

Studies on photophysical properties of pristine and nanocomposite thin films based on sol-gel TiO₂

Thesis submitted for the award of degree of
Doctor of Philosophy (Science)

JADAVPUR UNIVERSITY

December 2022



By

Sulakshana Mondal

School of Physical Sciences

Indian Association for the Cultivation of Science

Jadavpur, Kolkata - 700032, India

Dedicated to
Baba and Maa

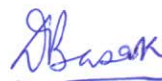


INDIAN ASSOCIATION FOR THE CULTIVATION OF SCIENCE
JADAVPUR, KOLKATA - 700032, INDIA

Prof. Durga Basak
Senior Professor
School of Physical Sciences

CERTIFICATE FROM THE SUPERVISOR

This is to certify that the thesis entitled “**Studies on photophysical properties of pristine and nanocomposite thin films based on sol-gel TiO₂**” submitted by **Ms. Sulakshana Mondal**, who got her name registered on 13.10.2015 for the award of Ph.D. (Science) degree of Jadavpur University, is absolutely based upon her own work under the supervision of **Prof. Durga Basak** and that neither this thesis nor any part of it has been submitted for either any degree/diploma or any other academic award anywhere before.


13/12/2022

(Signature of the supervisor
and date with official seal)



Dr. D. Basak, Ph.D.
Professor
Department of Solid State Physics
Indian Association for the
Cultivation of Science
Jadavpur, Kolkata - 700 032

Acknowledgement

The journey of my Ph.D. is not only a tale of my research works but a lifetime experience on enriching my character. This is a milestone for me with lots of memories of more than five years of hard works at the Indian Association for the Cultivation of Science (IACS), Jadavpur supported and encouraged by so many people. I feel deeply emotional while writing this section to acknowledge and thank those people I came across in this tenure of work.

First and foremost, I would like to pen down my sincere regards for my supervisor Prof. Durga Basak, School of Physical Sciences, IACS for her untiring guidance, meticulous support behind my all Ph.D. related studies and research, and invaluable inputs and insights throughout this dissertation. Without her continuous motivation, it would not have been possible for me to complete my doctoral studies alongside teaching. I am really grateful to her for giving me the freedom to carry out my research work.

I would like to acknowledge my senior and junior lab mates for all the inspiring and fruitful discussions, for all the stressful hours we are working together, and for all the fun we have had in the last more than five years. I am really thankful to my amazing seniors, Ashok da, Sanjit da, Arindam da, and Dipanwita di for being so helpful and supportive to me. Special thanks to my lovely juniors Shuvaraj, Ayon, Amaresh, Santanu, Sourav, Shantanu, and Barnali from the bottom of my heart. Thank you for all the respect, understanding, and support you have shown towards me. I also extend my gratitude to the employees of the School of Physical Sciences especially Sujit da and Pandit da for their administrative support.

I am thankful to Dr. Subhankar Tripathi, Principal, Sarsuna College, Dr. Suman Sinha, Head, Department of Physics, Sarsuna College and all my departmental colleagues for all the heartily support and cooperation whenever I needed. Special thanks to my closest and dearest colleague cum friend Dr. Sutapa Ganguly for her constant guidance and motivation, immense love and care.

I want to thank my friends Ankita and Sumana for being my side since last fourteen years. This journey would not be so memorable without their wonderful company. From the sleepless nights of studies to all the fun we made together is really blissful for me.

I am grateful to all the teachers and professors I came across in my life for enlightening and inspiring me to plan my future and become a better individual.

I take this opportunity to sincerely acknowledge the Department of Science and Technology (DST) for the financial support and my host institute IACS for giving me all other opportunities to perform the research work.

The thesis would not have come to a successful completion, without the help I received from the staffs of the Central Scientific Service and IACS workshop especially, Dr. Sasanka Maji, Dr. Bholanath Mondal, Mr. Rabindranath Banik, Mrs. Shipra Ghosh, Mr. Sutapesh Dutta and so many others.

Last but not the least; I am grateful to God for giving me such a loving family. I am blessed with each and everyone of my family specially my Baba, Maa, and Dida for their unwavering faith and trust on me. Without their endless love, care, and encouragement it would not have been possible to complete this journey. I am also fortunate to have my very supportive and motivating cousin sister, Riya. Thank you for being there with me and always doing the best to help me in my tough times.

Thank you all!

IACS, Kolkata
December, 2022

Sulakshana Mondal

Abstract

The thesis entitled “**Studies on photophysical properties of pristine and nanocomposite thin films based on sol-gel TiO₂**” deals with two photophysical properties namely photoluminescence and photodetection properties of TiO₂-based nanocrystalline thin films. TiO₂ being a wide band-gap (~ 3.0-3.2 eV) material is getting remarkable attention in various fields of applications due to its several unique properties like great thermodynamic stability, non-toxicity, low corrosion, and low cost. As TiO₂ has a very defect rich chemistry, the intrinsic and extrinsic defects present in TiO₂ cause appreciable change in the photoluminescence and photodetection properties. Therefore, engineering the surface defect states is very crucial to get significant modification of the mentioned properties. Here in this thesis work, easy and low-cost sol-gel technique has been used to prepare TiO₂ films followed by various post-growth treatments such as thermal annealing, vacuum annealing, UV curing to tune the surface defects and their concentration. Due to large band-gap, TiO₂ in general is ultraviolet (UV) light active and visible light blind. Among the various strategies adopted to get visible active TiO₂, incorporation of noble metals (Au, Ag, Pd, Pt) in TiO₂ is very beneficial and convenient way as these noble metal nanoparticles exhibit a unique property. The interaction of visible light with these noble metal nanoparticles results in the collective oscillation of free electrons in nanoparticle lattice in resonance with the electromagnetic field of light called surface plasmon resonance (SPR). Therefore, plasmonic Ag-TiO₂ nanocomposite film is synthesized to get visible photoactivity in this work. To study the defect states in TiO₂ like other semiconducting materials, doping is one of the well-known processing steps though the impurity incorporation into TiO₂ films has already achieved successfully using doping during growth or by diffusion, a controllable doping is still difficult. In such cases, post-growth doping via ion implantation can be an effective way where also the accumulation of doping impurities on the surface of the TiO₂ due to excess surface energy can be avoided. Therefore, in this work, Li doped TiO₂ is synthesized to study the defects and their effect on the above said photophysical properties. With the above-mentioned motivation, the work embodied in this thesis has focused mainly on two aspects:

- (i) Studies on photophysical properties of pristine sol-gel grown TiO₂ nanocrystalline thin films via various post-growth treatments
- (ii) Studies on the photophysical properties of TiO₂-based nanocomposite films and the evolution of defects in doped TiO₂ films via ion implantation

The entire thesis consists of total eight chapters. The chapter wise contents are given below:

The chapter 1 provides a concise general introduction of TiO₂ material and its advantages over other wide band-gap semiconductors followed by the motivation and organization of the thesis.

A brief status review on the published works dealing with enhanced photophysical properties of TiO₂, TiO₂-based nanocomposite, and doped TiO₂ has been presented in the chapter 2.

Chapter 3 consists of two sections; (i) Detailed descriptions of the deposition methods, and (ii) various types of characterization techniques particularly those used for this thesis work have been discussed in this chapter.

The influence of various post-growth annealing processes on the defects of sol-gel grown TiO_2 thin films has been investigated in the chapter 4. It has been observed that annealing in air followed by a rapid cooling process offers an efficient method to achieve a stronger UV emission and reduced visible emissions giving the highest UV to visible emission ratio value. The correlation between various types of surface defects formed due to different post-growth treatments with the visible emissions occurred in the films has been analysed thoroughly in this chapter.

In the chapter 5, highly efficient UV photodetection property of nanocrystal assembled TiO_2 films via defects tuning has been discussed. An extremely high UV-to-visible rejection ratio of 1.7×10^3 and photo-to-dark current ratio of 1.2×10^4 under 10 V bias and $10 \mu\text{W}$ incident light power in a simple lateral photoconductive geometry have been observed for UV cured TiO_2 film. This study also explains the influence of intrinsic defects like Ti^{3+} , oxygen vacancy (V_O) as well as surface adsorbed O_2 , OH species on the UV photodetection properties of TiO_2 . A photo-to-dark-current ratio of $\sim 10^4$ under as low as 1 V bias condition and $10 \mu\text{W}$ incident UV light reveal that simple sol-gel processed films followed by a post-growth UV curing can be promising candidate for efficient UV photodetector without any device fabrication.

UV to visible broad band photodetection property of plasmon assisted Ag- TiO_2 nanocomposite film has been presented in the chapter 6. In this study, various thicknesses of Ag nanoparticles on the sol-gel grown TiO_2 has been deposited and their photoresponse under various wavelengths of incident light has been rigorously discussed. For 1 nm thick Ag layer on TiO_2 , unprecedentedly high photo-to-dark current ratio of 10^7 , 10^5 and 10^4 under 350 nm, 680 nm and 550 nm light illuminations have been observed. It has been concluded that the plasmonic hot carriers play a crucial role in the highly enhanced visible photodetection property of Ag- TiO_2 nanocomposite film which depends on the Ag nanoparticle size.

In chapter 7, both photoluminescence and photodetection properties of Li doped TiO_2 films prepared via post-growth ion implantation method has been illustrated. It has been observed that creation of more acceptor levels defects upon Li ion fluence of 1×10^{14} causes violet emission. Then with increasing the fluence, probably due to creation of nonradiative recombination pathways, the violet emission has been disappeared. The enhanced visible emission has been noticed for higher fluence sample indicating formation of more defects like V_O and Ti^{3+} related states.

A list of up-to-date references relevant to the topics of the chapter has been included at the end of each chapter.

Finally, in the chapter 8, a summary of the important results stemming out from this thesis work has been listed followed by a future scope of the work.

List of publications

Publications included in the thesis:

1. “Defect controlled tuning of the ratio of ultraviolet to visible light emission in TiO₂ thin films” **Sulakshana Mondal**, Durga Basak, Journal of Luminescence, 179, 480–486, (2016)
2. “Very high photoresponse towards low-powered UV light under low-biased condition by nanocrystal assembled TiO₂ film” **Sulakshana Mondal**, Durga Basak, Applied Surface Science, 427, 814–822, (2018)
3. “Plasmon assisted high ultraviolet to visible broad band photosensitivity in lateral Ag NPs-TiO₂ nanocomposite film” **Sulakshana Mondal**, Durga Basak, Surfaces and Interfaces 31, 102090, (2022)
4. Investigations on photoluminescence and photodetection properties of Li doped TiO₂ films **Sulakshana Mondal**, Durga Basak (Manuscript under preparation)

Publications excluded from the thesis:

1. Sb₂S₃/Spiro-OMeTAD Inorganic-Organic Hybrid p-n Junction Diode for High Performance Self-Powered Photodetector A Bera†, A Das Mahapatra†, **S Mondal**, D Basak, ACS Applied Materials & Interfaces, 8 (50), 34506–34512, (2016)
2. TiO₂ Nanoparticles Incorporated Peptide Appended Perylene Bisimide-Based Nanohybrid System: Enhancement of PhotoSwitching Behavior S Roy, K Basu, K Gayen, S Panigrahi, **S Mondal**, D Basak, A Banerjee, The Journal of Physical Chemistry C, 121 (9), 5428-5435, (2017)

Contents

	Page No.
List of Tables.....	ix
List of Figures.....	xi
1 Chapter 1: Introduction and motivation.....	1
1.1 Background of the work.....	3
1.2 Properties of TiO ₂	5
1.3 Motivation and organization of the thesis.....	7
1.4 References.....	9
2 Chapter 2: Photoluminescence and photodetection properties of TiO₂ and TiO₂-based structures: An overview	
2.1 Introduction.....	15
2.2 Photoluminescence property	15
2.2.1 PL properties of TiO ₂	16
2.2.2 PL properties of TiO ₂ -based composites.....	18
2.2.3 PL properties of doped TiO ₂	19
2.3 Photodetection properties of TiO ₂	21
2.3.1 UV photodetection properties of TiO ₂ and TiO ₂ -based materials.....	22
2.3.2 Visible photodetection properties of TiO ₂ and TiO ₂ -based materials.....	24
2.4 Defects in TiO ₂	27
2.5 Conclusions.....	28
2.6 References.....	28
3 Chapter 3: Thin film synthesis and characterization techniques.....	35
3.1 Introduction	37
3.2 Thin film synthesis techniques	37
3.2.1 Chemically solution deposition techniques.....	38
3.2.1.1 Sol-gel.....	38
3.2.2 Physical vapor deposition techniques.....	40
3.2.2.1 Vacuum thermal evaporation.....	41
3.2.2.2 Post-growth doping: Ion implantation.....	42
3.3 Thin films characterization techniques.....	43
3.3.1 Structural and elemental characterization techniques.....	43

3.3.1.1	X-ray Diffraction	43
3.3.1.2	X-ray Photoelectron Spectroscopy	45
3.3.2	Microstructural and morphological characterization techniques	47
3.3.2.1	Field Emission Scanning Electron Microscopy	47
3.3.2.2	Atomic Force Microscopy	50
3.3.3	Optical characterization techniques	51
3.3.3.1	UV-VIS transmission and absorption spectroscopy	51
3.3.3.2	Photoluminescence measurement	53
3.3.3.3	Time Correlated Single Photon Counting	54
3.3.3.4	Raman spectroscopy	56
3.3.4	Optoelectronic characterization techniques	57
3.3.4.1	Photoconductivity measurements	58
3.4	References	61
4	Chapter 4: Investigation on photoluminescence properties of TiO₂ thin films via various post-growth treatments	63
4.1	Introduction	65
4.2	Experimental details	65
4.3	Results and discussions	67
4.4	Conclusions	75
4.5	References	76
5	Chapter 5: Development of TiO₂ thin films as ultraviolet photodetector via defects tuning	79
5.1	Introduction	81
5.2	Experimental details	81
5.3	Results and discussions	81
5.4	Conclusions	92
5.5	References	93
6	Chapter 6: Ultraviolet to visible broad-band photodetection by Ag-TiO₂ plasmonic nanocomposites	95
6.1	Introduction	97
6.2	Experimental details	97
6.3	Results and discussions	98

6.4	Conclusions.....	108
6.5	References.....	109
7	Chapter 7: Investigation on photoluminescence and photodetection properties of Li doped TiO₂ films.....	111
7.1	Introduction	113
7.2	Experimental details.....	113
7.3	Results and discussions.....	114
7.4	Conclusions.....	121
7.5	References.....	121
8	Chapter 8: Summary and future scope.....	123

List of Tables

	Page No.
Table 1.1. Properties of TiO ₂ . Ref. [60, 72]	6
Table 3.1. Various thin film deposition techniques	37
Table 4.1. Values of direct, indirect band-gap, UV/VIS, and green/orange emission of the samples	72
Table 4.2. Decay parameters of the samples estimated from TCSPC	74
Table 5.1. The values of dark current (I_d), photocurrent (I_{ph}), and I_{ph}/I_d for all the films	89
Table 6.1. Dark current (I_d), photo current (I_{ph}), and photo-to-dark current ratio (I_{ph}/I_d) under 350, 680, 550, and 450 nm illuminations for all samples	107
Table 7.1. Nomenclature of the samples.....	114
Table 7.2: The values dark current (I_d), photocurrent (I_{ph}), I_{ph}/I_d (for UV and visible (500 nm) illuminations), rise time, and decay time for UV illumination for all samples.....	121

List of Figures

	Page No.
Fig. 1.1: Schematic representation of TiO ₂ crystal structures; (a) Rutile, (b) Anatase, and (c) Brookite. Ref. [67]	5
Fig. 2.1: Photocurrent transport mechanism in TiO ₂ thin film. (a) Schematic illustration of TiO ₂ thin film-based UV photodetector. (b) Adsorption of oxygen molecules on the surface of TiO ₂ thin film in the dark and the upward band bending. (c) Under UV illumination, some of the photogenerated holes migrate to the TiO ₂ thin film surface due to the desorption of adsorbed oxygen molecules. This effectively decreases the resistive depletion layer width of the TiO ₂ thin film	24
Fig. 3.1: Schematic diagram of TiO ₂ thin film preparation by sol-gel method.....	39
Fig. 3.2: Digital image of the spin coating unit (APEX Instruments, Model: spinNXG-P1) used in the work.....	40
Fig. 3.3: A schematic (left) and digital image (right) of the vacuum thermal evaporator (HINDHIVAC, Model: 12A4D).....	41
Fig. 3.4: Digital image of the implantation unit of LEIBF at IUAC, New Delhi	42
Fig. 3.5: A schematic (left) and digital image (right) of the XRD instrument (Bruker, Model: D8).....	44
Fig. 3.6: A schematic of the working principle of XPS	46
Fig. 3.7: Digital image of the XPS instrument (Omicron, Serial No.: 0571).....	47
Fig. 3.8: A schematic of the working principle of FESEM.....	48
Fig. 3.9: Digital image of FESEM (JEOL, Model: JSM-6700F).....	49
Fig. 3.10: A schematic (left) and digital image (right) of the AFM instrument (VECCO, Model: diCP-II).....	50
Fig. 3.11: A schematic (left) and digital image (right) of the UV-VIS spectrometer (PerkinElmer, Model: Lamda 35)	52

Fig. 3.12:	A schematic of the PL instrument.....	53
Fig. 3.13:	Digital image of the PL measurement set-up.....	54
Fig. 3.14:	Digital image of the TCSPC instrument	55
Fig. 3.15:	A schematic of Raman spectroscopy	56
Fig. 3.16:	Digital image of the Raman instrument	57
Fig. 3.17:	A schematic of the photoconductivity measurement	58
Fig. 3.18:	Digital image of the photoconductivity measurement set-up	60
Fig. 4.1:	Flow chart of the (a) sol-gel preparation of TiO ₂ films and (b) various post-growth treatments of TiO ₂ films	66
Fig. 4.2:	XRD patterns of (a) Sample A, (b) Sample B, and (c) Sample C.....	67
Fig. 4.3:	Transmission spectra of the (a) Sample A, (b) Sample B, (c) Sample C, and (d) bare substrate. The inset shows the variation of refractive indices with wavelength for all samples.....	68
Fig. 4.4:	Representative (a) $(ah\nu)^2$ vs $h\nu$ and (b) $(ah\nu)^{1/2}$ vs $h\nu$ plots of Sample A	69
Fig. 4.5:	RT PL spectra of (a) Sample A, (b) Sample B, and (c) Sample C. The inset shows an enlarged view of the UV emission	70
Fig. 4.6:	Gaussian multi-peak fitting of the visible photoluminescence spectra of (a) Sample A, (b) Sample B, and (c) Sample C	71
Fig. 4.7:	XPS pattern of (a) Sample A, (c) Sample B,-/ and (e) Sample C. Gaussian peak fitting of Ti 2p _{3/2} peak of (b) Sample A, (d) Sample B, and (f) Sample C.....	73
Fig. 4.8:	(a) Representative time resolved UV PL decay profile of Sample C (b): Room temperature dark $I-V$ curves of (a) Sample A, (b) Sample B, and (c) Sample C.....	75
Fig. 5.1:	(a) XRD patterns of all the samples. The inset in the figure shows the enlarged view of (101) peak. The cross-sectional SEM images of (b) SA, (c) SB, and (d) SC. The inset in the respective figure shows the magnified view of the columns. AFM images of (e) SA, (f) SB, and (g) SC	82

Fig. 5.2:	(a) Absorption spectra of the samples. Inset shows the corresponding Tauc plots for the samples. (b) Dark I - V of samples. Inset shows the schematic diagram of experimental set-up for photoconductivity measurement, (c) and (d) Photocurrent spectra of the samples at 10 V for high and low incident power respectively. Inset shows the corresponding value of UV-to-visible rejection ratio	84
Fig. 5.3:	(a) Absorption spectra of the samples. Inset shows the corresponding Tauc plots for the samples. (b) Dark I - V of samples. Inset shows the schematic diagram of experimental set-up for photoconductivity measurement, (c) and (d) Photocurrent spectra of the samples at 10 V for high and low incident power respectively. Inset shows the corresponding value of UV-to-visible rejection ratio	86
Fig. 5.4:	Transient photoresponse curves at 10 V bias for various incident powers of UV light for (a) SA, (b) SB, and (c) SC. (d) Transient photoresponse of all the samples at 1 V bias and 350 μ W UV irradiance. (e) Transient photoresponse curves of SC at 1 V bias for various power values. (f) Power dependence of the photocurrent at 10 V and corresponding fitting of photocurrent for all the samples.....	87
Fig. 5.5:	XPS Ti 2p _{3/2} peak fitting for (a) SA, (c) SB, and (e) SC. The Insets show full scan of the XPS spectrum for the corresponding samples. XPS O 1s peak fitting for (b) SA, (d) SB, and (f) SC. The contribution of each of the fitted peak is shown in the figures for all samples.....	90
Fig. 5.6:	Time dependent growth-decay cycles at three fixed bias conditions for (a) SA, (b) SB, and (c) SC respectively for 350 μ W UV illumination. (d) Growth-decay cycle of SC at low bias (1 V) and low incident power (10 μ W)	91
Fig. 5.7:	Stability of the detector after prolonged exposure to UV light at 10 V bias and 350 μ W UV irradiation	92
Fig. 6.1:	Schematic diagram of sample preparation.....	98
Fig. 6.2:	XRD patterns of all the samples. The inset shows XRD pattern of pristine Ag NPs' film.....	99

Fig. 6.3:	FESEM images of the samples (a) S1, (b) S2, (c) S3, and (d) S4	100
Fig. 6.4:	EDX spectra of the samples (a) S1, (b) S2, (c) S3, and (d) S4. The inset shows the atomic percentage of the elemental components of the samples	101
Fig. 6.5:	(a) Optical transmission spectra of all the samples. (b) UV-visible absorption spectra of all the samples. Inset shows the enlarged view of spectra within the range of 400 to 800 nm. (c) Absorbance spectra of pristine Ag NPs films of different thickness on glass substrate.....	102
Fig. 6.6:	XPS spectra of (a) Ti 2p _{3/2} (b) O 1s (c) Ag 3d peaks of S2	103
Fig. 6.7:	(a) Dark <i>I-V</i> and (b) Photocurrent spectra at 10 V bias for all the samples	104
Fig. 6.8:	(a) Spectral responsivity and (b) specific detectivity of all the samples.....	105
Fig. 6.9:	Transient photoresponse of all the samples under (a) 350 nm, (b) 680 nm, (c) 550 nm, and (d) 450 nm light illumination at 10 V bias	106
Fig. 6.10:	(a) Band alignment of Ag and TiO ₂ junction and (b) Schematic diagram for hot electron transfer from Ag to TiO ₂	107
Fig. 6.11:	Periodic growth-decay cycles of all the samples under (a) 350 nm, (b) 680 nm, and (c) 550 nm wavelength light irradiation.....	108
Fig. 7.1:	(a) XRD patterns of all the samples and (b) Enlarged view of (101) peak of all the samples.....	114
Fig. 7.2:	(a) XPS full scan of pristine and TLi115, (b) Li 1s peak of TLi115, (c), (d) Ti 2p, and (e), (f) O 1s peak fitting of pristine and TLi115 respectively	116
Fig. 7.3:	(a) Optical absorbance spectra and (b) PL spectra of the samples	117
Fig. 7.4:	(a) Raman spectra and (b) Enlarged view of 1E _g mode of all the samples.....	118
Fig. 7.5:	(a) Photocurrent spectra of all samples. (b) Transient photoresponse of all samples under (b) UV (340 nm) and (c) visible (500 nm) illumination. (d) Periodic growth-decay cycles of sample TLi115	120

CHAPTER-1

Introduction and motivation

1.1 Background of the work

Over past two decades, TiO_2 [titanium (iv) oxide or titania] is getting remarkable attention in the field of various optoelectronic, photochemical, and photophysical applications due to its extraordinary properties like wide band-gap, great thermodynamic stability, low corrosion, non-toxicity, and low cost [1-5]. Among the above-mentioned application fields, photophysical applications are very demanding in current research areas [6-10]. Among the various photophysical phenomena, photoluminescence and photodetection are two main kinds where prospects of TiO_2 -based materials need extensive investigation.

Photoluminescence (PL) spectroscopy, is the spontaneous emission of light from a material following optical excitation. It is a non-contact, non-destructive method to probe the electronic structure of materials. The materials exhibiting PL properties are significant for practical applications such as solid-state lighting (SSL), light emitting diodes (LEDs), display devices, sensing, and biomedical applications [11-17]. TiO_2 being a wide band-gap material having good electron mobility and high light absorption coefficient is a very promising candidate for luminescence [18-22]. It has band-gap of 3.0-3.4 eV that permits activation by the ultraviolet (UV) light and then electron-hole (exciton) pairs are produced. The electrons can quickly relax to the bottom of the conduction band (CB), where its mobility can carry it to a defect site or elsewhere. As TiO_2 has high defect rich chemistry, PL study can also be a great tool to probe its defect states [23, 24]. The presence of defects or impurities disturbs the local band structure of TiO_2 by interrupting the periodicity of the lattice. Hence a local charge irregularity is generated due the presence of the defects that act as traps for the photogenerated charge carriers i.e., electrons and holes. At low temperature the interactions between photoexcited charge carriers and lattice phonons are significantly reduced, and as a result, charge carriers become trapped at defect sites, where they recombine following an emission of defect states related PL [25-27].

Photodetection is another main photophysical property which has extensive usage in optical communication systems, optical interconnections, biomedical imaging, and many more [28-32]. A photodetector is a device that converts the incident photon energy into an electrical signal where the active component of it is usually made up of semiconducting materials [33]. The working principle of a photodetector is, when a photon of ample energy strikes the detector, it makes a pair of an electron-hole. This mechanism is also known as the internal photoelectric effect [34]. If the absorption arises in the depletion region junction, then the

carriers are removed from the junction by the inbuilt electric field of the depletion region. Therefore, holes in the region move toward the anode, and the electrons move toward the cathode, hence a photocurrent is generated [35]. Based on the spectral detection limit, the detectors can be divided into UV, visible, and near infrared (NIR) photodetectors. For a broad spectral detection, it is called as broad-band photodetector. In our modern daily life, usage of UV radiation has now become an important part because of its widespread applications such as water and air purification, therapeutic purposes, disinfection for viruses, hygiene and infection control, fluorescent inspection, flame detection, environmental studies etc [36-42]. It is generally known that a moderate UV light is beneficial for human health however, excessive exposure of UV rays can cause various health issues like eye problems, skin cancer, wrinkling, etc [43, 44]. Therefore, an efficient detection of UV radiation is necessary. In the past decades, narrow band-gap silicon, some III-V compounds (GaP, GaAs, etc.) have been broadly investigated for the purpose of UV photodetection [45, 46]. Nevertheless, there are intrinsic imperfections for those, such as fragile, large volume, high cost related to raw materials, and expensive growth technology which obstacles their application in miniaturized and reliable UV detection devices for portability or shipping. To overcome the limitations, development of a new generation of wide band-gap semiconductor-based UV photodetectors has received a great interest. In this scenario, a delicate selection of suitable material with efficient morphological, microstructural, and photoelectrical properties plays a key role in the construction of high-performance photodetector. Many wide band-gap semiconductors including GaN, TiO₂, ZnO, SiC, ZnS, ZnSe, Ge₂O₃ etc. have been chosen for investigation as UV photodetectors [47-51]. Among them, TiO₂ is emerged as a novel material due to its excellent physical, chemical, optical, and optoelectrical properties. Moreover, its high electron transport property and suitable band-gap makes TiO₂ appropriate for UV detection [9, 52]. Detection of visible light is also significant because of applications in a wide variety of fields ranging from day-to-day consumer electronics to more advanced and complex applications such as camera sensors, spectroscopic instruments, various communications etc. [53-56]. Generally, pristine TiO₂ can't be used in visible photodetection as its optical band-gap restricts the visible photon absorption. Many strategies like doping with metal or non-metal elements, surface modification, photosensitization, noble metal incorporation etc. can be performed to extend the absorption edge of TiO₂ in the visible range to get visible photo active TiO₂ [57-59].

1.2 Properties of TiO₂

TiO₂ is an inexpensive, biocompatible material having high dielectric constant, strong oxidizing power, great refracting index with large surface area [60-62]. It is by far the most suited white pigment to obtain whiteness and hiding power in coatings, inks, self-cleaning ceramics, and plastics as well as food items, medicines, cosmetics products [63-65]. Apart from this, there are several additional beneficial properties of TiO₂, such as the scope of band-gap engineering, availability of large area single crystal substrates, various formation of nanostructures, large piezoelectric constants, easy wet chemical etching, environmental benefits, etc. [66-68] Further, by simple post-growth treatments, fabricating composites, doping with suitable materials its optical, electrical, and optoelectronic properties can be tuned for making a better and efficient candidate for broad area of applications.

There are three common polymorphs (phases) of TiO₂ found in nature; anatase, rutile, and brookite which are all composed of TiO₆ octahedra (i.e., Ti⁴⁺ coordinated to six O²⁻) but in different arrangements [1]. The crystalline structures of all three phases are shown in Fig. 1.1. At ambient pressure, TiO₂ crystallizes into mainly two polymorphs, anatase and rutile. Anatase is the most common and low temperature phase. Commonly, anatase forms at temperature below 600 °C and above this temperature, it transforms to thermodynamically stable rutile phase [70, 71].

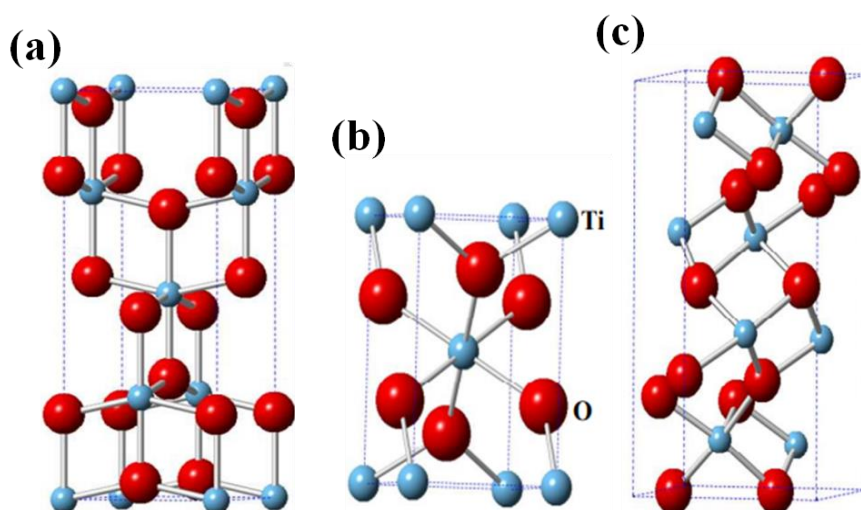


Fig. 1.1: Schematic representation of TiO₂ crystal structures; (a) anatase, (b) rutile, and (c) brookite. Ref. [69].

Introduction and motivation

Anatase and rutile both crystallizes in the tetragonal system. Both structures can be described in terms of chains of TiO_6 octahedra that are more distorted in anatase than in rutile. Therefore, unit cells of anatase and rutile are significantly dissimilar which results in their distinct physical and chemical behavior. Anatase and rutile belong to space group $I4_1/amd$ and $P4_2/mnm$ respectively [73]. The characteristics of Ti-O bonds play very crucial roles in the properties of different TiO_2 phases [74]. In both rutile and anatase, there are two elongated Ti-O bonds in each octahedron

Table. 1.1. Properties of TiO_2 . [60, 72]

Phase	Crystal system	Refractive index	Lattice constant (nm)			Band-gap (eV)	Density (gm/cm^3)
			a	b	c		
Rutile	tetragonal	2.609	0.459	0.459	0.296	3.0	4.13
Anatase	tetragonal	2.488	0.378	0.378	0.953	3.2	3.79
Brookite	orthorhombic	2.583	0.544	0.915	0.514	—	3.99

and lengthening of these two bonds is greater in rutile than anatase which indicates relative weakening of the bonds in rutile. This results in a decrease in the energy required for the excitation of the bonds for rutile. The (110) face in rutile has the lowest surface energy and it is the most intensely studied surface. In rutile, along the [001] direction, six-fold-coordinated Ti atoms rows alternate with five-fold-coordinated Ti atoms with one ‘dangling bond’ perpendicular to the surface. Two types of oxygen atoms are present in rutile TiO_2 . Oxygens on main surface planes are three-fold coordinated where bridging oxygens are two-fold-coordinated. For anatase, (101) and (001) plans are the two main surfaces. The closed-pack structure of anatase consists of large oxygen with titanium atoms with every second octahedral interstitial site in a zigzag alignment. Each titanium atom is thus surrounded by an oxygen octahedron. The evident ionic character of atoms results a strong crystal field that distorts the octahedral. The third phase, brookite, a metastable phase of TiO_2 which is often observed as a by-product when the synthesis procedure is carried out in an acidic medium at low temperature. Pure brookite without rutile or anatase is usually difficult to prepare [75, 76]. This phase belongs to orthorhombic structure whose unit cell composed of octahedra, each with a titanium

atom at its center with oxygen atoms at its corners. Some fundamental and key properties of all three structures are summarized in Table 1.1.

1.3 Motivation and Organization of thesis

The studies on PL property of TiO_2 has so far been focused on the controllable synthesis as well as fabrication of heterostructures based on TiO_2 for realizing enhanced functionality [77, 78]. Knowing the fact that PL property of TiO_2 highly depends upon surface defect states, controlled technique of engineering the defects is crucial to achieve significant emission properties of TiO_2 [79-81]. Hence, surface modification via simple post-growth treatment of TiO_2 thin films is an easy and efficient approach to modify the surface defects of TiO_2 as well as for enhancement of emission properties without fabricating any complex heterostructure.

Pristine TiO_2 is an eligible candidate for UV detection as mentioned earlier. Similar to PL, the sub-band-gap density of states mainly originated from the defect states such as oxygen vacancy (V_O) and surface adsorbed species strongly influence the properties of TiO_2 and consequently its UV photodetection property by affecting carrier mobility and recombination [9, 82, 83]. Therefore, post-growth treatments are also useful for tuning the defects to achieve enhanced UV photodetection. Superior operation of TiO_2 or TiO_2 -based composite UV photodetectors is mostly realized in photodiode mode which involves a p-n junction of similar or dissimilar semiconducting material leading towards complicated fabrication procedures [84, 85]. On the other hand, pristine TiO_2 film as single semiconducting layer photodetector based on photoconducting principle may engage much simple synthesis process and without fabricating any complex heterostructure it can exhibit high UV photosensitivity.

Besides UV detection, TiO_2 can be a very promising candidate for visible photodetection by incorporating noble metals (Au, Ag, Pt, Pd) into it [86-88]. Due to surface plasmon resonance (SPR), the noble metal nanoparticles (NPs) can absorb visible photons which can generate hot carriers. These hot carriers can exhibit visible photosensitivity of noble metal modified TiO_2 -based composite systems. Among all noble metals, Ag is cheaper, abundant, and it possesses unique plasmonic properties [89]. Therefore, Ag NPs modified TiO_2 films can be an ideal combination for visible photodetection.

Among the several approaches to modify the defects and to study its effect on the photophysical properties of TiO_2 , doping in TiO_2 with suitable elements is very enticing for the current field of research [90, 91]. Selection of proper dopant to enhance the desired property is

also essential in this purpose. Various metals and non-metals are popularly used to dope TiO_2 to tune its photophysical properties [92-98]. Being a group-I element and comparable cationic radius with Ti, Li doped TiO_2 has special importance for wide area of applications. Hence a detailed discussion on the photophysical properties of Li doped TiO_2 is needed.

Keeping eye on the above-mentioned issues the main objectives of this thesis work have been decided as: (i) Tuning the structural defects in TiO_2 thin films by various post-growth treatments and study their PL properties. (ii) Developing TiO_2 films as efficient UV photodetector by post-growth treatments via defect engineering. (iii) UV to visible broad-band photodetection by Ag- TiO_2 nanocomposite film. (iv) Investigation of photophysical properties of Li doped TiO_2 films. Considering the applications and advantages of TiO_2 as discussed in the earlier sections, the work presented in this thesis has focused mainly on the detailed investigations on two photophysical properties of TiO_2 namely PL and photodetection.

With the given opportunity of the progressive work on those photophysical properties, the title of the thesis has been chosen as ‘Studies on photophysical properties of pristine and nanocomposite thin films based on sol-gel TiO_2 ’. The thesis consists of eight chapters including a brief introduction on TiO_2 which has been presented in this chapter 1 with an objective and organization of the thesis work. In chapter 2, a status review on the PL and photodetection properties of TiO_2 has been illustrated. Various synthesis processes for TiO_2 thin films have been elaborated in the chapter 3 followed by the descriptions of different types of characterization techniques used in this work. In the chapter 4, various post-growth treatments on tuning the defects and their effect on the PL properties of TiO_2 films grown by the sol-gel process have been investigated. The effect of various post-growth treatments on UV photodetection properties of simple sol-gel grown TiO_2 films have been discussed in chapter 5. In chapter 6, plasmon assisted UV to visible broad-band photodetection by Ag- TiO_2 composite films has been presented. An investigation on the photophysical properties of TiO_2 due to Li doping has been discussed in chapter 7. Finally, a summary of the important results that emerged from this thesis work has been presented followed by a future scope of the work in chapter 8.

1.4 References

- [1] J. Schneider, M. Matsuoka, M. Takeuchi, J. Zhang, Y. Horiuchi, M. Anpo, and D. W. Bahnemann, *Chemical reviews*, **114** (2014) 9919-9986
- [2] M. Pawar, S. Topcu Sandoğdular, and P. Gouma, *Journal of Nanomaterials*, **2018** (2018)
- [3] Q. Guo, C. Zhou, Z. Ma, and X. Yang, *Advanced Materials*, **31** (2019) 1901997
- [4] S. Peiris, H. B. de Silva, K. N. Ranasinghe, S. V. Bandara, and I. R. Perera, *Journal of the Chinese Chemical Society*, **68** (2021) 738-769
- [5] X. Chen, S. Shen, L. Guo, and S. S. Mao, *Chemical reviews*, **110** (2010) 6503-6570
- [6] K. Nakata, and A. Fujishima, *Rev*, **13** (2012) 169-189
- [7] U. M. Nayef, K. A. Hubeatir, and Z. J. Abdulkareem, *Optik*, **127** (2016) 2806-2810
- [8] A. J. Molina-Mendoza, A. Moya, R. Frisenda, S. A. Svatek, P. Gant, S. Gonzalez-Abad, E. Antolin, N. Agraït, G. Rubio-Bollinger, and D. P. de Lara, *Journal of Materials Chemistry C*, **4** (2016) 10707-10714
- [9] Z. Li, Z. Li, C. Zuo, and X. Fang, *Advanced Materials*, (2022) 2109083
- [10] J. M. Aguilar-Camacho, L. Doonan, and G. P. McCormack, *Molecular phylogenetics and evolution*, **131** (2019) 245-253
- [11] X. Zhou, J. Qiao, and Z. Xia, *Chemistry of Materials*, **33** (2021) 1083-1098
- [12] A. Kitai, *Luminescent Materials and Applications*
- [13] A. Dwivedi, M. Srivastava, and S. Srivastava, *Journal of Molecular Structure*, **1251** (2022) 132061
- [14] W. P. Lustig, S. Mukherjee, N. D. Rudd, A. V. Desai, J. Li, and S. K. Ghosh, *Chemical Society Reviews*, **46** (2017) 3242-3285
- [15] B. P. S. A.K.Soni, *Luminescent Materials in Lighting, Display, Solar Cell, Sensing, and Biomedical Applications*,
- [16] H. Wang, and G. Liu, *Journal of Materials Chemistry B*, **6** (2018) 4029-4042
- [17] D. Singh, S. Bhagwan, A. Dalal, K. Nehra, K. Singh, A. Simantilleke, S. Kumar, and I. Singh, *Optik*, **208** (2020) 164111
- [18] A. M. Bolbol, O. H. Abd-Elkader, H. Elshimy, Z. I. Zaki, S. A. Shata, M. Kamel, A. S. Radwan, and N. Y. Mostafa, *Results in Physics*, **42** (2022) 105955
- [19] H. Tang, and K. Prasad, *Sens. Actuators B*, **26** (1995) 71
- [20] A. Meng, L. Zhang, B. Cheng, and J. Yu, *Advanced Materials*, **31** (2019) 1807660
- [21] H. Tang, H. Berger, and P. Schmid, *Optical Properties of Anatase TiO₂*,” *Solid State Commun*, **92** (1994) 267
- [22] S. Mathew, T. Benoy, P. Rakesh, M. Hari, T. Libish, P. Radhakrishnan, V. Nampoori, and C. Vallabhan, *Journal of fluorescence*, **22** (2012) 1563-1569
- [23] S. Binetti, A. Le Donne, and A. Sassella, *Solar energy materials and solar cells*, **130** (2014) 696-703
- [24] G. Yue, J. Lorentzen, J. Lin, D. Han, and Q. Wang, *Applied Physics Letters*, **75** (1999) 492-494
- [25] K. Mettler, *Applied physics*, **12** (1977) 75-82
- [26] D. K. Schroder, *Semiconductor material and device characterization*, John Wiley & Sons, (2015)
- [27] A. Stevanovic, M. Büttner, Z. Zhang, and J. T. Yates Jr, *Journal of the American Chemical Society*, **134** (2012) 324-332
- [28] D. Yang, and D. Ma, *Advanced Optical Materials*, **7** (2019) 1800522
- [29] M. J. D. A. Bandyopadhyay, *Photodetectors for Optical Fiber Communications*,
- [30] Z. Zhao, J. Liu, Y. Liu, and N. Zhu, *Journal of Semiconductors*, **38** (2017) 121001

- [31] Controlling the photon absorption characteristics in avalanche photodetectors for high resolution biomedical imaging, Proceedings of the Nanoscale Imaging, Sensing, and Actuation for Biomedical Applications XVIII, **(2021)**;
- [32] A. Biberman, and K. Bergman, Reports on Progress in Physics, **75** (2012) 046402
- [33] J. Wang, and W. Hu, Chinese Physics B, **26** (2017) 037106
- [34] G. S. Spagnolo, A. Postiglione, and I. De Angelis, Physics Education, **55** (2020) 055011
- [35] S. Mridha, and D. Basak, journal of Applied Physics, **101** (2007) 083102
- [36] J. Cheng, Y. Zhang, and R. Guo, Journal of Crystal Growth, **310** (2008) 57-61
- [37] F. Zeng, S. Cao, W. Jin, X. Zhou, W. Ding, R. Tu, S.-F. Han, C. Wang, Q. Jiang, and H. Huang, Journal of Cleaner Production, **243** (2020) 118666
- [38] A. A. Ameen, H. ElSayed, and A. H. Aly, RSC advances, **11** (2021) 14915-14921
- [39] Z. Qureshi, and M. H Yassin, Infectious Disorders-Drug Targets (Formerly Current Drug Targets-Infectious Disorders), **13** (2013) 191-195
- [40] E. Gorokhov, A. Magunov, V. Feshchenko, and A. Altukhov, Instruments and Experimental Techniques, **51** (2008) 280-283
- [41] A. R. Pauchard, D. Manic, A. Flanagan, P. A. Besse, and R. S. Popovic, IEEE Transactions on Industrial Electronics, **47** (2000) 168-174
- [42] M. Heßling, K. Hönes, P. Vatter, and C. Lingenfelder, GMS hygiene and infection control, **15** (2020)
- [43] R. M. Lucas, and A. L. Ponsonby, Medical journal of Australia, **177** (2002) 594-598
- [44] J. D’Orazio, S. Jarrett, A. Amaro-Ortiz, and T. Scott, International journal of molecular sciences, **14** (2013) 12222-12248
- [45] New capabilities of GaAs detectors for UV applications, Proceedings of the Optoelectronic Integrated Circuit Materials, Physics, and Devices, **(1995)**;
- [46] R. Hughes, T. Zipperian, L. Dawson, R. Biefeld, R. Walko, and M. Dvorack, Journal of applied physics, **69** (1991) 6500-6505
- [47] A. Kumar, M. Kumar, V. Bhatt, D. Kim, S. Mukherjee, J.-H. Yun, and R. K. Choubey, Chemical Physics Letters, **763** (2021) 138162
- [48] D. Walker, and M. Razeghi, Opto-Electronics Review, **8** (2000) 25-42
- [49] A. Tonkikh, E. Voloshina, P. Werner, H. Blumtritt, B. Senkovskiy, G. Güntherodt, S. Parkin, and Y. S. Dedkov, Scientific reports, **6** (2016) 1-8
- [50] P. Hu, Z. Wen, L. Wang, P. Tan, and K. Xiao, ACS nano, **6** (2012) 5988-5994
- [51] K. Liu, M. Sakurai, and M. Aono, Sensors, **10** (2010) 8604-8634
- [52] J. Zou, Q. Zhang, K. Huang, and N. Marzari, The Journal of Physical Chemistry C, **114** (2010) 10725-10729
- [53] G. Konstantatos, J. Clifford, L. Levina, and E. H. Sargent, Nature photonics, **1** (2007) 531-534
- [54] N. Kouklin, Advanced Materials, **20** (2008) 2190-2194
- [55] Visible light communications: Application to cooperation between vehicles and road infrastructures, Proceedings of the 2012 IEEE Intelligent Vehicles Symposium, **(2012)**;
- [56] I. Ashraf, M. Shkir, S. AlFaify, F. Abdel-Wahab, A. M. Ali, M. Sebak, M. A. Al-Juman, and M. Sanaa, Optical Materials, **103** (2020) 109834
- [57] Y. Yalçın, M. Kılıç, and Z. Çınar, Journal of Advanced Oxidation Technologies, **13** (2010) 281-296
- [58] T.-V. Nguyen, J. C. Wu, and C.-H. Chiou, Catalysis Communications, **9** (2008) 2073-2076
- [59] A. Gołębiewska, A. Malankowska, M. Jarek, W. Lisowski, G. Nowaczyk, S. Jurga, and A. Zaleska-Medynska, Applied Catalysis B: Environmental, **196** (2016) 27-40
- [60] I. Ali, M. Suhail, Z. A. Alothman, and A. Alwarthan, RSC advances, **8** (2018) 30125-30147

- [61] A. N. Banerjee, Nanotechnology, science and applications, **4** (2011) 35
- [62] Ş. Sungur, Handbook of nanomaterials and nanocomposites for energy and environmental applications, (2021) 713-730
- [63] C. Tian, S. Huang, and Y. Yang, Dyes and Pigments, **96** (2013) 609-613
- [64] Structural and electrical properties of TiO₂ thin films, Proceedings of the AIP Conference Proceedings, (2016);
- [65] K. Hashimoto, H. Irie, and A. Fujishima, Japanese journal of applied physics, **44** (2005) 8269
- [66] L.-B. Mo, Y. Bai, Q.-Y. Xiang, Q. Li, J.-O. Wang, K. Ibrahim, and J.-L. Cao, Applied Physics Letters, **105** (2014) 202114
- [67] J.-M. Wu, H. C. Shih, and W.-T. Wu, Nanotechnology, **17** (2005) 105
- [68] L. Sun, Y. Yuan, F. Wang, Y. Zhao, W. Zhan, and X. Han, Nano Energy, **74** (2020) 104909
- [69] V. Etacheri, C. Di Valentin, J. Schneider, D. Bahnemann, and S. C. Pillai, Journal of Photochemistry and Photobiology C: Photochemistry Reviews, **25** (2015) 1-29
- [70] T. Ghosh, S. Dhabal, and A. Datta, Journal of applied physics, **94** (2003) 4577-4582
- [71] M. Hirano, C. Nakahara, K. Ota, O. Tanaike, and M. Inagaki, Journal of Solid State Chemistry, **170** (2003) 39-47
- [72] M. Shang-Di, and W. Ching, Physical review. B, Condensed matter, **51** (1995) 13023-13032
- [73] E. Salomatina, A. Loginova, S. Ignatov, A. Knyazev, I. Spirina, and L. Smirnova, Journal of Inorganic and Organometallic Polymers and Materials, **26** (2016) 1280-1291
- [74] J. Zhang, M. Li, Z. Feng, J. Chen, and C. Li, The Journal of Physical Chemistry B, **110** (2006) 927-935
- [75] P. Di, M. Bellardita, and L. Palmisano, Catalysts, **3** (2013) 36-73
- [76] A. Di Paola, G. Cufalo, M. Addamo, M. Bellardita, R. Campostrini, M. Ischia, R. Ceccato, and L. Palmisano, Colloids and Surfaces A: Physicochemical and Engineering Aspects, **317** (2008) 366-376
- [77] C. F. Song, M. K. Lü, P. Yang, D. Xu, and D. R. Yuan, Thin Solid Films, **413** (2002) 155-159
- [78] J.-M. Wu, H. C. Shih, W.-T. Wu, Y.-K. Tseng, and I.-C. Chen, Journal of crystal Growth, **281** (2005) 384-390
- [79] X. Pan, M.-Q. Yang, X. Fu, N. Zhang, and Y.-J. Xu, Nanoscale, **5** (2013) 3601-3614
- [80] H. Zhang, M. Zhou, Q. Fu, B. Lei, W. Lin, H. Guo, M. Wu, and Y. Lei, Nanotechnology, **25** (2014) 275603
- [81] D. Zhang, J. A. Downing, F. J. Knorr, and J. L. McHale, The Journal of Physical Chemistry B, **110** (2006) 21890-21898
- [82] B. Weintraub, Z. Zhou, Y. Li, and Y. Deng, Nanoscale, **2** (2010) 1573-1587
- [83] Z. Li, M. K. Joshi, J. Chen, Z. Zhang, Z. Li, and X. Fang, Advanced Functional Materials, **30** (2020) 2005291
- [84] L. Su, Z. Li, F. Cao, X. Liu, and X. Fang, Journal of Materials Chemistry C, (2022)
- [85] G. Rawat, D. Somvanshi, Y. Kumar, H. Kumar, C. Kumar, and S. Jit, IEEE Transactions on Nanotechnology, **16** (2016) 49-57
- [86] K. K. Paul, P. Giri, H. Sugimoto, M. Fujii, and B. Choudhury, Solar Energy Materials and Solar Cells, **201** (2019) 110053
- [87] X. D. Gao, G. T. Fei, S. H. Xu, B. N. Zhong, H. M. Ouyang, X. H. Li, and L. De Zhang, Nanophotonics, **8** (2019) 1247-1254
- [88] W. Wang, C. Zhang, K. Qiu, G. Li, A. Zhai, Y. Hao, X. Li, and Y. Cui, Materials, **15** (2022) 2737
- [89] J. Bateman, S. Nimmrichter, K. Hornberger, and H. Ulbricht, Nature communications, **5** (2014) 1-5

- [90] R. López, R. Gómez, and S. Oros-Ruiz, *Catalysis today*, **166** (2011) 159-165
- [91] F. Kara, M. Kurban, and B. Coşkun, *Optik*, **210** (2020) 164605
- [92] D. Komaraiah, E. Radha, N. Kalarikkal, J. Sivakumar, M. R. Reddy, and R. Sayanna, *Ceramics International*, **45** (2019) 25060-25068
- [93] L. Kernazhitsky, V. Shymanovska, T. Gavrilko, V. Naumov, L. Fedorenko, V. Kshnyakin, and J. Baran, *Journal of Luminescence*, **166** (2015) 253-258
- [94] B. Choudhury, and A. Choudhury, *Journal of luminescence*, **132** (2012) 178-184
- [95] A. Nila, M. Baibarac, A. Udrescu, I. Smaranda, A. Mateescu, G. Mateescu, P. Mereuta, and C. C. Negrilă, *Journal of Physics: Condensed Matter*, **31** (2019) 375201
- [96] K. Das, S. N. Sharma, M. Kumar, and S. De, *The Journal of Physical Chemistry C*, **113** (2009) 14783-14792
- [97] M. B. Sarkar, A. Mondal, B. Choudhuri, B. K. Mahajan, S. Chakrabartty, and C. Ngangbam, *Journal of alloys and compounds*, **615** (2014) 440-445
- [98] M. Zhang, K. Tuokedaerhan, H.-y. Zhang, and L. Li, *Optoelectronics Letters*, **15** (2019) 81-84

CHAPTER-2

**Photoluminescence and photodetection properties of
TiO₂ and TiO₂-based structures: An overview**

2.1 Introduction

In 1972, after the great achievement of photoelectrochemical water splitting by Fujishima and Honda [1], the field of photoelectrochemistry has received a significant boost in attention and paved the way for the role of TiO_2 in numerous energy-based applications [2-10]. It is very much known that TiO_2 is used as an excellent photocatalyst [11-15]. Besides photocatalysis, TiO_2 is also an eligible and promising candidate for various photophysical applications due to its superior optoelectronic properties as discussed in previous chapter 1 [16-18]. Commonly, photoexcitation or any subsequent process that does not involve any chemical change is called as photophysical process such as photoluminescence (PL) and photodetection. Among the extensive applications using physical and surface chemical properties of TiO_2 , the study of the surface defect states of TiO_2 plays a vital role in its electrical, chemical, and optical properties [19, 20]. PL and photodetection properties of TiO_2 have been studied extensively as both properties provide the significant informations about the photogenerated electron-hole separation, recombination, and their trapping at defect sites [21, 22]. But as said in previous chapter, the optical absorption of pristine TiO_2 restricts its photoactivity in the UV fraction of solar light, which accounts for only 3-5% of the solar energy [23, 24]. Therefore, as mentioned in the earlier chapter, many approaches have been attempted to extend its absorption in the visible range such as doping, photosensitizing, making a composite, etc. Literature data shows that the optoelectrical properties of TiO_2 significantly depend on the method of its synthesis and purification, structure and morphology, its surface state, and the way of its treatment [18, 25-27]. Therefore, this chapter presents a brief status review of the above mentioned photophysical properties of TiO_2 and TiO_2 -based materials followed by a discussion on defects present in TiO_2 .

2.2 Photoluminescence property

PL provides a measure of recombination of the photogenerated excitons while a recombination may be radiative or non-radiative. For semiconducting materials, the most common radiative transition is between the conduction band (CB) and the valence band (VB) termed as band edge emission. Radiative transitions in semiconductors may also involve localized defects or impurity levels, therefore, the analysis of the PL spectrum also leads to the identification of defects or impurities present in the material. Excitons can be classified into two types; free exciton and bound exciton. Bound excitons can be bound to the donor; called donor bound or to the acceptor; called acceptor bound [28, 29]. The electronic states of bound

excitons strongly depend on the type of semiconducting materials hence the band structure of the materials [30, 31]. Therefore, the PL property is also a measure of the purity of the crystalline structure of a material.

Luminescence from a wide band-gap semiconductor is usually due to two reasons named as band edge emission and defect mediated emission [32, 33]. Since in this thesis work, PL property has been studied broadly, a comprehensive overview of the PL properties of TiO₂ and TiO₂-based materials is presented in the next section.

2.2.1 PL properties of TiO₂

TiO₂ can be grown in nanostructured bulk or thin film form on a substrate. The shape and size of the bulk nanocrystals depend on the surface energy and experimental conditions whereas that for nanostructured films depend on the lattice mismatch with the substrate, substrate roughness, and growth conditions. There are enormous numbers of reports on different types of nanostructured TiO₂ synthesized by various methods [34-39]. In this section, we will discuss the PL properties of TiO₂ grown via various synthesis procedures.

Structural control constitutes one of the major challenges in the design of a suitable coating process for use in specific applications. Among many synthesis procedures, radio frequency (RF) magnetron sputtering can produce highly uniform films having good adherence to the substrate [40, 41]. Various parameters such as sputtering pressure, sputtering power, substrate temperature, types of sputtering gas, etc can change the structural and optical properties of thin films prepared by this method. Nair et al. [42] have synthesized TiO₂ films by this method and reported that annealing temperature has a vital effect on the room temperature PL (RT PL) properties of TiO₂ films. As the growth temperature has been varied from 573K to 1073K, both UV and visible peak intensities and the peak positions of the PL spectra have been changed. The inter-band transition has been assigned for UV emission whereas the transition of electrons from the shallow donor level of oxygen vacancy (V_O) states to the VB is for visible emission obtained in the PL spectra. The variation in the peak positions of band edge emission has been attributed to different concentrations of native defects present in the crystal. The decrease in PL intensity at higher annealed TiO₂ films has been attributed to thermal quenching. Liu et al. [43] have also prepared sputtered TiO₂ films on quartz substrates with some variation of post-growth treatments and discussed their PL properties. A broad emission band has been reported to be formed in the region of 350 to 550 nm for all the samples where the UV peak at 368 nm has been ascribed to direct electron-hole recombination. The

shoulder peaks at 496.5 and 486.5 nm have been attributed to indirect recombination via defects with the interaction of phonons in the TiO₂ lattice. The study of defect levels through PL spectra in TiO₂ thin films deposited by magnetron sputtering has also been reported by Abdullah et al. [19] and their PL results show the profound effect of annealing temperature on the defect levels of V_O and Ti³⁺ at Ti interstitials site. They have also found that increases in temperature reduce the V_O related defects in TiO₂. The sol-gel process is considered as one of the suitable methods to obtain semiconducting oxide films because of low cost, ambient processing temperature and simple synthesis route [44-47]. Also, the quality of the films like homogeneity, stoichiometry, and purity can be easily achieved, ease of processing and control of composition, and the ability to coat on large area substrates [48-50]. Senthil et al. [51] have prepared TiO₂ films by the sol-gel method and discussed the PL properties of these films followed by annealing at two different temperatures. Both the spectra exhibit a broad band PL in the region of 350 to 550 nm. Self-trapped excitons (STE) located or trapped on Ti octahedra have been attributed to main cause of PL emission in anatase TiO₂ film. They have also discussed that the peak at 449 nm in the 350 °C annealed film and the shoulder peak at 446 nm in the 550 °C annealed film can be due to oxygen related defects which is a prominent intrinsic defect in TiO₂ lattice. The thickness of the film is a very crucial factor for measuring PL property. Malliga et al. [52] have reported that with increasing film thickness, intensity of PL band of sol-gel grown TiO₂ films has been enhanced. Rawat et al. [53] have prepared TiO₂ films by another method, electron beam evaporation (EEB) and also by sol-gel method and compared their PL properties. The sol-gel derived films provide more prominent and intense UV peak in PL spectra than the other one. Both the films exhibit a strong peak at ~ 413 nm which has been assigned to near band edge emission (NBE) while the other peaks in the visible region have been assigned to the surface states, V_O, and bulk defects.

Besides the thin films, there are several other nanostructures of TiO₂ which exhibit good UV as well as visible emission properties. TiO₂ nanorods (NRs) grown on the sapphire show a UV peak at 396 nm as a result of free excitons recombination as reported by Wu et al. [54] They have concluded the low intense green emission band in the PL spectra due to the presence of low oxygen related defect concentration in TiO₂ sample. Rajabi et al. [22] have synthesized TiO₂ NRs on FTO substrates and measured their PL properties with the variation of excitation wavelengths which show that the PL property of TiO₂ NRs strongly depends upon the excitation energy. V_O-Ti³⁺ related states have been assigned for the emission peaks at visible region. They have also discussed the effect of growth conditions on the PL property of TiO₂

NRs. Change in growth conditions changes the UV peak intensity but the peak positions remain unaltered. The detailed analysis of both UV and defect mediated visible PL emission has been reported in TiO₂ nanofibers (NFs) by Chetibi et al. [55] They have deconvoluted the broad PL band into six Gaussian sub-bands centered at 3.2 eV, 2.7 eV, 2.5 eV, 2.3 eV, 2 eV and 1.9 eV and thoroughly discussed the correlation of the peaks with the defects present in the sample. According to their report, the peak at 3.2 eV corresponds to band edge emission and the other emissions have been attributed to three kinds of physical origins; STE, V_O, and surface states. De-excitation from lower levels in Ti³⁺ 3d states of TiO₂ lattice to the deep levels (acceptor) created by OH⁻ states have been assigned for appearing the peaks at 463 and 591 nm. Choudhury et al. [56] have synthesized TiO₂ NPs which exhibit both UV and visible emission. The multi-peaks in the visible emission spectra are mainly associated with the excitons and oxygen defects related shallow and deep trap centers. The emission peak at 431 nm has been assigned to STE. The other two peaks centered at 460 and 535 nm have been assigned to F or F²⁺ and F⁺ color centers respectively where the F center is V_O with two trapped electrons, F⁺ is V_O with one trapped electron, and F²⁺ is the V_O with no trapped electrons. Green emission is a very familiar characteristic of anatase TiO₂ which is mainly originated from V_O related states [57-59]. TiO₂ also exhibits red emission. A red band at 600 nm and a green band at 515 nm in atomic layered deposited (ALD) TiO₂ films have been reported by Jin et al. [60] The under-coordinated Ti³⁺ defects have been attributed to the red band and the green band is due to the V_O located on the (101) surface of the films. The increase in annealing temperature causes a blue shift in the PL spectra which has been assigned for transition of under-coordinated Ti atoms to surface V_O with increasing temperature from 800 °C to 900 °C in N₂ atmosphere. Pallotti et al. [61] have also reported red PL in anatase TiO₂ films. Radiative recombination between free holes and electrons that relax from CB and shallow sub-gap states to deep defect states have been attributed to the red emission in TiO₂.

2.2.2 PL properties of TiO₂-based composites

Composites are heterogeneous materials composed of more than one material to obtain a combination of the individual properties of its constituents. Nanocomposites are nothing but amalgamations of varying materials, combined together in nanoscale dimensions [62, 63]. This technology utilizes the strongest features of different elements and combines them into one entity to bring about the most efficient functionality. That's why nanocomposites have received great scientific and industrial attention in various fields [64-67]. TiO₂-based nanocomposites also are not the exception. Sridevi et al. [68] have synthesized ZnO-TiO₂ nanocomposite via

the sol-gel process and reported its PL property. In PL spectra, NBE found at 430 nm has been red shifted in composite sample which has been attributed to the de-excitation of Ti^{3+} 3d states of ZnO-TiO₂ lattice from the lower vibronic level to the deep trap levels. The presence of several types of defects like zinc interstitials (Zn_i), oxygen interstitials (O_i), zinc vacancy (V_{Zn}), V_{O} have been reported. Avci et al. [69] also have studied PL properties of ZnO-TiO₂ nanocomposites synthesized by submerged direct current (DC) arc discharge. A broad PL band with multiple emission peaks of both TiO₂ and ZnO has been observed. The band at 3.26 eV is due to the free exciton recombination of TiO₂ and blue emission band at 2.92 eV is due to presence of both phases of the TiO₂-ZnO nanocomposites. The intense emission band centered at 3.18 eV due to the free exciton-related NBE emission of ZnO NRs due to the recombination of the free exciton through an exciton-exciton collision process. Wang et al. [70] have chosen sub-stoichiometric tungsten oxide (WO_{3-x}) with TiO₂ matrix which is basically WO₃ structure with V_{O} and shown that TiO₂/WO_{3-x} hybrid nanomaterials exhibit multi-color including UV, blue, green, and red PL band. The UV band has been attributed to band edge emission where blue PL bands (435-448 nm) have been associated with the recombination of photogenerated electrons and holes via the V_{O} with two trapped electrons. Surface states of TiO₂ have originated the green PL band and the transition between the gap state and the VB has been attributed to red and infrared emission. Badhe et al. [71] have prepared CdS@TiO₂ nanoparticles by two-step low temperature solvothermal method and reported that both pristine TiO₂ and CdS@TiO₂ NPs show two sharp emission bands at 402 and 428 nm, which are due to TiO₂ NPs. The additional emission band in CdS@TiO₂ nanoparticles in the red region at 500-600 nm has been attributed to presence of CdS but the overall PL intensity of the composite sample has been reduced which indicates better charge separation and lower electron-hole recombination.

2.2.3 PL properties of doped TiO₂

Doping is an intentional introduction of impurity elements into semiconductor for the purpose of modulating and modifying their electrical, optical, and structural properties. Doping in semiconducting metal oxides creates defect states in the band-gap and modulate its optical properties [72-75]. Metal or non-metal doping is preferable as a feasible method to alter the wide band-gap material, owing to its ability to decrease the band-gap and expand the absorption in the visible range. Loan et al. [76] have studied the effect of Zn doping in PL properties of anatase TiO₂ nanowires (NWs) synthesized by hydrothermal technique and reported that incorporation of Zn^{2+} ions into the TiO₂ lattice leads to a strong enhancement in PL intensity

compared to undoped TiO₂. TiO₂ doped with 0.1% Zn has introduced a strong peak located at 2.96 eV and enhanced the intensity of peaks at 2.65, 2.76 and 2.83 eV significantly. According to the report, replacing Ti⁴⁺ ions with Zn²⁺ ions creates V_O states and shallow defects associated with V_O which are responsible for the enhanced luminescence of Zn²⁺ doped TiO₂ NWs. Jing et al. [77] have also discussed that Zn dopant has a great effect on the PL intensity of sol-gel grown TiO₂ NPs. According to their report, with increasing the Zn content, the intensity of PL spectra has been increased but no additional peak has appeared. But for 3% Zn doping, the PL intensity of the sample has been decreased. The PL spectra of all samples have shown two intense peaks at 420 and 480 nm which have been attributed to presence of V_O. Different levels of sub-bands resulting from the V_O are located near the bottom of the CB, and these states easily trap photoinduced electrons to further give rise to PL signals. Cr can be another transition metal dopant that may act as a trapping centre for the enhancement of emission properties in TiO₂. Both Cr doped rutile and anatase TiO₂ NPs have been prepared by Kernazhitsky et al. [78] and found that both undoped and Cr doped TiO₂ samples exhibit broad PL spectra with similar curve patterns, while the intensity of PL spectra of doped samples has been changed. It has been observed from their study that in Cr doped rutile TiO₂, the emission peaks at 2.70-2.75 eV have become narrower and a new peak at 2.78 eV appears. The new peak has been assigned to ⁴T₁→⁴A₂ transition in Cr³⁺. For Cr doped anatase TiO₂, blue and red shifts of the PL peaks are due to the Burstein-Moss and band tailing effects, respectively. The anatase samples with low concentrations of Cr³⁺ ions (0.5 at%), the intensity of PL band has been increased compared to the undoped TiO₂ due to the formation of more radiative recombination centers. At higher contents of Cr³⁺ (1.0 at%), the PL intensity decreases due to the concentration quenching effect. Morphology can be an important factor in luminescence properties of metal oxides. Das et al. [79] have developed three types of Co doped TiO₂ nanostructures namely NRs, NWs, and, nanotubes (NTs) via simple solvothermal process, and compared their PL properties. While doping, Co has been incorporated into the TiO₂ lattice as Co²⁺ and V_O have been created due to the substitution of the Ti⁴⁺ ions by Co²⁺ ions which leads to a significant change in the PL properties of doped TiO₂. The higher intensity of emission peaks with a higher doping concentration of Sn in sol-gel TiO₂ films due to formation of more V_O states have been reported by Rajeswari et al. [80] Non-metal doping has also been considered as a promising way to change the optical absorption of TiO₂. Dong et al. [81] have synthesized C doped TiO₂ followed by heat treatment at 200 °C and reported a broad visible PL band centered at 570 nm. The PL intensity has been decreased in the heat-treated sample compared to un-treated sample. Here also, shallow trap levels associated with V_O have been considered as a reason behind the

visible PL band and reduction of these defects due to heat treatment has been suggested as the removal of oxygen related defects which is also reported by Zhang et al. [82] The emission intensity has been significantly weakened in hydrothermally grown N doped TiO₂-graphene composite as reported by Khalid et al. [83] As the PL is nothing but the electron-hole recombination, the results have suggested that charge carriers have been separated more effectively due to the cooperative effect of N and graphene.

2.3 Photodetection properties of TiO₂

It has been observed that in the last few decades the photodetectors (both UV and UV to visible broad-band) based on TiO₂ have been acquired engrossing achievements due to their intrinsic photoresponse mechanism along with the various advantages as mentioned in the earlier chapter. The basic quality of a photodetector is determined by some quantities named below:

Sensitivity (photo-to-dark current ratio): Photo-to-dark current ratio or sensitivity (S) is a basic characteristic of a photodetector. S is a unitless ratio of photocurrent (I_{ph}) to dark current (I_d) and can be expressed as: $S = I_{ph}/I_d$ [84]. In absence of light, I_d flows in the circuit due to impurity and thermal excitations in a photodetector.

Responsivity: Responsivity or photoresponsivity (R) is a measure of the gain of a detector based on illumination intensity. R is usually expressed in A/W in S.I. unit. Usually, the R value is dependent on spectral region intensity and output current. Mathematically, it is expressed as [85]:

$$R = \frac{I_{ph}}{P \times A} \quad (2.1)$$

where P is the input illumination power density

Detectivity: Detectivity of a photodetector is a figure of merit used to characterize the performance of a photodetector. It is commonly expressed in Jones (cm. $\sqrt{\text{Hz}}$ /W), in the honor of Robert Clark Jones, who originally defined it [86]. D value of a photodetector is dependent on R and I_d values and can be represented as:

$$D = \frac{R_\lambda}{\sqrt{2qJ_d}} \quad (2.2)$$

where q is the charge of an electron and J_d is the dark current density of the detector

In the next section, TiO₂ and TiO₂-based materials will be discussed as conventional UV as well as visible photodetecting materials.

2.3.1 UV photodetection properties of TiO₂ and TiO₂-based materials

The wide band-gap of TiO₂ has established itself as an efficient UV photodetector. Xing et al. [87] have synthesized epitaxial TiO₂ thin films on LaAlO₃ single crystal substrates by RF magnetron sputtering technique which exhibit a maximum responsivity of 3.63 A/W at 310 nm UV irradiation at 10 V bias condition. The three order of UV to visible rejection ratio specifies visible blindness of the films. High quality TiO₂ films on LaAlO₃ substrates by pulsed laser deposition (PLD) method have also been reported by Zhang et al. [88]. They have claimed a high photo-to-dark current ratio of order ~ 6 and high responsivity of 0.21A/W at 5 V bias under 270 nm UV light. TiO₂ films on glass substrates prepared by magnetron sputtering show responsivity of 2.2×10^{-4} and photosensitivity of 32.25 with a fast response with a rise time of 0.98 s and fall time of 3.12 s at 4 V bias under 365 nm UV light has been reported by Gu et al. [89] A comparative study of UV detection properties of TiO₂ films on p-Si substrates fabricated using two different deposition techniques namely the electron-beam evaporation and sol-gel has been illustrated by Rawat et al. [53] The samples have shown photoresponsivity value of ~ 0.69 and ~1.25 A/W at a bias of -10 V for electron beam evaporated and sol-gel derived samples respectively. The enhanced responsivity in the sol-gel based photodetectors has been attributed to the modification of adsorbed oxygen species at the surface of the TiO₂ films under illumination and trapped incident photons. Kumbhar et al. [90] have developed TiO₂ film-based metal-semiconductor-metal (MSM) UV photodetector by hydrothermal method with a high photocurrent of 3.96 μ A and responsivity of 13.29 A/W under 365 nm illumination at 5 V bias. Post-growth treatments of TiO₂ have a great effect on its photoresponse properties. Car et al. [91] have shown that annealing in oxygen preserves the stoichiometry of TiO₂ films and hence exhibits faster photoconductivity in TiO₂ films in UV region where annealing in H₂ and N₂, TiO₂ loses their photoconductive characteristic due to non-stoichiometry. Doping in TiO₂ also can enhance UV photodetection properties. Enache et al. [92] have prepared Fe doped and C doped TiO₂ films and observed that C doped TiO₂ films exhibit 16 times larger photoresponse than that of undoped TiO₂ where Fe doped films do not exhibit a significant change in photoresponse under 330 nm UV light. The enhancement in UV photoconductivity has been attributed to the changes in the electronic structure of the material due to the incorporation of C. Perez et al. [93] have observed UV photoconductivity properties of Er doped TiO₂ by sol-gel method. They have shown that 7 at. % Er³⁺ doped TiO₂ exhibits the higher photosensitivity

of 2.08×10^4 compared undoped sample and a further increase in doping concentration leads to a decrease in photoresponse. The presence of more traps and/ or recombination centers and the loss of crystallinity of the sample have been attributed as the cause for this. Besides the thin films, various morphologies of nanostructured TiO_2 have been reported for UV detection. Mahapatra et al. [94] have grown TiO_2 NR array on ordinary glass substrates and measured UV photosensitivity followed by annealing in different ambiances. They have found a maximum photo-to-dark current ratio of 7.1×10^3 upon 350 nm UV light for H_2 annealed sample due to generation of Ti^{3+} surface defects below the CB when annealed in H_2 under a high vacuum. A fast UV sensitive anodic TiO_2 NT-based photodetector with photo-to-dark current ratio of 10^4 has been reported by Zou et al. [95] The photoresponsivity value of 13 A/W has been obtained under 312 nm of UV illumination with a power density of 1.06 mW/cm^2 at 2.5 V bias. The internal gain induced by the desorption of oxygen and the reduction of the Schottky barrier of Ag electrode and TiO_2 have been considered as the cause of enhancement of responsivity. Wang et al. [96] have fabricated TiO_2 NT array/monolayer graphene film-based UV detector with responsivity, photo-to-dark current ratio, and detectivity values of 15 A/W, 51, and 1.5×10^{12} Jones respectively due to extension of carrier lifetime and lower barrier potential for electron transfer under 365 nm UV illumination.

The basic principle involved in UV photodetection in photoconductive mode is that when the photogenerated electrons and holes due to the UV illumination are separated by an external driving force. Like other wide band-gap semiconductors, in TiO_2 , upon UV illumination, the electron-hole pairs are generated and recombined simultaneously. In this case, oxygen molecule adsorption and desorption on the film's surface play an imperative role in photoconduction [97]. In dark condition, oxygen molecules from the air are easily adsorbed on the TiO_2 surface and due to their high electronegativity, they capture electrons from the bulk which leads to the formation of a low conductivity depletion region near the surface [98].



Upon UV illumination, the electron-hole pairs are created and the photogenerated holes migrate to the surface along the potential gradient produced by band bending and the oxygens are desorbed from the surface.



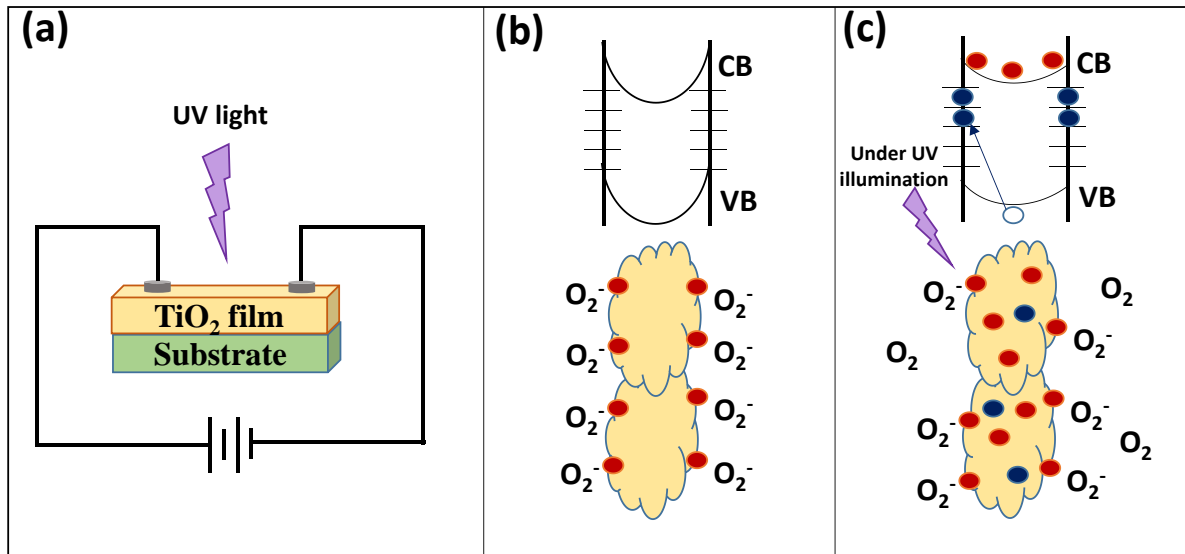


Fig. 2.1: Photocurrent transport mechanism in TiO_2 thin film. (a) Schematic illustration of TiO_2 thin film-based UV photodetector. (b) Adsorption of oxygen molecules on the surface of TiO_2 thin film in the dark and the upward band bending. (c) Under UV illumination, some of the photogenerated holes migrate to the TiO_2 thin film surface due to the desorption of adsorbed oxygen molecules. This effectively decreases the resistive depletion layer width of the TiO_2 thin film.

The unpaired electrons are either collected at the anode or recombined with a hole when oxygen molecule is reabsorbed on the surface of TiO_2 . It results a decrease in the free carrier concentration and a decrease in the width of the depletion layer. This leads to an enhancement of carrier concentration, producing an enhancement in current. So, the photoresponse of TiO_2 depends on two factors; a fast process of photo generation of carriers followed by recombination of electron-hole pairs, and a slow process of surface adsorption and desorption of oxygen molecules. After a certain time, these two processes balance each other that gives consistent photocurrent.

2.3.2 Visible photodetection properties of TiO_2 and TiO_2 -based materials

As discussed earlier, the large band-gap of TiO_2 is a considerable disadvantage for solar light-based applications and therefore, a major goal in this research field is directed to make visible photoactive TiO_2 . In the next section, several approaches to get visible photodetection from TiO_2 and TiO_2 -based materials will be discussed.

In semiconductor physics, doping is a very fundamental process that can introduce a donor or acceptor state in the band-gap and tune the optical and electrical properties according to the demands as mentioned previously. In the case of TiO_2 , both metal and non-metal elements can be incorporated into TiO_2 matrix as dopants for enhanced visible photodetection. Kara et al. [99] have reported a photocurrent enhancement in sol-gel derived Fe doped TiO_2 films under solar light. The decrease of band-gap energy due to doping has been considered as the reason behind it. Ghicov et al. [100] have reported an increase in visible photoresponse properties in TiO_2 NTs due to Cr doping due to formation of defect states which act as recombination centers for the photogenerated charge carriers. A maximum of 2.5 times enlarged photodetection at -3.5 V bias has been observed in In doped TiO_2 thin film under white light illumination [101]. Here also, doping introduces mid-gap levels in TiO_2 which causes visible photoresponse. N doped single TiO_2 NW has been prepared by Wu et al. [102] and they have reported that under blue light (457 nm), the device shows a responsivity value of 8 A/W with the power density of 40 mW/cm^2 at 1 V bias with response time only 0.5 s. Impurity N atoms create an energy (N_{2p}) level at about 0.75 eV above the VB and electrons in the VB and localized N_{2p} levels are excited by photons with lower energy, which result in noteworthy enhancement of visible light absorption in TiO_2 . Ngangbam et al. [103] have prepared Ag doped TiO_2 NWs on n-type Si substrate and fabricated n-Si/ TiO_2 NWs/Ag- TiO_2 /Au device. The device shows maximum photosensitivity at -4 V bias under white light illumination due to the hole trapping process.

Hybrid devices, based on organic conjugated polymers and inorganic semiconductors are active materials and due to their opportunity to the combine the valuable properties of both materials groups, particularly in terms of charge generation and transport, they have attracted considerable attention in the current area of research [104-107]. For this purpose, organic dye sensitization is a beneficial approach to get visible absorption from wide band-gap semiconducting oxides like TiO_2 [108-110]. Additionally, wavelength selectivity can be achieved using organic dyes with different absorption spectra. The basic mechanism involved is that the TiO_2 with a high surface area acts as the dye molecule supporting layer and allows the conduction of electrons (electron injection by the photoexcited dye molecule into the film) to the electrodes [111]. Parreira et al. [112] have fabricated TiO_2 NRs array films sensitized with the commercially available ruthenium complex N719, and two new coumarin dyes, C1-LEN and C2-LEN and shown that the devices exhibit maximum 6 orders of photo-to-dark current ratio under the visible range of the spectrum.

Although the above discussed efforts have resulted in improvements in the visible light response of TiO₂, but some drawbacks are still there. The inherently unavoidable trap centers created by dopants, photobleaching of the dyes, and the complication of fabrication methods in dye sensitization still limit the performance of TiO₂-based visible photodetector. In this scenario, noble metal incorporated TiO₂ can be an alternative and useful option to extend the absorption of TiO₂ in the visible spectral range. The noble metals (Au, Ag, Pt, Pd) exhibit unique optical properties due to the interaction between the conduction electrons of the metal NPs with the photons of the incident polarized light which causes collective oscillations. It leads to a strong enhancement of the local electromagnetic field surrounding NPs which is called localized surface plasmon resonance (LSPR) [113-115]. The combination of appropriate plasmonic metal and semiconducting oxide forms a metal-semiconductor Schottky or Ohmic junction depending on their work functions that can transform incident light energy to other forms of energy via the plasmonic hot-carriers leading to wide applications in photophysical and photochemical areas [116-118]. Mainly, these noble metals modified TiO₂ are widely used in the research field of photocatalysis and very few reports on the study of photodetection have been found to the best of our knowledge. This kind of photodetector has an additional advantage of tuning spectral response peak by simply adjusting the shape, size, and interparticle distance of metal NPs [119, 120]. Chen et al. [121] have synthesized plasmonic Au-TiO₂ composite films on FTO substrates by the sputtering technique. They have reported that while Au loading, a drastic change of photocurrent density has been observed for the composite films upon the visible light (550 nm) irradiation and the photocurrent value increases with the thickness of Au film on TiO₂ due to LSPR. Au-TiO₂ nanocomposite electrode also have been prepared by the electrophoretic deposition of Au NPs into a porous nanoparticulate TiO₂ film as reported by Brennan et al. [122] Photocurrent increases for the composite films under 520 nm light that has been attributed to the generation and separation of plasmonic hot-electrons at the interface and also the inter-band generation of holes in Au NPs by visible photons. Due to the advantages of the narrow energy distribution of plasmonic hot-electrons in Ag and the high density of states in the TiO₂ CB, Ag-TiO₂ composite is considered as an appropriate pair to develop plasmonic photodetector [123, 124]. Porous Ag-TiO₂ Schottky-diode based plasmonic photodetector with enhanced photo-to-dark current ratio and high responsivity under 450 nm incident radiation has been fabricated by Gao et al. [121] due to plasmonic hot-electrons. Wang et al. [125] have fabricated graphene quantum dot (GQD) sensitized Ag/TiO₂ films and noticeable photocurrent with fast response has been observed in Ag/TiO₂ and GQDs/Ag/TiO₂ films under visible light. The enhanced photoresponse has been attributed to the shift of hot-

electrons from Ag NPs and GQDs to TiO_2 under visible light. Paul et al. [126] have also suggested that plasmonic hot-electrons are responsible in visible photoresponse in Ag- TiO_2 . Significant enhancement in photocurrent in Ag- TiO_2 and Ag- TiO_2 - C_3N_4 composites over bare TiO_2 under several visible (470, 510, and 545nm) illuminations has been reported. They have claimed that the increase in photocurrent is due to the contribution from Ti^{3+} excitation, hot-electron injection, and charge transfer from TiO_2 to C_3N_4 .

2.4 Defects in TiO_2

Native structural defects are imperfections in the crystal lattice that include only the constituent elements [127]. The concentration of these defects depends on their formation energy, which is dependent on the growth condition or post-growth annealing condition and position of the Fermi level [128]. Defects usually exist in all laboratory grown crystals [129]. As a simple binary oxide, TiO_2 exhibits very rich defect chemistry as stated earlier. The fundamental native point defects identified in TiO_2 are Ti vacancy (V_{Ti}), V_{O} , Ti interstitial (Ti_i), and O interstitial (O_i). Among these, Ti_i , V_{O} are well known as the donor type defects where V_{Ti} , O_i are known as the acceptor type defects. As V_{O} has higher formation energy than that of Ti_i , the kinetic barrier for creating V_{O} in a perfect TiO_2 is expected to be lesser than that for creating Ti_i . However, post-growth creation of V_{O} is possible, particularly after the sample has been heated for a prolonged time or at high temperature [130]. V_{Ti} is the lowest energy acceptor in TiO_2 . Thus, in undoped and non-heat treated samples, Ti_i and V_{Ti} should be the principal donor and acceptor, respectively. However, according to literature V_{O} is the significant and supposed to be the prevalent defect in TiO_2 [131-134]. In principle, the formation of V_{O} on TiO_2 leads to the creation of unpaired electrons or Ti^{3+} centers, which creates an overall reduced state of the TiO_2 crystal, both in the bulk and in the surface. Zuo et al. [135] have reported that the presence of a defect state closely below the CB minimum, which is attributed to the V_{O} with Ti^{3+} and is the responsible for the band-gap narrowing in TiO_2 . The presence of both $\text{Ti}^{3+}_{\text{lattice}}$ and Ti_i^{3+} species results in new states in the band-gap which is about 1-1.5 eV below the CB of TiO_2 as discussed by Finazzi et al. [136] The defect levels of TiO_2 can be categorized into two types namely electron trap and hole trap [137]. Abdullah et al. [138] have reported that the electron trap states are associated with Ti_i or/and Ti^{3+} defects which is at 0.7-1.6 eV below the CB within the band-gap whereas the hole trap states are estimated to be located at 2.50 and 2.29 eV. Pan et al. [131] also has also identified V_{O} as the major defect observed in TiO_2 and the energy level of this localized donor states originating from V_{O} is located at 0.75-1.18 eV below the CB of TiO_2 .

2.5 Conclusions

From the above review, it is noted that the existence of structural defects, such as V_O, surface oxygen in the TiO₂ has a direct influence in its photophysical properties mainly PL and photodetection as they often behave like trapping centers for the charge carriers to prolong the charge carrier generation and recombination time under UV illumination. Therefore, to improve the above mentioned properties, it is important to tune structural defects in TiO₂ through surface modification, formation of complex heterostructure, post-growth annealing, etc. The various way of getting visible photoresponse of TiO₂ and TiO₂-based materials also have been discussed which are very effective and promising in the field of applications.

2.6 References

- [1] A. Fujishima, and K. Honda, *nature*, **238** (1972) 37-38
- [2] R. Abe, *Journal of Photochemistry and Photobiology C: Photochemistry Reviews*, **11** (2010) 179-209
- [3] T. Ochiai, and A. Fujishima, *Journal of Photochemistry and photobiology C: Photochemistry reviews*, **13** (2012) 247-262
- [4] X. Lü, B. Xia, C. Liu, Y. Yang, and H. Tang, *Hindawi*, (2016)
- [5] Q. Zhou, Z. Fang, J. Li, and M. Wang, *Microporous and Mesoporous Materials*, **202** (2015) 22-35
- [6] V. Anitha, A. N. Banerjee, and S. W. Joo, *Journal of materials science*, **50** (2015) 7495-7536
- [7] R. Pessoa, M. Fraga, L. Santos, M. Massi, and H. Maciel, *Materials Science in Semiconductor Processing*, **29** (2015) 56-68
- [8] A. Fujishima, K. Kohayakawa, and K. Honda, *Journal of the Electrochemical Society*, **122** (1975) 1487
- [9] Y. Li, H. Yu, C. Zhang, W. Song, G. Li, Z. Shao, and B. Yi, *Electrochimica Acta*, **107** (2013) 313-319
- [10] C. Y. L. J. C. CJ, *Photobiol.*, **A**, **400** (2020) 112666
- [11] Y. Wang, H. Yang, and W. Zou, *Materials Letters*, **254** (2019) 54-57
- [12] Z. Xing, J. Zhang, J. Cui, J. Yin, T. Zhao, J. Kuang, Z. Xiu, and N. Wan, *Recent Advances in Floating TiO₂-Based Photocatalysts for Environmental Application.* *Applied Catalysis B: Environmental*, **225** 452-467
- [13] R. Wang, K. Hashimoto, A. Fujishima, M. Chikuni, E. Kojima, A. Kitamura, M. Shimohigoshi, and T. Watanabe, *Google Scholar* There is no corresponding record for this reference,
- [14] R. Zuo, *Advances in Materials Science and Engineering*, (2014) 170148
- [15] J. Schneider, M. Matsuoka, M. Takeuchi, J. Zhang, Y. Horiuchi, M. Anpo, and D. W. Bahnemann, *Chemical reviews*, **114** (2014) 9919-9986
- [16] U. M. Nayef, K. A. Hubeatir, and Z. J. Abdulkareem, *Materials Technology*, **31** (2016) 884-889

- [17] N. Yang, G. Li, W. Wang, X. Yang, and W. Zhang, *Journal of Physics and Chemistry of Solids*, **72** (2011) 1319-1324
- [18] A. F. Khan, M. Mehmood, S. Durrani, M. Ali, and N. Rahim, *Materials Science in Semiconductor Processing*, **29** (2015) 161-169
- [19] Photoluminescence study of trap-state defect on TiO₂ thin films at different substrate temperature via RF magnetron sputtering. *Proceedings of the Journal of Physics: Conference Series*, (2018)
- [20] N. Hosaka, T. Sekiya, and S. Kurita, *Journal of luminescence*, **72** (1997) 874-875
- [21] Z. Li, Z. Li, C. Zuo, and X. Fang, *Advanced Materials*, (2022) 2109083
- [22] M. Rajabi, and S. Shogh, *Journal of Luminescence*, **157** (2015) 235-242
- [23] W. Wang, *J. Mol. Catal. A: Chem*, **235** (2005) 194-199
- [24] L. Gomathi Devi, and B. Narasimha Murthy, *Catalysis letters*, **125** (2008) 320-330
- [25] G. Kaur, P. Negi, M. Kaur, R. Sharma, R. J. Konwar, and A. Mahajan, *Ceramics International*, **44** (2018) 18484-18490
- [26] C. G. Aba-Guevara, I. E. Medina-Ramírez, A. Hernández-Ramírez, J. Jáuregui-Rincón, J. A. Lozano-Álvarez, and J. L. Rodríguez-López, *Ceramics International*, **43** (2017) 5068-5079
- [27] M. El-Henawey, M. Kubas, A. El-Shaer, and E. Salim, *Journal of Materials Science: Materials in Electronics*, **32** (2021) 21308-21317
- [28] P. Dean, *Physical Review*, **139** (1965) A588
- [29] E. H. Bogardus, and H. B. Bebb, *Physical Review*, **176** (1968) 993
- [30] H. Hosono, *Thin solid films*, **515** (2007) 6000-6014
- [31] B. Monemar, *Journal of Physics: Condensed Matter*, **13** (2001) 7011
- [32] J. Gupta, K. Barick, and D. Bahadur, *Journal of Alloys and Compounds*, **509** (2011) 6725-6730
- [33] J. Foreman, J. Simmons Jr, W. Baughman, J. Liu, and H. Everitt, *Journal of Applied Physics*, **113** (2013) 133513
- [34] T. Y. Y. X. F. RC, *Nano Lett*, **11** (2011) 3026-3033
- [35] Z. Miao, D. Xu, J. Ouyang, G. Guo, X. Zhao, and Y. Tang, *Nano Letters*, **2** (2002) 717-720
- [36] P. Roy, S. Berger, and P. Schmuki, *Angewandte Chemie International Edition*, **50** (2011) 2904-2939
- [37] H. G. Yang, G. Liu, S. Z. Qiao, C. H. Sun, Y. G. Jin, S. C. Smith, J. Zou, H. M. Cheng, and G. Q. Lu, *Journal of the American Chemical Society*, **131** (2009) 4078-4083
- [38] E. Muniz, M. Góes, J. Silva, J. A. Varela, E. Joanni, R. Parra, and P. R. Bueno, *Ceramics International*, **37** (2011) 1017-1024
- [39] X. Feng, J. Zhai, and L. Jiang, *Angewandte Chemie*, **117** (2005) 5245-5248
- [40] Z. Zhang, C. Bao, W. Yao, S. Ma, L. Zhang, and S. Hou, *Superlattices and Microstructures*, **49** (2011) 644-653
- [41] Y. Yang, Y. Zhang, and M. Yan, *Separation and Purification Technology*, (2022) 121627
- [42] P. B. Nair, V. Justinivictor, G. P. Daniel, K. Joy, K. J. Raju, D. D. Kumar, and P. Thomas, *Progress in Natural Science: Materials International*, **24** (2014) 218-225
- [43] L. Baoshun, Z. Xiujian, Z. Qingnan, H. Xin, and F. Jingyang, *Journal of Electron Spectroscopy and Related Phenomena*, **148** (2005)
- [44] J. Livage, F. Beteille, C. Roux, M. Chatry, and P. Davidson, *Acta materialia*, **46** (1998) 743-750
- [45] A. E. Danks, S. R. Hall, and Z. Schnepf, *Materials Horizons*, **3** (2016) 91-112
- [46] H. Dislich, *Journal of non-crystalline solids*, **80** (1986) 115-121
- [47] Sol-gel synthesis of optical thin films and coatings, *Proceedings of the Sol-Gel Optics*, (1990)

- [48] I. Chilibon, and J. N. Marat-Mendes, Journal of sol-gel science and technology, **64** (2012) 571-611
- [49] The role of crystallisation process of ferroelectric ceramic gels on the electroactive properties of sol-gel ceramic/polymer composites, Proceedings of the 10th International Symposium on Electrets (ISE 10). Proceedings (Cat. No. 99 CH36256), (**1999**);
- [50] S. Kazaoui, and J. Ravez, Journal of materials science, **28** (1993) 1211-1219
- [51] T. Senthil, N. Muthukumarasamy, R. Balasundaraprabhu, and C. Kumaran, J. Nanosci. Nanotechnol, **1** (2012) 6-9
- [52] P. Malliga, J. Pandiarajan, N. Prithivikumaran, and K. Neyvasagam, IOSR Journal of Applied physics, **6** (2014) 22
- [53] G. Rawat, D. Somvanshi, H. Kumar, Y. Kumar, C. Kumar, and S. Jit, IEEE Transactions on Nanotechnology, **15** (2015) 193-200
- [54] J.-M. Wu, H. C. Shih, and W.-T. Wu, Nanotechnology, **17** (2005) 105
- [55] L. Chetibi, T. Busko, N. P. Kulish, D. Hamana, S. Chaieb, and S. Achour, Journal of Nanoparticle Research, **19** (2017) 1-9
- [56] B. Choudhury, and A. Choudhury, Physica E: Low-Dimensional Systems and Nanostructures, **56** (2014) 364-371
- [57] F. Labreche, A. Berbadj, N. Brihi, R. Karima, and B. Jamoussi, Optik, **172** (2018) 63-71
- [58] F. J. Knorr, and J. L. McHale, The Journal of Physical Chemistry C, **117** (2013) 13654-13662
- [59] J. L. McHale, C. C. Rich, and F. J. Knorr, MRS Online Proceedings Library (OPL), **1268** (2010)
- [60] C. Jin, B. Liu, Z. Lei, and J. Sun, Nanoscale research letters, **10** (2015) 1-9
- [61] D. K. Pallotti, L. Passoni, P. Maddalena, F. Di Fonzo, and S. Lettieri, The Journal of Physical Chemistry C, **121** (2017) 9011-9021
- [62] S. Lal, D. Mudgal, and P. Gupta, Current Nanomaterials, **1** (2016) 183-189
- [63] H. DM Follmann, A. F Naves, R. A Araujo, V. Dubovoy, X. Huang, T. Asefa, R. Silva, and O. N Oliveira, Current pharmaceutical design, **23** (2017) 3794-3813
- [64] G. Pyrgiotakis, J. McDevitt, A. Bordini, E. Diaz, R. Molina, C. Watson, G. Deloid, S. Lenard, N. Fix, and Y. Mizuyama, Environmental Science: Nano, **1** (2014) 15-26
- [65] J. Joy, E. George, P. Haritha, S. Thomas, and S. Anas, Journal of Polymer Science, **58** (2020) 3115-3141
- [66] J. Liu, Y. Gao, D. Cao, L. Zhang, and Z. Guo, Langmuir, **27** (2011) 7926-7933
- [67] B. Ates, S. Koytepe, A. Ulu, C. Gurses, and V. K. Thakur, Chemical Reviews, **120** (2020) 9304-9362
- [68] K. Sridevia, L. G. Prasad, B. Sangeetha, and S. Sivakumard, JOURNAL OF OVONIC RESEARCH, **18** (2022) 453-464
- [69] A. Avci, V. Eskizeybek, H. Gülce, B. Haspulat, and Ö. S. Şahin, Applied Physics A, **116** (2014) 1119-1125
- [70] B. Wang, X. Zhong, J. Zhu, Y. Wang, Y. Zhang, U. Cvelbar, and K. Ostrikov, Applied Surface Science, **562** (2021) 150180
- [71] R. A. Badhe, A. Ansari, and S. S. Garje, Bulletin of Materials Science, **44** (2021) 1-11
- [72] A. S. Ahmed, M. Singla, S. Tabassum, A. H. Naqvi, and A. Azam, Journal of luminescence, **131** (2011) 1-6
- [73] M. Samadi, M. Zirak, A. Naseri, E. Khorashadizade, and A. Z. Moshfegh, Thin Solid Films, **605** (2016) 2-19
- [74] G. Wang, Y. Yang, D. Han, and Y. Li, Nano Today, **13** (2017) 23-39
- [75] H.-C. Wu, Y.-C. Peng, and T.-P. Shen, Materials, **5** (2012) 2088-2100
- [76] T. T. Loan, V. H. Huong, V. T. Tham, and N. N. Long, Physica B: Condensed Matter, **532** (2018) 210-215

- [77] L. Jing, B. Xin, F. Yuan, L. Xue, B. Wang, and H. Fu, *The Journal of Physical Chemistry B*, **110** (2006) 17860-17865
- [78] L. Kernazhitsky, V. Shymanovska, T. Gavrilko, V. Naumov, L. Fedorenko, V. Kshnyakin, and J. Baran, *Journal of Luminescence*, **166** (2015) 253-258
- [79] K. Das, S. N. Sharma, M. Kumar, and S. De, *The Journal of Physical Chemistry C*, **113** (2009) 14783-14792
- [80] R. Rajeswari, D. Venugopal, A. George, A. D. Raj, S. J. Sundaram, A. Bashir, M. Maaza, and K. Kaviyarasu, *Applied Physics A*, **127** (2021) 1-8
- [81] F. Dong, S. Guo, H. Wang, X. Li, and Z. Wu, *The Journal of Physical Chemistry C*, **115** (2011) 13285-13292
- [82] J. Zhang, X. Chen, Y. Shen, Y. Li, Z. Hu, and J. Chu, *Physical Chemistry Chemical Physics*, **13** (2011) 13096-13105
- [83] N. Khalid, E. Ahmed, M. Ahmad, N. Niaz, M. Ramzan, M. Shakil, T. Iqbal, and A. Majid, *Ceramics International*, **42** (2016) 18257-18263
- [84] S. Mondal, S. Ghosh, and D. Basak, *Materials Research Bulletin*, **144** (2021) 111490
- [85] S. Chen, X. Qiao, F. Wang, Q. Luo, X. Zhang, X. Wan, Y. Xu, and X. Fan, *Nanoscale*, **8** (2016) 2277-2283
- [86] S. Wu, B. Xiao, B. Zhao, Z. He, H. Wu, and Y. Cao, *Small*, **12** (2016) 3374-3380
- [87] J. Xing, H. Wei, E.-J. Guo, and F. Yang, *Journal of Physics D: Applied Physics*, **44** (2011) 375104
- [88] Z. Zhang, L. M. Wong, Z. Zhang, Z. Wu, S. Wang, D. Chi, R. Hong, and W. Yang, *Applied Surface Science*, **355** (2015) 398-402
- [89] P. Gu, X. Zhu, H. Wu, J. Li, and D. Yang, *Journal of Alloys and Compounds*, **779** (2019) 821-830
- [90] S. Kumbhar, S. Shaikh, and K. Rajpure, *Journal of Electronic Materials*, **49** (2020) 499-509
- [91] T. Car, N. Radić, and A. Turković, *Japanese journal of applied physics*, **41** (2002) 5618
- [92] C. S. Enache, J. Schoonman, and R. V. Krol, *Journal of electroceramics*, **13** (2004) 177-182
- [93] J. B. Pérez, M. Courel, R. C. Valderrama, I. Hernández, M. Pal, F. P. Delgado, and N. Mathews, *Vacuum*, **169** (2019) 108873
- [94] A. Das Mahapatra, A. Das, S. Ghosh, and D. Basak, *ACS omega*, **4** (2019) 1364-1374
- [95] J. Zou, Q. Zhang, K. Huang, and N. Marzari, *The Journal of Physical Chemistry C*, **114** (2010) 10725-10729
- [96] M. Z. Wang, F. X. Liang, B. Nie, L. H. Zeng, L. X. Zheng, P. Lv, Y. Q. Yu, C. Xie, Y. Y. Li, and L. B. Luo, *Particle & Particle Systems Characterization*, **30** (2013) 630-636
- [97] S. Studenikin, N. Golego, and M. Cocivera, *Journal of Applied Physics*, **87** (2000) 2413-2421
- [98] A. V. Raghu, K. K. Karuppanan, J. Nampoothiri, and B. Pullithadathil, *ACS Applied Nano Materials*, **2** (2019) 1152-1163
- [99] F. Kara, M. Kurban, and B. Coşkun, *Optik*, **210** (2020) 164605
- [100] A. Ghicov, B. Schmidt, J. Kunze, and P. Schmuki, *Chemical Physics Letters*, **433** (2007) 323-326
- [101] M. B. Sarkar, A. Mondal, B. Choudhuri, B. K. Mahajan, S. Chakrabartty, and C. Ngangbam, *Journal of alloys and compounds*, **615** (2014) 440-445
- [102] P. Wu, X. Song, S. Si, Z. Ke, L. Cheng, W. Li, X. Xiao, and C. Jiang, *Nanotechnology*, **29** (2018) 184005
- [103] C. Ngangbam, N. K. Singh, and A. Mondal, *Journal of Nanoscience and Nanotechnology*, **18** (2018) 5059-5062

- [104] A. L. M. Reddy, S. R. Gowda, M. M. Shaijumon, and P. M. Ajayan, *Advanced Materials*, **24** (2012) 5045-5064
- [105] V. K. Thakur, G. Ding, J. Ma, P. S. Lee, and X. Lu, *Advanced materials*, **24** (2012) 4071-4096
- [106] S. Parola, B. Julián-López, L. D. Carlos, and C. Sanchez, *Advanced Functional Materials*, **26** (2016) 6506-6544
- [107] C. M. Niemeyer, *Angewandte Chemie International Edition*, **42** (2003) 5796-5800
- [108] J. Diaz-Angulo, I. Gomez-Bonilla, C. Jimenez-Tohapanta, M. Mueses, M. Pinzon, and F. Machuca-Martinez, *Photochemical & Photobiological Sciences*, **18** (2019) 897-904
- [109] S. Goulart, L. J. J. Nieves, A. G. Dal Bó, and A. M. Bernardin, *Dyes and Pigments*, **182** (2020) 108654
- [110] G. B. Strapasson, F. R. Scheffer, S. W. Cendron, F. d. C. Silva, N. H. Lazzari, C. Azambuja, A. Peyrot, and D. E. Weibel, *SN Applied Sciences*, **2** (2020) 1-12
- [111] M. Grätzel, *Pure and Applied Chemistry*, **73** (2001) 459-467
- [112] P. Parreira, E. Torres, C. Nunes, C. N. de Carvalho, G. Lavareda, A. Amaral, and M. J. Brites, *Sensors and Actuators B: Chemical*, **161** (2012) 901-907
- [113] K. Y. Kim, *Plasmonics: Principles and Applications*, BoD–Books on Demand, (2012)
- [114] E. Petryayeva, and U. J. Krull, *Analytica chimica acta*, **706** (2011) 8-24
- [115] J.-H. Choi, J.-H. Lee, J. Son, and J.-W. Choi, *Sensors*, **20** (2020) 1003
- [116] A. N. Koya, X. Zhu, N. Ohannesian, A. A. Yanik, A. Alabastri, R. Proietti Zaccaria, R. Krahne, W.-C. Shih, and D. Garoli, *ACS nano*, **15** (2021) 6038-6060
- [117] H. Tang, C.-J. Chen, Z. Huang, J. Bright, G. Meng, R.-S. Liu, and N. Wu, *The Journal of Chemical Physics*, **152** (2020) 220901
- [118] Y. Wy, H. Jung, J. W. Hong, and S. W. Han, *Accounts of Chemical Research*, **55** (2022) 831-843
- [119] C. de Melo, M. Jullien, Y. Battie, A. En Naciri, J. Ghanbaja, F. Montaigne, J.-F. Pierson, F. Rigoni, N. Almqvist, and A. Vomiero, *ACS applied materials & interfaces*, **10** (2018) 40958-40965
- [120] E. Boisselier, and D. Astruc, *Chemical society reviews*, **38** (2009) 1759-1782
- [121] W. Chen, Y. Lu, W. Dong, Z. Chen, and M. Shen, *Materials Research Bulletin*, **50** (2014) 31-35
- [122] L. J. Brennan, F. Purcell-Milton, A. S. Salmeron, H. Zhang, A. O. Govorov, A. V. Fedorov, and Y. K. Gun'ko, *Nanoscale research letters*, **10** (2015) 1-12
- [123] L. V. Besteiro, X.-T. Kong, Z. Wang, G. Hartland, and A. O. Govorov, *Acs Photonics*, **4** (2017) 2759-2781
- [124] J. Bateman, S. Nimmrichter, K. Hornberger, and H. Ulbricht, *Nature communications*, **5** (2014) 1-5
- [125] W. Wang, S. Wang, J. Lv, M. Zhao, M. Zhang, G. He, C. Fang, L. Li, and Z. Sun, *Journal of the American Ceramic Society*, **101** (2018) 5469-5476
- [126] K. K. Paul, P. Giri, H. Sugimoto, M. Fujii, and B. Choudhury, *Solar Energy Materials and Solar Cells*, **201** (2019) 110053
- [127] A. Bera, T. Ghosh, and D. Basak, *ACS Applied Materials & Interfaces*, **2** (2010) 2898-2903
- [128] C. G. Van de Walle, and J. Neugebauer, *Journal of applied physics*, **95** (2004) 3851-3879
- [129] M. Daeumling, J. Seuntjens, and D. Larbalestier, *Nature*, **346** (1990) 332-335
- [130] S. Na-Phattalung, M. F. Smith, K. Kim, M.-H. Du, S.-H. Wei, S. Zhang, and S. Limpijumnong, *Physical Review B*, **73** (2006) 125205
- [131] X. Pan, M.-Q. Yang, X. Fu, N. Zhang, and Y.-J. Xu, *Nanoscale*, **5** (2013) 3601-3614
- [132] H. Li, Y. Guo, and J. Robertson, *The Journal of Physical Chemistry C*, **119** (2015) 18160-18166

- [133] S. Huygh, A. Bogaerts, and E. C. Neyts, *The Journal of Physical Chemistry C*, **120** (2016) 21659-21669
- [134] C. Li, T. Wang, Z. J. Zhao, W. Yang, J. F. Li, A. Li, Z. Yang, G. A. Ozin, and J. Gong, *Angewandte Chemie International Edition*, **57** (2018) 5278-5282
- [135] F. Zuo, L. Wang, T. Wu, Z. Zhang, D. Borchardt, and P. Feng, *Journal of the American Chemical Society*, **132** (2010) 11856-11857
- [136] E. Finazzi, C. Di Valentin, and G. Pacchioni, *The Journal of Physical Chemistry C*, **113** (2009) 3382-3385
- [137] Q. Guo, C. Zhou, Z. Ma, and X. Yang, *Advanced Materials*, **31** (2019) 1901997
- [138] S. Abdullah, M. Sahdan, N. Nafarizal, H. Saim, Z. Embong, C. C. Rohaida, and F. Adriyanto, *Applied Surface Science*, **462** (2018) 575-582

CHAPTER-3

Thin film synthesis and characterization techniques

3.1 Introduction

The properties of semiconductor thin films highly depend on the film synthesis procedures and various parameters associated with them [1-4]. Each synthesis technique produces films with different structural, electrical, optical, and optoelectronic properties. There are several deposition techniques to prepare good quality TiO_2 thin films [5-10]. In this chapter, deposition procedures, those, used in this thesis work are described elaborately followed by a discussion on the various characterization techniques as well.

3.2 Thin film synthesis techniques

There are mainly two broad categories of deposition techniques such as (i) physical vapor deposition (PVD) and (ii) chemically solution deposition (CSD) techniques. There are various examples of these deposition techniques as noted below in the Table. 3.1

Table 3.1. Various thin film deposition techniques

Physical vapor deposition techniques	Chemically solution deposition techniques
DC and RF sputtering	Sol-gel
Pulsed laser deposition	Electro deposition
Electron beam evaporation	Chemical bath deposition
Thermal evaporation	Aqueous chemical growth
Molecular beam epitaxy	Hydrothermal
Atomic layer deposition	Solvothermal

PVD techniques are mainly vacuum-based processes with very good reproducibility rates, hence, greatly favorable for uniform and homogeneous thin film deposition. But, the PVD techniques are more expensive than CSD techniques. In this thesis work mainly sol-gel and thermal evaporation techniques have been used to prepare TiO_2 thin films. For post-growth doping, the ion implantation process has been carried out. In the next section, the above-mentioned techniques will be discussed to some extent.

3.2.1 Chemically solution deposition techniques

CSD technique is a low cost and non-vacuum process. This technique has more control over the morphology and optical properties to fabricate polycrystalline, textured, and epitaxial oxide thin films.

3.2.1.1 Sol-gel

Sol-gel technique is a versatile wet-chemical method that is broadly used for the synthesis of metal oxide films as well as nanostructures. This process goes through four major steps such as the formation of sol, gelation, drying, and annealing. The process begins with choosing a metal alkoxide or inorganic salt as a precursor material and then the formation of a colloidal suspension of this precursor solution (known as ‘sol’) through hydrolysis and condensation reaction. Then the sol follows transformation to an integrated network of either discrete particles or network polymers via polycondensation reactions known as ‘gel’. To improve the stability, often chelating agents are added into the sol. The gel can be shaped into desired forms such as thin films or powder followed by appropriate annealing. The following three reactions at the functional group level are used to describe the hydrolysis and condensation process of the sol-gel reaction [11].



where M is the metal or Si, X is the reactive ligands like halogen O-R, NR_2 , acetate, etc. Equation (3.1) represents the hydrolysis reaction and both equations (3.2) and (3.3) correspond to the condensation process. The hydrolysis reaction can be reflected as an origin for the reactive monomers or oligomers. For a multi-component system, the hydrolysis rate depends on the type of precursor used and thus metal hydroxides are produced at different rates which in turn control the rate of condensation reaction. These monomers further react to form polymers with a higher molecular weight with the three-dimensional continuous network at proper chemical and thermal environment. This process is called gelation. Both powder and film type samples can be prepared by this method. With evaporating the solvent, the wet gel is converted into xerogel and after proper heating dense ceramic material can be formed. If the solvent in the wet gel is removed under a supercritical condition, a highly porous and extremely

low-density material called aerogel is obtained. For thin film synthesis, the substrates are coated with sol after ageing the sol to get gel films. Then the thermal decomposition is performed to remove the residual organic matter and moisture in the gel coating, and finally, the desired metal oxide film is formed through appropriate heat treatment.

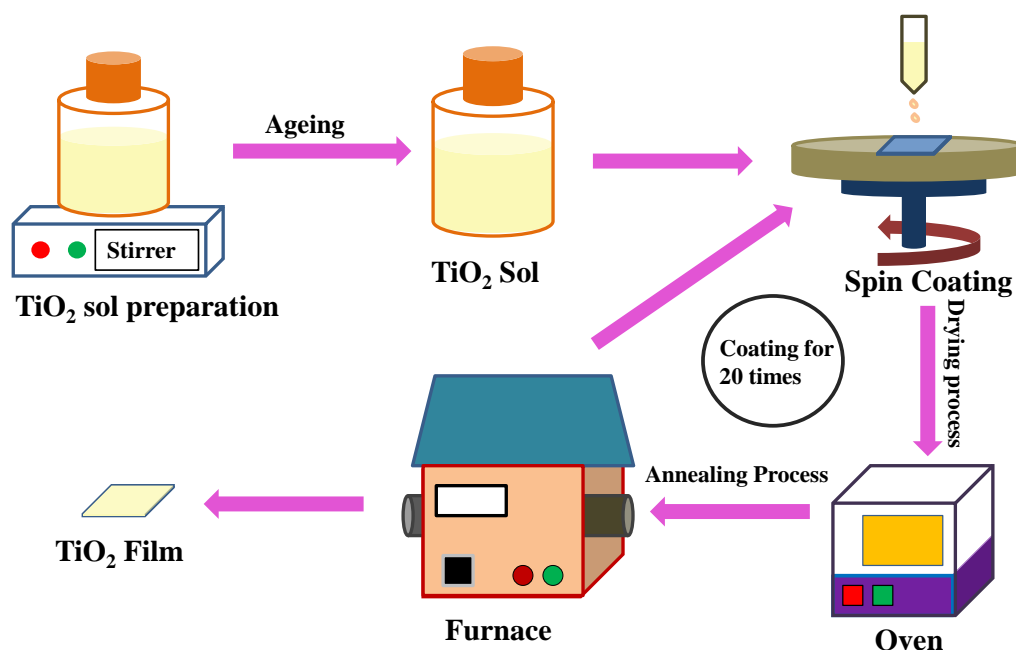


Fig. 3.1: Schematic diagram of TiO₂ thin film preparation by sol-gel method.

There are various coating methods to obtain the sol-gel film; spin coating, drain coating, dip coating, spray coating, capillary coating, etc. Among them, spin coating is the most efficient and broadly used in chemical deposition technique for the preparation of thin films. This process is very much industrial friendly and has a good reproducibility for large area coating. In this process, the cleaned substrate is kept on a holder which can rotate at a certain rotation per minute (RPM) around an axis perpendicular to the substrate surface. The sol is then sprayed on the substrate that spreads evenly throughout the substrate due to a rotation at the required speed for some fixed time. The film thickness depends on the rotation speed, number of coatings, sol concentration etc. Next, the films are dried and annealed at high temperature to obtain crystalline films.

In this thesis work, TiO₂ films have been prepared using sol-gel followed by the spin coating method. Firstly, the soda-lime glass substrates were ultrasonically cleaned using the chromic solution, de-ionized water, HCl, KOH solution, acetone, and methanol sequentially for 10 minutes each. The precursor material used for TiO₂ sol is titanium isopropoxide (Spectrochem, purity > 98%) and 2-methoxy ethanol (Merck, purity > 98%) have been taken as solvent. The milli pore water and acetic acid have been added, followed by a thorough mixing for 2 hours at RT with a magnetic stirrer at a speed of around 400 RPM. After preparation, the solution is aged for 24 hours. Finally, using this sol, twenty (20) coatings have been done at a speed of 2000 RPM for 25 seconds. Each coating was dried at 120 °C and then heated as required. The particular synthesis details of samples have been described in the respective chapters. Fig. 3.1 illustrates the schematic diagram of sol-gel preparation of TiO₂ films. The spin coating unit used for this thesis work is shown in Fig. 3.2.



Fig. 3.2: Digital image of the spin coating unit (APEX Instruments, Model: spinNXG-P1) used in the work.

3.2.2 Physical vapor deposition techniques

Commonly, PVD methods require a high vacuum system to prepare thin films and coatings. In this method, the material goes from a condensed phase to a vapor phase and then back to again in the condensed phase to form thin films. In this thesis work, the thermal evaporation method has been used.

3.2.2.1 Vacuum thermal evaporation

Thermal evaporation under a vacuum is very simple and easy PVD technique to implement. Such a technique allows the deposition of a large range of materials such as metals, semiconductors, composite materials etc. In this process, atoms, clusters of atoms or molecules are removed as vapor flux from a target material placed in a metal crucible having high melting point, such as tungsten. Usually, the target or source material that has to be coated on the substrate is taken as bulk solid or powder form and the crucible loaded with this material is heated to a very high temperature (lower than the melting point of the crucible material but higher than the melting temperature of the target) by passing a current through it in a closed vacuum chamber until the evaporation takes place. The substrates are kept at a distance above the source material and the material vapor finally condenses in form of thin film when it reaches the substrates. Very low pressure ($\sim 10^{-6}$ or 10^{-5} Torr) is maintained to avoid a reaction between the material vapor and the atmosphere inside the chamber. This is a very controlled process where the thickness of the depositing material and the rate of deposition up to nm order per second can be regulated using the thickness monitor attached to this vacuum chamber.

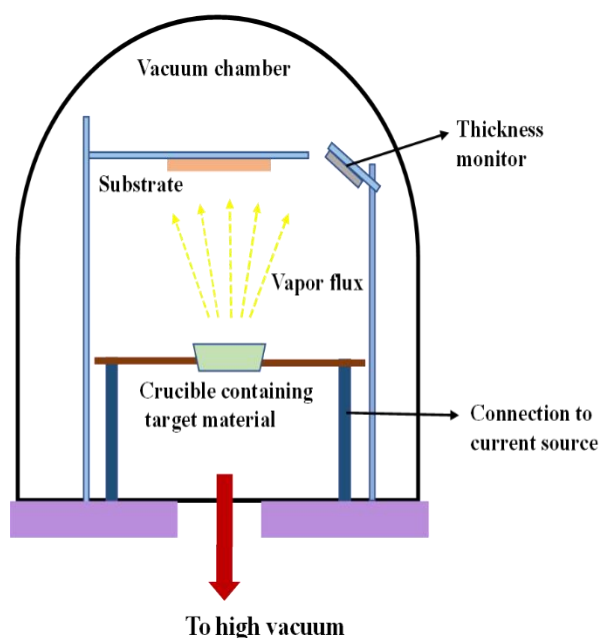


Fig. 3.3: A schematic (left) and digital image (right) of the vacuum thermal evaporator (HINDHIVAC, Model: 12A4D).

In this thesis, this method has been used to deposit a metal layer (Ag) of desired thickness on the TiO_2 film at controlled condition as well as metal contacts (Al) on TiO_2 films

using a shadow mask for photoconductivity measurement of the samples. In Fig. 3.3, the schematic diagram (left) and digital image (right) of the thermal evaporation system used in this work are presented.

3.2.2.2 Post-growth doping: Ion implantation

Ion implantation is a process in which ions of a material are accelerated by an electrical field to impact a solid target and the most common application of ion implantation is as dopants in semiconductors [12, 13]. The ion implantation equipment generally comprises of an ion source (where ions of the desired element can be produced), an accelerator (where the ions are electrostatically accelerated to a high energy), a mass spectrometer, and a chamber with a target (where the ions impinge on a target). Ions are formed from a feed gas, or vapor from a solid source, by running it through a voltage difference, making a plasma. The ions are then accelerated to high energy into the apparatus with an even higher voltage difference. Thereafter, a mass spectrometer is employed at the bend in the setup to separate the incoming ions, only letting the ones with the right velocity, mass, and charge. It is even possible to separate different isotopes of the ion. Finally, the ion beam is focused by the electromagnetic lenses and bombarded on the target mounted on a sample holder.



Fig. 3.4: Digital image of the implantation unit of LEIBF at IUAC, New Delhi.

In this thesis work, the TiO_2 films were implanted with Li ions using the low energy ion beam facility (LEIBF) at Inter-University Accelerator Centre (IUAC), New Delhi. The

experimental details of implantation have been described in the respective chapter. The digital image of the implantation unit installed at LEIBF is shown in Fig. 3.4.

3.3 Thin films characterization techniques

After the fabrication of TiO₂ thin films, they have been characterized by several techniques to investigate their structural, microstructural, elemental, optical, and opto-electronic properties. The characterization techniques those have been used for this thesis work would be discussed in the next section.

3.3.1 Structural and elemental characterization techniques

The structural characterizations and elemental analysis have been done by using X-ray diffractometry (XRD) and X-ray photoelectron spectroscopy (XPS). Therefore, the working principle of XRD and XPS measurement would be discussed here in brief.

3.3.1.1 X-ray Diffraction

XRD is a well-recognized rapid analytical tool used for checking the crystallinity and phase identification of a crystalline material. Also, some other physical properties like crystal structure, lattice parameter, grain size of materials can be determined from this tool. In 1912, Max von Laue had discovered that crystalline materials can act as 3D diffraction grating under X-ray irradiation as the wavelength of X-ray is in the order of the lattice spacing. In the year 1913, Lawrence Bragg and his father, William Henry Bragg had proposed simple but very powerful equation which became known as famous Bragg's law showing the connection between the wavelength of the X-rays, the distance between the planes of the lattice, and the angle at which the X-rays are incident. When a monochromatic X-ray beam of wavelength λ (1.5406 Å for Cu K_α radiation), generated by cathode ray tube, is incident upon a crystal lattice plane having inter planar distance 'd' at a certain angle 'θ', the beam gets scattered and undergoes constructive interference. The condition for interference can be expressed by the well-known Bragg's law as follows [14]:

$$2d\sin(\theta) = n\lambda \quad (3.4)$$

where n is an integer called the order of diffraction. Technically, first, the sample is scanned through a range of 2θ angles, so that all possible diffraction directions of the lattice can be attained. From the Bragg's law, the possible 2θ values are determined by the unit cell

dimensions. However, the intensities of the reflections are determined by the distribution of the electrons in the unit cell. The highest electron density is found around the atoms and intensities depend on the nature and the number of atoms. Planes going through the areas with high electron density reflect strongly and planes with low electron density will give weak intensities corresponding to the highest and lowest intense peak in the XRD pattern. Next, the diffraction peaks are converted to interplanar spacing and the material with its phases is identified. Comparing this data with the joint committee on powder diffraction standard (JCPDS) data file, miller indices of the planes can be identified. Also, from this data file one can easily recognize the crystal structure of the material.

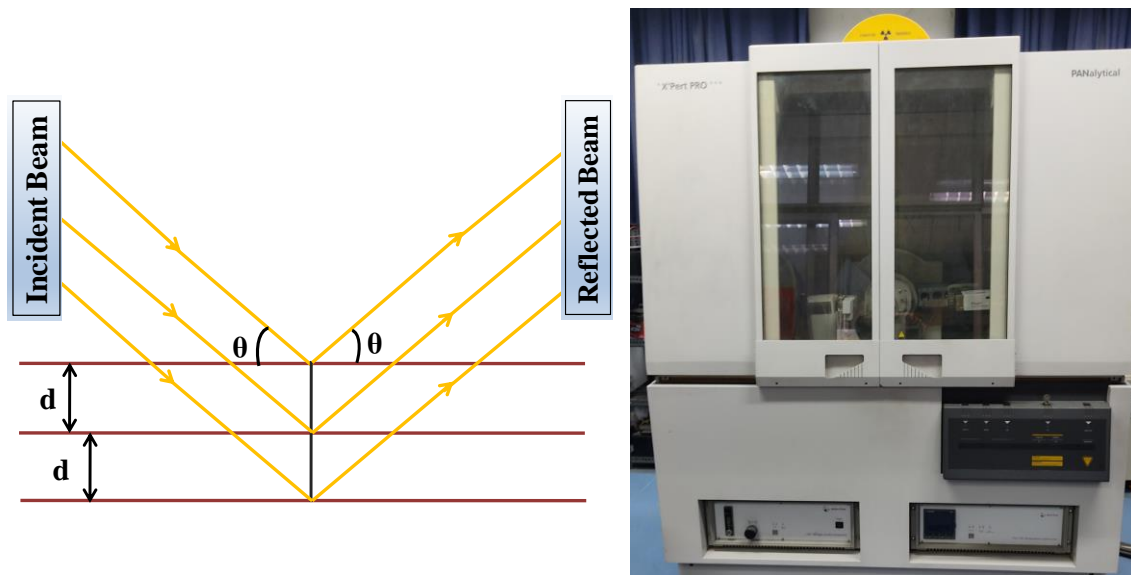


Fig. 3.5: A schematic (left) and digital image (right) of the XRD instrument (Bruker, Model: D8).

Lattice parameters can be estimated by applying the standard equations. For example, in a tetragonal crystal system, lattice parameters 'a' and 'c' can be determined by the equation:

$$\sin^2 \theta = \frac{\lambda^2}{4} \left[\frac{h^2 + k^2}{a^2} + \frac{l^2}{c^2} \right] \quad (3.5)$$

where θ is the corresponding Bragg incidence angle, at which diffraction occurs from the (h k l) plane. Also, one can estimate the crystallite size by using the Scherrer equation given as follows [15]:

$$D = \frac{k\lambda}{\beta \cos\theta} \quad (3.6)$$

where D is the crystallite size by considering the peak broadening due to the film, β is the full-width-at-half-maximum (FWHM) of a selected diffraction peak, and k is the shape factor determined by the geometry of the crystallites. Also, the β values give an idea about the crystalline quality, such as for lower β value the quality of crystallite is better. Fig. 3.5 shows the schematic diagram (left) and digital image (right) of the XRD used for this thesis work.

3.3.1.2 X-ray Photoelectron Spectroscopy

XPS, also known as Electron Spectroscopy for Chemical Analysis (ESCA) is the most widely used surface chemical analysis technique to detect the elemental composition of materials along with their electronic states. Each atom in a material has core electrons having characteristic binding energy (E_b) ideally equal to the ionization energy of that electron and this tool simply deals with the basic photoelectric effect. This technique is surface sensitive and it can provide information only about the top surface 80-100 Å of the sample surface as the electrons below this layer can't emit outside of the surface due to the collision with the electrons and atoms lying above them. When a monoenergetic X-ray with photon energy higher than E_b , is incident on a sample, the core electron emits from the atom as well as the surface with some kinetic energy, E_k . The kinetic energy of the photoelectron can be calculated by using the famous photoelectric equation [16]:

$$E_k = h\nu - E_b - \phi \quad (3.7)$$

Where $h\nu$ is the incident photon energy, ϕ is the work function that is adjustable of the material.

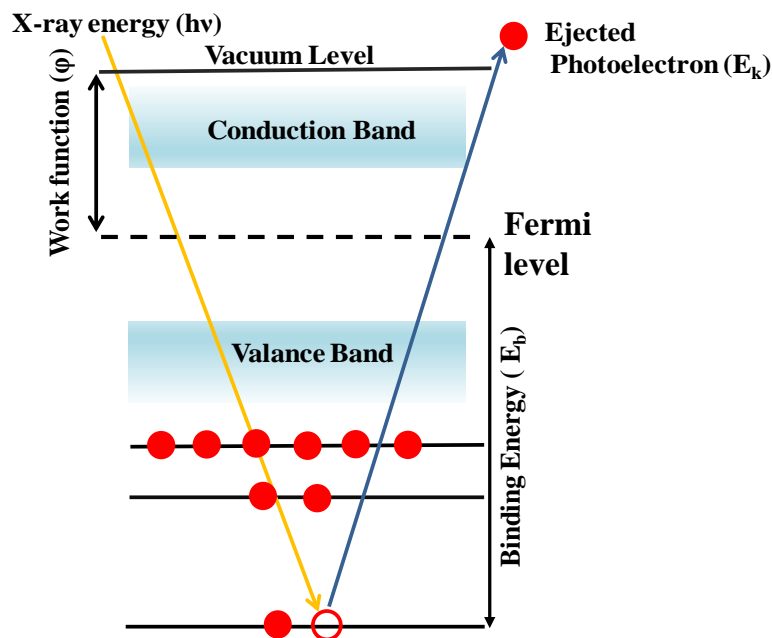


Fig. 3.6: A schematic of the working principle of XPS.

XPS patterns are obtained by irradiating a material with X-ray beam while simultaneously measuring the kinetic energy and the number of photo excited electrons that escape from the surface. Since the energy of core electron is a significant characteristic of a material, a detailed elemental analysis can be performed by this technique. The binding energy of the photoelectrons is measured by an electron energy analyzer. In XPS, a high to ultrahigh vacuum (10^{-8} - 10^{-9} mbar) is required to maintain the accuracy of detection of the actual elements without contamination. The elemental identity, chemical bonding, and quantitative amounts of constituent elements can be determined from the position, shape, area, and intensity of the photoelectron peak. Fig. 3.6 and 3.7 show the schematic diagram of the working principle and the digital image of the XPS instrument used for this thesis work.

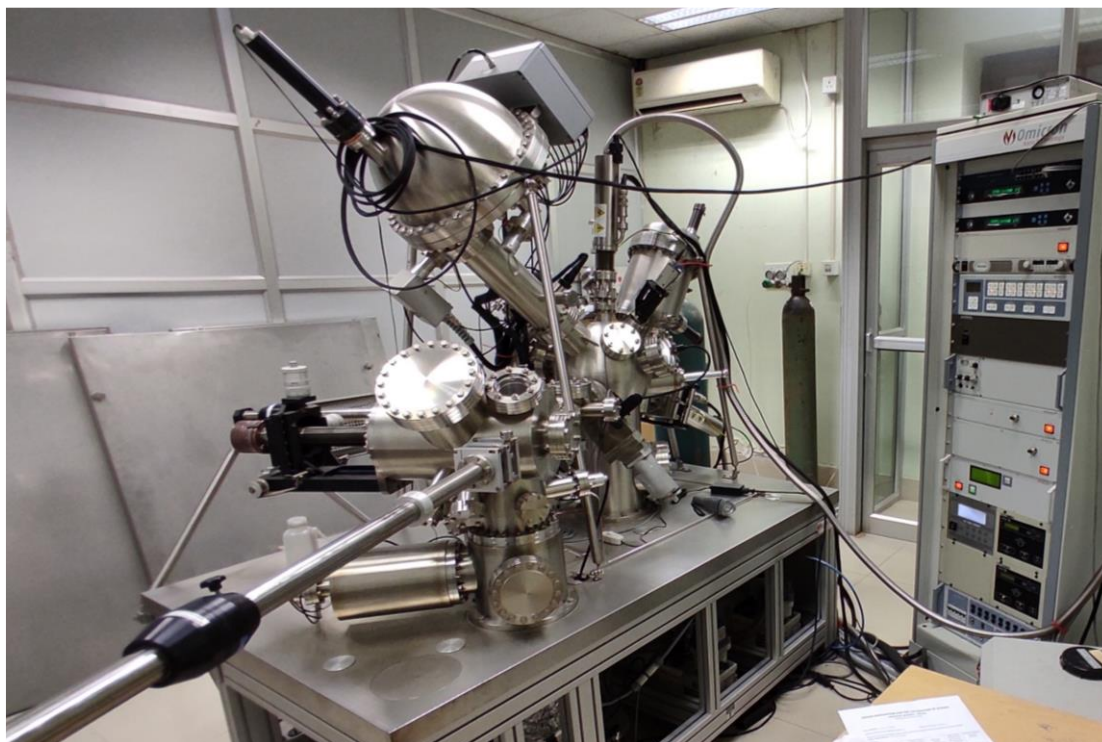


Fig. 3.7: Digital image of the XPS instrument (Omicron, Serial No.: 0571).

3.3.2 Microstructural and morphological characterization techniques

The shape, size, orientation of the grains, surface roughness, porosity, and microstructural defects in the films are known as the microstructure and morphology of the thin film. These results are quite helpful to explain the electrical, optical, and optoelectronic properties. Field emission scanning electron microscopy (FESEM) and atomic force microscopy (AFM) has been used in this work for the microstructural and morphological analysis. Hence these two techniques are discussed in the next section.

3.3.2.1 Field Emission Scanning Electron Microscopy

Scanning electron microscope (SEM) is a type of electron microscope that produces images of a sample by scanning it with a highly accelerated (having energy of several KeV) focused electron beam which is produced by the heating of a metal filament known as electron gun. The SEM with field-emission cathode in the electron gun is known as a FESEM which provides narrower probing beams for both low and high electron energy. As a result, the spatial resolution of the images is improved a lot with the highest possible magnification. The use of a field-emission cathode can also reduce the possibility of sample charging which sometimes

may damage the sample. The working principle of FESEM is similar to an electron microscope where the electron beam is used instead of light. As the wavelength of accelerated electrons is shorter

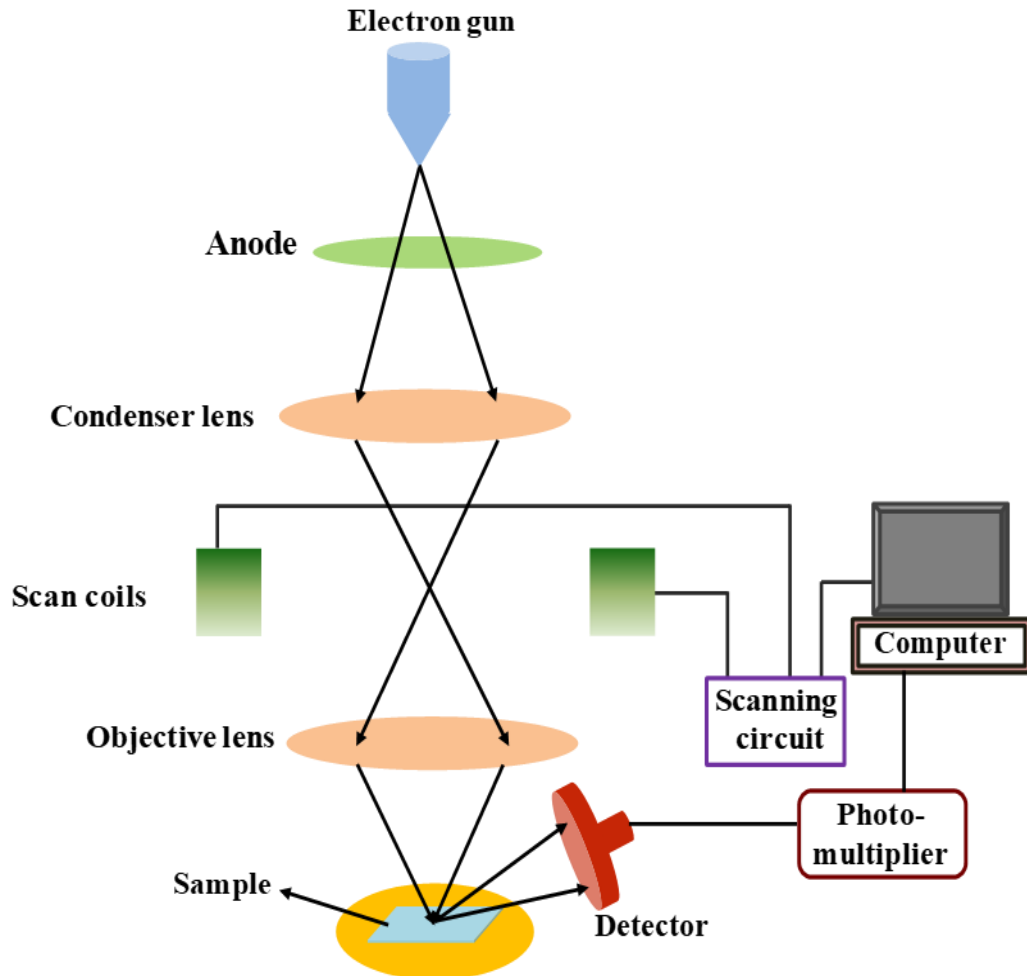


Fig. 3.8: A schematic of the working principle of FESEM.

than that of electromagnetic wave, hence the electron beam in FESEM can produce a better resolution image than the optical microscope. Here, the electron beam passes through several condenser lenses placed vertically which helps to focus the beam onto the target sample. Usually, the target is scanned in a raster scan pattern having energy ranging between 0.2 to 40 KeV. Various electrons such as back-scattered electrons, secondary electrons, auger electrons, characteristics X-ray etc. are produced due to the interactions in between the target sample and the electron beam striking on it. The back-scattered electrons are used for contrasting the multiphase compositions of sample whereas the secondary electrons are generally for

collecting information regarding surface morphology and topology of the sample to build the microstructural image of the target sample. The characteristic X-ray photons, produced when the beam hits the target, are collected by the detector, and analyzed to recognize the elements present on the surface of the target.



Fig. 3.9: Digital image of FESEM (JEOL, Model: JSM-6700F).

Sometimes an additional arrangement is attached to the FESEM for elemental analysis of the target sample called energy dispersive X-ray spectroscopy (EDS/ EDX). This technique works on the generation of the X-ray fluorescence produced from the atoms when scanning beam falls on them. Then, the characteristic X-ray photon produced from the elements in sample are collected by the detector and analyzed to recognize the elements present in target sample. In this thesis work, FESEM has been used for topography imaging as well as cross-section analysis. Fig. 3.8 and 3.9 show the schematic diagram of and the digital image of the FESEM instrument used for this thesis work.

3.3.2.2 Atomic Force Microscopy

AFM is one kind of high-resolution scanning probe microscopy (SPM) having resolution in the order of a fraction of one nm, more than 1000 times better than the optical diffraction limit. It measures mainly the asperity of a sample using a tip with micro-machined cantilever attached with the instrument. As the tip scans the sample surface, the inter-atomic force between the tip and the sample surface induces a displacement of the tip that bends the cantilever which is measured using a laser beam. The moving cantilever reflects the laser beam which strikes a position-sensitive four segment photodiode. The difference between the segments of photodiode indicates the position of the laser spot and helps to provide a three-dimensional pattern of the motion using a piezoelectric scanner. Then the data is processed in the computer and comes up with a topographical image of the surface with atomic range resolution.

There are three types of modes in AFM to read the sample: contact mode, tapping mode and non-contact mode. Firstly in ‘contact mode’, the tip can be dragged smoothly over the surface and in the second one, ‘tapping mode’, the tip is repeatedly tapped on the surface. In ‘non-contact mode’ where the tip doesn’t actually touch the material surface but rather measures attractive forces between the sample and tip. The tapping mode is normally used for AFM imaging. The contact mode is used for some specific applications, such as force curve measurements.

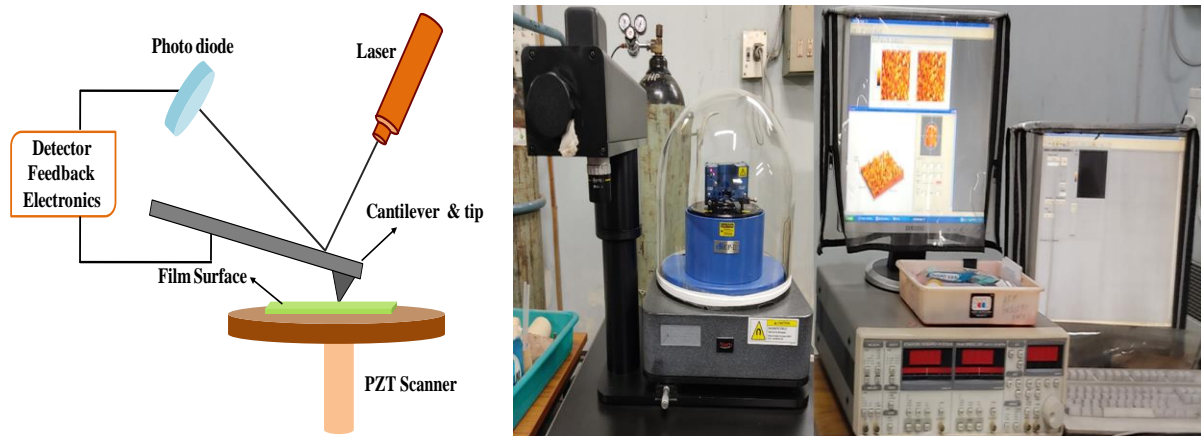


Fig. 3.10: A schematic (left) and digital image (right) of the AFM instrument (VECCO, Model: diCP-II).

The properties and dimensions of the cantilever and tip play important role in determining the sensitivity and resolution of the AFM. AFM tips are manufactured using micro-lithographic techniques normally shaped like a pyramid and it is gold coated on the upper side with spring constants ~ 10 pN/nm. The sharper the tip, the better is the resolution of the final image of the sample surface. The tip is generally made from ceramic, semiconducting materials, and carbon nanotubes. AFM is basically an updated version of electron microscopes with two main advantages; it doesn't require a vacuum and can give three-dimensional images. As vacuum is not needed, hence there is the versatility to measure samples in air or any required medium (even underwater). Also, it can give additional information like roughness, co-efficient of friction of the sample. In this thesis, AFM images of the TiO₂ films are studied to know the surface morphology and topographic nature. Fig. 3.10 shows the schematic diagram (left) and digital image (right) of the AFM instrument used for this thesis work.

3.3.3 Optical characterization techniques

The optical characterization of the material is very important as it has huge applications in various optoelectronic devices, such as solar cells, photosensors, light emitting diodes (LEDs), etc. There are mainly three types of optical characterization used in this work namely transmission, absorption spectroscopy, and photoluminescence (PL). For more investigations about the PL relaxation pathways, Time Correlated Single Photon Counting (TCSPC) measurement has been carried out.

3.3.3.1 UV-VIS transmission and absorption spectroscopy

It is a very convenient tool to measure the absorbance, transmittance, and reflectance of a material. When a beam of light falls on a sample, a part of the beam is reflected, another part is absorbed and the rest of the incident light transmits through the sample. Light passing through an optical medium gets attenuated due to both absorption and reflection. As light travel more through a medium, more it gets absorbed. Mathematically, absorbance is the logarithmic ratio of the incident radiation to the transmitted radiation through the medium. According to Lambert-Bouguer Law, the absorbance of an optical medium is directly proportional to the density of the absorbing medium and path length i.e., the thickness of a material. For a medium with insignificant scattering, at a particular wavelength, the absorbed beam intensity, ' I ' is related to incident beam intensity, ' I_0 ' according to Lambert-Bouguer law [17]:

$$I(\lambda) = I_0(\lambda) e^{-\alpha(\lambda)d} \quad (3.8)$$

where ‘ d ’ is the sample thickness and ‘ α ’ is the absorption coefficient. The change in the α with λ is called the absorption spectrum of the medium. According to classical electromagnetic theory, the absorption coefficient can be written as the following equation:

$$\alpha = 4\pi k/c \quad (3.9)$$

where k is the imaginary part of the complex index of refraction and it is also called extinction coefficient and c is the speed of the light in free space. Now considering that the reflection is

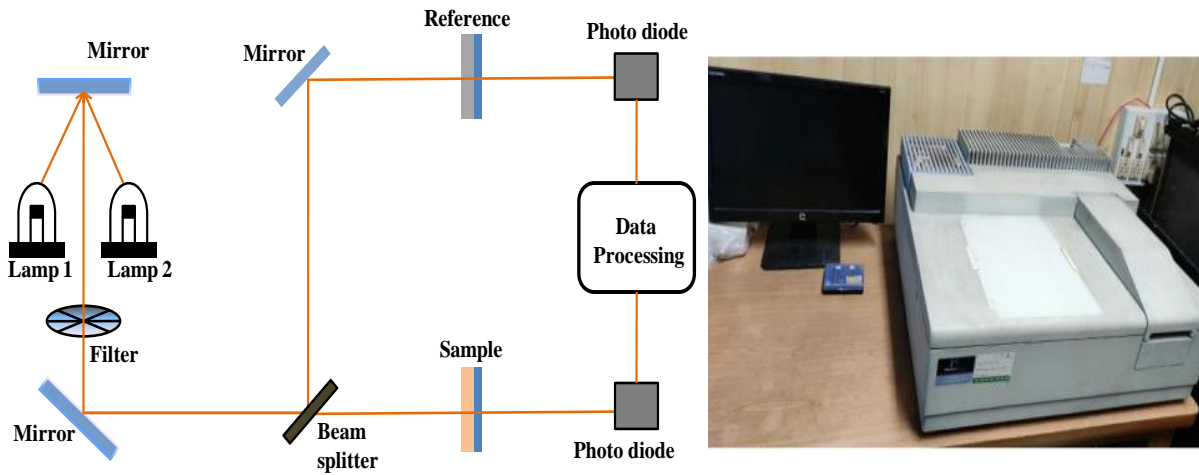


Fig. 3.11: A schematic (left) and digital image (right) of the UV-VIS spectrometer (PerkinElmer, Model: Lamda 35).

insignificant for any material, then the transmittance of a sample is equal to the ratio of the transmitted beam to that of the incident beam and its expression is given by:

$$T(\lambda) = \frac{I(\lambda)}{I_0(\lambda)} \quad (3.10)$$

Using above two equations,

$$\ln\{T(\lambda)\} = -\alpha(\lambda)d \quad (3.11)$$

Therefore if ‘ d ’ is known, the absorption coefficient can be calculated from the above equation. From this relation, Tauc plot $[(\alpha h\nu)^{1/n} \text{ vs } h\nu]$ can be drawn to determine the optical band-gap of the materials where $n = 1/2$ for direct band-gap and $n = 2$ for indirect band-gap materials [18]. A schematic of and the digital image of the UV-VIS spectroscopy instrument used in this thesis work are shown in Fig. 3.11.

3.3.3.2 Photoluminescence measurement

When light of suitable energy is incident on a material, the photon gets absorbed by the material and the absorbed energy is converted into several forms. It can be transformed into thermal energy through inter-atomic collisions and later radiated at lower wavelengths. When it is the subsequent emission of a photon, it is classified as PL. Luminescent materials can radiate light even when the excitation is turned off. The time gap between the absorption and emission of a photon is called life-time or decay time of emission. Depending on life-time, luminescence is

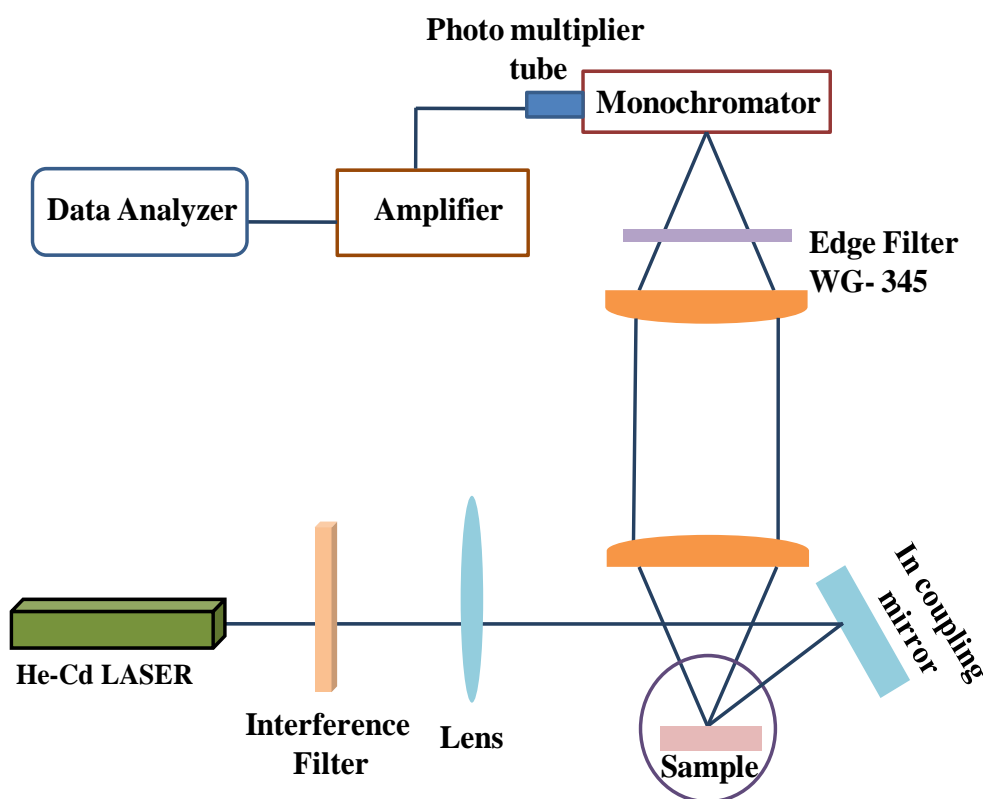


Fig. 3.12: A schematic of the PL instrument.

named as phosphorescence (long life time $\sim 10^{-3}$ s and more) and fluorescence (short life time $\sim 10^{-9}$ to 10^{-5} s). These processes involve electronic transitions between the different energy states associated with the CB and VB and the other in-gap defect states lying in between. The general discussions about PL property have been already presented in previous chapters. The required major components of a PL apparatus are: (i) an illuminating source to excite the sample, (ii) a monochromator, (iii) a dark chamber where the sample is placed, and (iv) a detector that recognizes the emission intensity.

In this thesis work, the sample has been irradiated by He-Cd LASER (Kimmon Koha Co., Ltd., Model: KR1801C) source at 325 nm excitation. The emission from the sample has been focused through an array of lenses and mirrors (Horiba Jobin Yvon, Model: iHR 320) together with a photomultiplier tube and finally recorded by a detector. The schematic and the digital image of the PL set-up used in this work is shown in Fig. 3.12 and 3.13 respectively.



Fig. 3.13: Digital image of the PL measurement set-up.

3.3.3.3 Time Correlated Single Photon Counting

TCSPC is a well-established and common technique to measure PL decays in the time domain. This instrument provides time dependent intensity profile of the emitted photons upon excitation by a short flash of light [19]. In principle, a single photon is detected and its time of arrival with respect to a reference signal usually the light source is measured. Mainly, the laser is used as a source to excite the sample. Because of the high repetition rate of the laser, this process can be repeated many times to accumulate a sufficient number of photon events to build up a statistical photon distribution over the time and spatial coordinates. In practice, a sample is excited by a pulsed laser source. The pulse duration is in the range of femtoseconds to about 100 picoseconds with a pulse repetition rate between 1-100 MHz. A single photon

detector is attached to record the emission. A fast and efficient TCSPC electronics is needed to register the photon events in relation to the laser sync pulses. From the PL decay curve, the lifetime can be determined. When TCSPC instrument is attached with a scanning technique fluorescence lifetime imaging (FLIM) can also be performed.

In this thesis work, PL emission life time measurement has been carried out by TCSPC instrument (Horiba Jobin Yvon IBH) using micro-channel plate photomultiplier tubes (Hamamatsu, Model: R3809) by exciting the samples with 295 nm light using a picosecond diode (IBH, Model: Nanoled-295) at the detection wavelength of 380 nm. The digital image of the TCSPC instrument used in this work is shown in Fig. 3.14.



Fig. 3.14: Digital image of the TCSPC instrument.

3.3.3.4 Raman spectroscopy

Raman spectroscopy is an important tool in the field of vibrational spectroscopy [20]. This means that it analyses a sample chemically by using light to create molecular vibration, and interpreting the interaction of light with the chemical bonds of the substance. These yields detailed information about molecular composition, structure, polymorphism, defects in crystal, crystallinity, and molecular dynamics. The working principle of Raman spectroscopy is based on the inelastic scattering of light when it falls on a sample. A very small part of scattered lights changes its wavelength after the interaction of light with the sample. This usually happens in relation to molecular vibration. This scattered light is then collected and is used to gather information about the sample. This scattering phenomenon, which was predicted by Adolf Smekal in 1923 and discovered by C.V. Raman in 1928, is called the Raman effect [21].

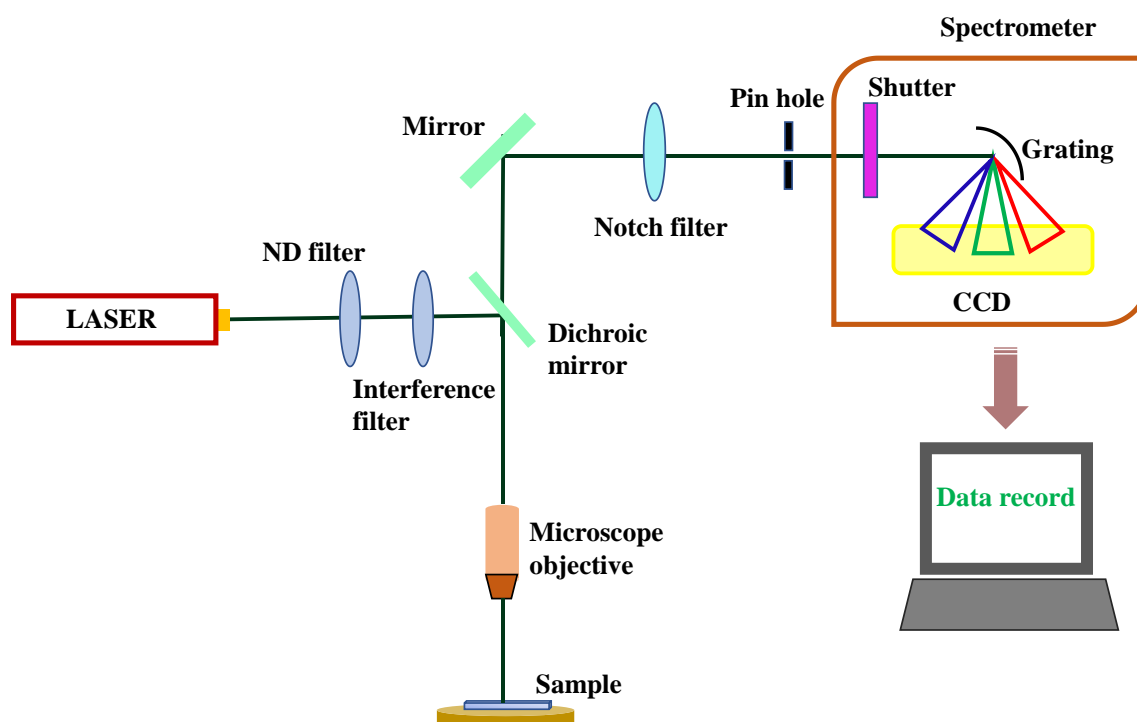


Fig. 3.15: A schematic of Raman spectroscopy.

As the change of wavelength is very small compared to the wavelength of the irradiating light, the change of wavelength is most easily observed when monochromatic light is used. Therefore, in a Raman spectrometer, a laser beam is most suitable to focus on the sample under investigation. However, that sample must not be showing fluorescence to the laser used for excitation. If that is the case, the fluorescence will cover most of the Raman effect, since it is so weak in comparison. After the laser light has irradiated the sample, the scattered light is passed through a notch filter (to get rid of any light from the excitation laser). Then it is directed to a grating element, which distributes the inelastic parts like a prism and according to wavelength. In the end, these rays are directed to a CCD detector which then outputs a spectrum depending on the intensity. In this thesis work, Raman measurements were carried out using a Lab RAM HR800 spectrometer (Horiba Jobin Yvon) with a 458 nm Argon-ion laser as the excitation source. The schematic and the digital image of the Raman instrument used in this work is shown in Fig. 3.15 and Fig. 3.16 respectively.

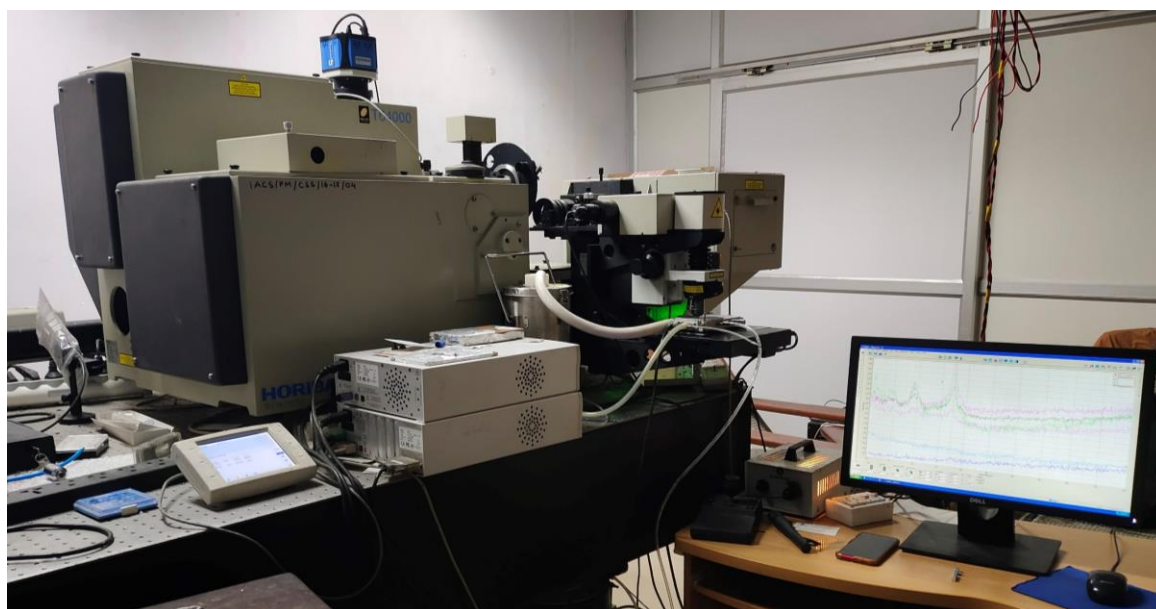


Fig. 3.16: Digital image of the Raman instrument.

3.3.4 Optoelectronic characterization techniques

Optoelectronics is the study and application of those electronic devices which either detect or source or control light. Optoelectronic property is the combined effect of the optical and electrical phenomenon based on the quantum mechanical effects of light on the

semiconducting materials, sometimes in the presence of an electric field. In this work, the photodetection properties of the samples have been observed thoroughly.

3.3.4.1 Photoconductivity measurements

Photodetectors are sensors of light or other electromagnetic radiation. As discussed in chapter 1, there is a wide variety of photodetectors that may be classified by the mechanism of detection. Among them, in this thesis work, photodetection in simple photoconductive mode has been used. Photoconductivity is nothing but enhancement of electrical conductivity of material upon incidence of electromagnetic radiation such as visible, UV, and IR light of sufficient energy. The general discussions on photoconductivity property have been described in earlier chapters.

In a typical photoconductivity measurement, under the irradiation of suitable light, the electron-hole pairs are continuously created and recombined simultaneously. The enhancement of photocurrent occurred due to an excess number of charge carrier generation in the process. The defects states of the materials serve as recombination center (trap) for electro-hole pairs which highly affects photoconductivity. The main factors that control this process are: photocarrier generation, trapping effect, and time constants.

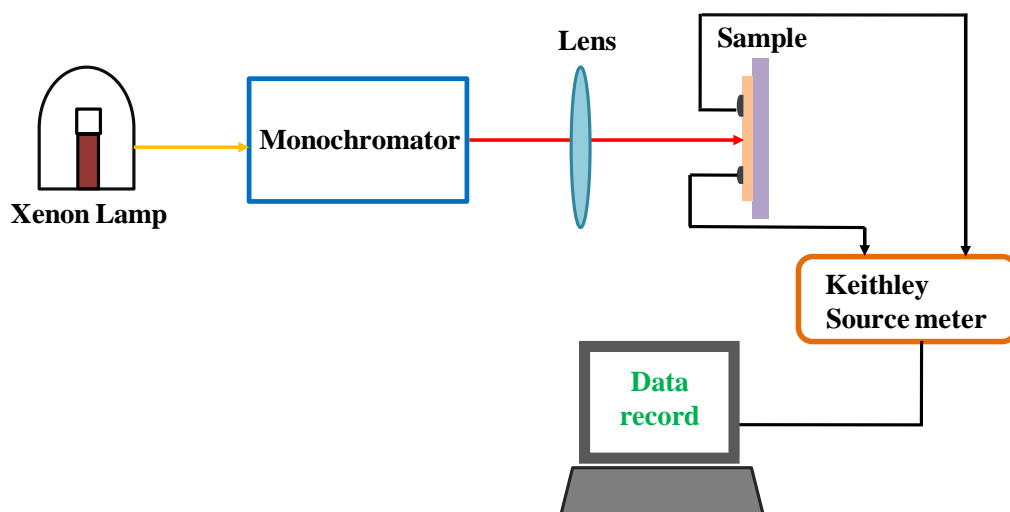


Fig. 3.17: A schematic of the photoconductivity measurement set-up.

From semiconductor physics, at any instant (t), the number of photocarriers in an ideal semiconductor is given by

$$n(t) = n(s)(1 - e^{-t/\tau}) \quad (3.12)$$

where $n(t)$ is the photo generated carrier concentration at t, $n(s)$ is the saturated photocarrier concentration and τ is the life time of a carrier.

Assuming no trap states or recombination center except the band edge recombination, the rate equation of for transient photocurrent can be expressed as

$$\frac{dn(t)}{dt} = G - \frac{n(t)}{\tau} \quad (3.13)$$

Where G is the rate of generation of carriers upon illumination

When the light is turned off, current value begins to fall due to recombination of carriers. Then the rate of decay equation takes form,

$$\frac{dn(t)}{dt} = - \frac{n(t)}{\tau} \quad (3.14)$$

At any instant t during decay, the carrier concentration can be written as

$$n(t) = n(s) e^{-t/\tau} \quad (3.15)$$

So, at $t = \tau$,

$$n(t) = n(s)(1 - 1/e) \quad [\text{during growth}] \quad (3.16)$$

$$n(t) = \frac{n(s)}{e} \quad [\text{during decay}] \quad (3.17)$$

From these equations the free carrier life time can be calculated easily.

In general, chemically, or physically developed metal oxide semiconductor thin films contain various defect states and their effects cannot be ignored. Therefore, in presence of defect states, the rate equation can be written as;

$$\frac{dn_e}{dt} = G - \alpha_1 (N_t - n_c) + c_1 n_e \quad (3.18)$$

$$\frac{dn_c}{dt} = \alpha_1 (N_t - n_c) - \delta_o p_e n_c - r_1 n_c \quad (3.19)$$

$$\frac{dn_p}{dt} = G - \delta_0 p_e n_c - p_e C_2 \quad (3.20)$$

where n_e & p_e are excess electrons & holes in CB and VB; c_1 & c_2 are capturing cross sections in recombination centers; n_c & N_t are occupied and the total number of traps; α_1 & δ_0 are electron & hole capturing rate respectively.

Photoconductivity set-up simply contains a light source and an electrometer for current and voltage measurements. Sometimes a monochromator is attached for specific light detection. In this thesis work, a Xe light source with a monochromator (Newport Corp-USA, Model: 66902) and a source meter (Keithley, Model: 2410 with GPIB card) have been used. Electrodes or metal contacts (deposited by the thermal evaporator) have been deposited on the films for measurement purposes. Also, for low current (in the order of nA or lower) measurements, picoammeter (Keithley, Model: 6485) has been connected in series with the source meter. Further, the intensity of incident illumination has been modulated using a neutral density filter and detected by a power meter (Newport, Model: 1930C). The schematic diagram for photoconductivity measurement and digital images of the power meter and photoconductivity measurement set-up used in this thesis work are shown in Fig. 3.17 and Fig. 3.18 respectively.



Fig. 3.18: Digital image of the photoconductivity measurement set-up.

3.4 References

- [1] P. Nyamukamba, O. Okoh, H. Mungondori, R. Taziwa, S. Zinya, Titan. Dioxide-Mater. a Sustain. Environ, 2018
- [2] B. Pant, M. Park, S.-J. Park, Coatings, **9(10)**, (2019), 613
- [3] R.L. Milot, G.E. Eperon, H.J. Snaith, M.B. Johnston, L.M. Herz, Advanced Functional Materials, **25(39)**, (2015), 6218-6227
- [4] D. Buso, M. Post, C. Cantalini, P. Mulvaney, A. Martucci, **18(23)**, (2008), 3843-3849
- [5] C. Chen, Y. Cheng, Q. Dai, H. Song, **5(1)**, (2015), 1-12
- [6] S. Šegota, L. Ćurković, D. Ljubas, V. Svetličić, I.F. Houra, N. Tomašić, Ceramics International, **37(4)**, (2011), 1153-1160
- [7] H. Miao, X. Hu, J. Fan, C. Li, Q. Sun, Y. Hao, G. Zhang, J. Bai, X. Hou, Applied Surface Science, **358**, (2015), 418-424
- [8] S. Murugesan, P. Kuppusami, N. Parvathavarthini, E. Mohandas, **201(18)**, (2007), 7713-7719
- [9] W.-J. Lee, M.-H. Hon, **114(15)**, (2010), 6917-6921
- [10] J. Feng, J. Han, X. Zhao, Progress in Organic Coatings, **64(2-3)**, (2009), 268-273
- [11] a.H. Schmidt, **100(1-3)**, (1988), 51-64
- [12] J.F. Gibbons, Ion implantation in semiconductors—Part I: Range distribution theory and experiments, Proceedings of the IEEE, **56(3)**, (1968), 295-319
- [13] B. Sealy, Ion implantation doping of semiconductors, International materials reviews, **33(1)**, (1988), 38-52
- [14] W.H. Bragg, W.L. Bragg, The reflection of X-rays by crystals. Proceedings of the Royal Society of London. Series A, Containing Papers of a Mathematical and Physical Character, **88(605)**, (1913), 428-438
- [15] A. Taylor, H. Sinclair, On the determination of lattice parameters by the Debye-Scherrer method, Proceedings of the Physical Society (1926-1948), **57(2)**, (1945), 126
- [16] D. Wong, P. Lee, G. Shenghan, W. Xuezhou, H.Y. Qi, F.S. Kit, European Journal of Physics, **32(4)**, (2011), 1059
- [17] N.A. Mortensen, S. Xiao, Applied Physics Letters, **90(14)**, (2007), 141108
- [18] N. Mott, Conduction in non-crystalline systems: IV. Anderson localization in a disordered lattice, Philosophical Magazine, **22(175)**, (1970), 7-29
- [19] L.M. Hirvonen, K. Suhling, Wide-field TCSPC: methods and applications, Measurement Science and Technology, **28(1)**, (2016), 012003
- [20] R.J.A.i.P. Loudon, The Raman effect in crystals, **13(52)**, (1964), 423-482
- [21] R. Singh, Physics in Perspective, **4(4)**, (2002), 399-420

CHAPTER-4

Investigation on photoluminescence properties of TiO₂ thin films via various post-growth treatments

Contents of this chapter has been published in *Journal of Luminescence*, 179, 480–486, (2016).

4.1 Introduction

Various works regarding the PL properties of different morphologies of TiO₂ have been studied till date. However, it is worthy to note that the interpretation of experimental PL results of TiO₂, similar to ZnO is still controversial. It is well understood from the previous chapter that the PL properties of TiO₂ thin films are strongly dependent on the intrinsic as well as surface adsorbed defects [1, 2]. Therefore, a controlled processing is necessary to regulate these defects in order to enhance the emission property [3, 4]. Post-growth treatments can be a simple and useful way to tune the defects in TiO₂ films. Keeping these concerns in mind, in this chapter, a detailed investigation on the RT PL properties of sol-gel derived TiO₂ thin films under various post-growth treatments has been presented. It has been shown that rapidly cooled films after air annealing exhibit higher UV PL where the vacuum annealing and UV curing in TiO₂ films leads to higher visible PL due to defect modifications.

4.2 Experimental details

TiO₂ thin films have been deposited on ultrasonically cleaned soda-lime glass substrates synthesized via sol-gel technique followed by spin coating. Details of sol preparation and coating have been mentioned in previous chapter. Each coating has been dried at 120 °C for 10 minutes and then heated at 500 °C for 20 minutes. This process has been repeated for 19 times. After 20th coating, three sets of samples have been prepared by varying the final treatment as described below:

- (i) Thermal annealing at 500 °C in air ambient for 2 hours followed by very rapid cooling (sample A)
- (ii) Thermal annealing at 500 °C in vacuum ambient (1.2×10^{-6} Torr) for 2 hours followed by a slow cooling (sample B)
- (iii) UV (365nm) curing in air ambient using an irradiance of 1.2 mW power from a UV source (Spectroline, ENF-280C/FE) for 2 hours at RT (sample C)

The flow chart for film preparation and post-growth annealing procedures is shown in Fig. 4.1

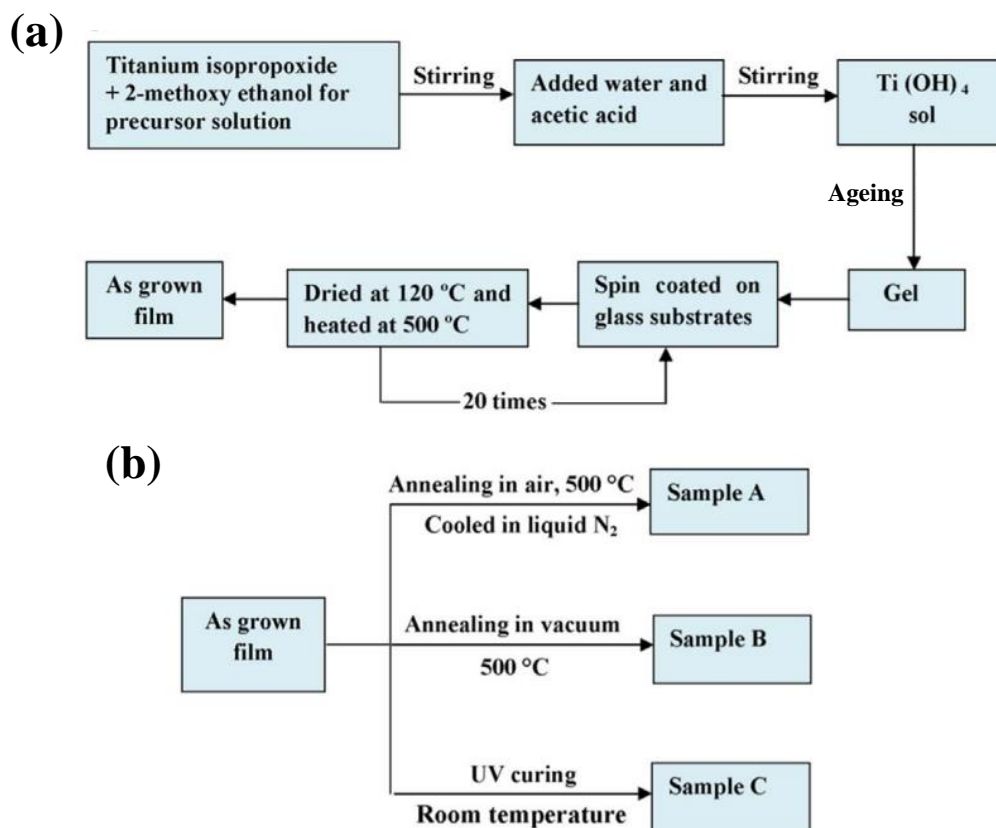


Fig. 4.1: Flow chart of the (a) sol-gel preparation of TiO₂ films and (b) various post-growth treatments of TiO₂ films.

The structural properties of the thin films have been investigated by using the XRD while the chemical states of the elements and contribution of the surface adsorbed -OH groups, oxygen molecules in the films have been confirmed and discussed from XPS. The transmittances of the films have been measured by using a UV-VIS spectrometer. The RT PL spectra have been measured by using a spectrophotometer where the films have been excited by a He-Cd LASER. For dark current measurement, two Al (~ 40 nm thick) electrodes have been deposited by the vacuum thermal evaporator. The details of instruments used in this work have been illustrated in chapter 3.

4.3 Results and discussions

The XRD patterns of the films as presented in the Fig. 4.2 depicts the multiple peaks at $2\theta = 25.3^\circ$, 37.8° , 48.0° , and 53.9° which are indexed to the (101), (004), (200), (105) diffraction planes of anatase TiO_2 phase (JCPDS file: PDF#211272). The presence of a very weak peak $2\theta = 30.9^\circ$ has been assigned to (121) peak of brookite according to the JCPDS data file (PDF#291360). However, the XRD results of all the films indicate that mainly anatase phase of TiO_2 film has been formed. This result is in excellent agreement with the study reported by Paola et al. [5] that anatase TiO_2 is formed $\sim 500^\circ\text{C}$ and brookite is a meta-stable phase of TiO_2 often produced as a by-product with rutile and anatase.

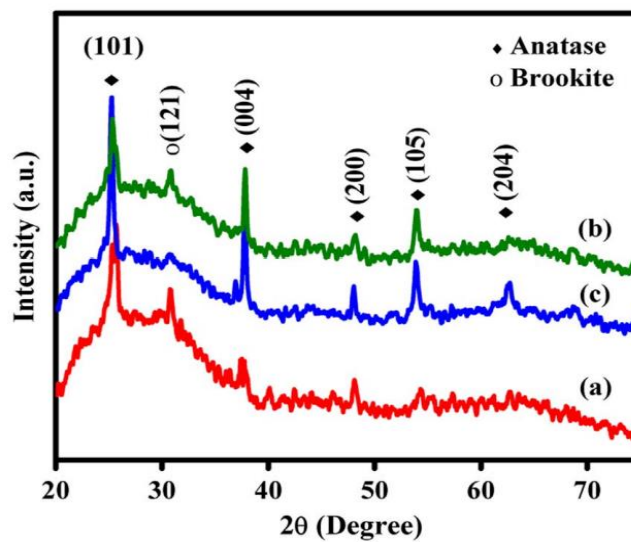


Fig. 4.2: XRD patterns of (a) Sample A, (b) Sample B, and (c) Sample C

Fig. 4.3 shows the transmission spectra for all the samples as well as for the bare glass substrate. All films exhibit an average transparency greater than 70% in the region of 500-700 nm of the spectra and below 400 nm the transmittance value sharply drops for all the films due to band edge transition. Several fringes have been observed for all films which indicates appreciable thickness of the films. The thickness of the films has been calculated theoretically by the famous Swanepoel envelope method [6] using the following calculations:

$$n = [N + (N^2 - s^2)^{1/2}]^{1/2} \quad (4.1)$$

$$N = 2s \frac{T_M - T_m}{T_M T_m} + \frac{s^2 + 1}{2} \quad (4.2)$$

Where T_M and T_m is the transmission maximum and corresponding minimum at a certain wavelength λ . The refractive index of the substrate at each λ is calculated by the formula:

$$s = \frac{1}{T_s} + \left(\frac{1}{r_s^2} - 1\right)^{\frac{1}{2}} \quad (4.3)$$

Where T_s is the transmittance of the substrate. The variation of the refractive indices with λ has been shown in the inset of the Fig. 4.3.

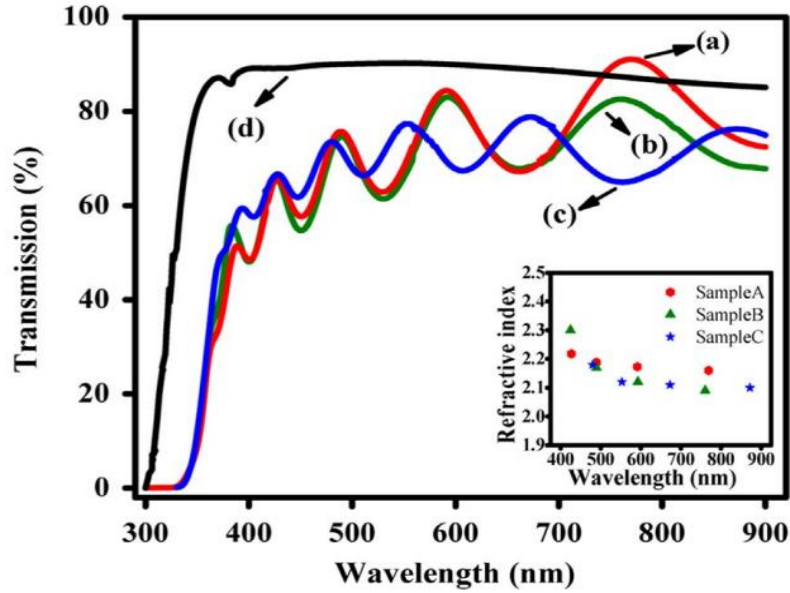


Fig. 4.3: Transmission spectra of the (a) Sample A, (b) Sample B, (c) Sample C, and (d) bare substrate. The inset shows the variation of refractive indices with wavelength for all samples.

Then the thickness of the films is estimated with the calculated n values by using the equation:

$$d = \frac{\lambda_1 \lambda_2}{2 (\lambda_1 n_1 - \lambda_2 n_2)} \quad (4.4)$$

where n_1 and n_2 are the refractive indices of the successive maxima or minima at λ_1 and λ_2 . The average thicknesses estimated of the samples A, B, and C are 616, 590, and 645 nm respectively.

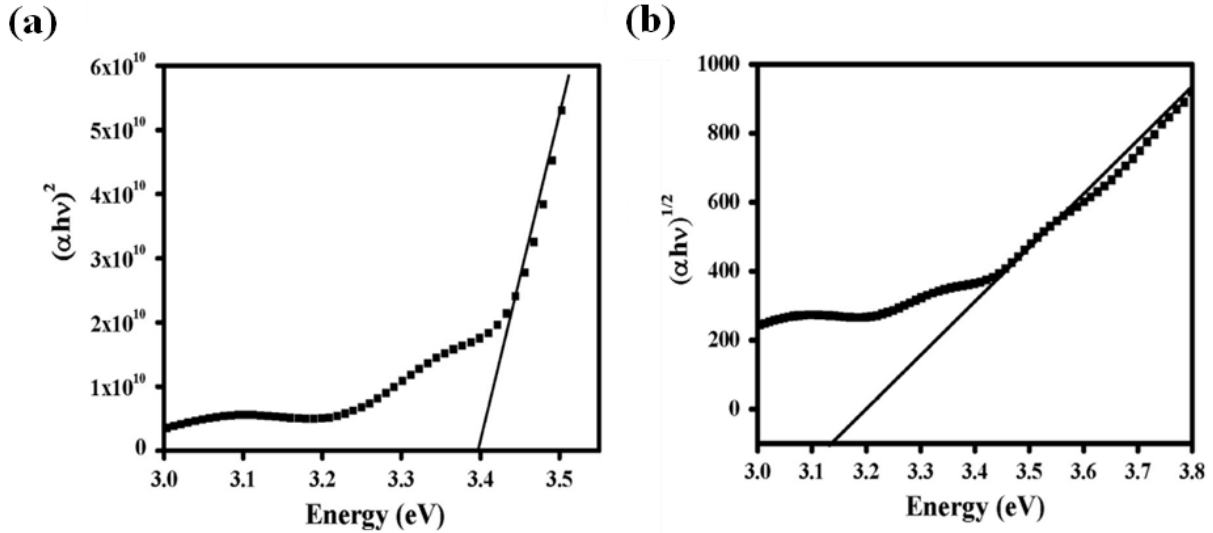


Fig. 4.4: Representative (a) $(\alpha h\nu)^2$ vs $h\nu$ and (b) $(\alpha h\nu)^{1/2}$ vs $h\nu$ plots of Sample A.

The optical band-gaps of the samples are calculated by using very well-known Tauc plot based on fundamental absorption equation:

$$(\alpha h\nu)^{1/n} = A (h\nu - E_g) \quad (4.5)$$

where α is absorption coefficient, $h\nu$ is the incident photon energy, E_g is the band-gap of TiO_2 , and A is a constant. Fig. 4.4(a) and (b) show the representative plots of $(\alpha h\nu)^2$ vs $h\nu$ and $(\alpha h\nu)^{1/2}$ vs $h\nu$ of sample A which indicate both direct and indirect nature of its band-gap. The band-gap values estimated for all the samples using similar plots have been summarized in Table 4.1 which shows that the direct band-gap values in general are higher than the indirect ones. The values and trends of the band-gap are quite consistent with the values reported by Wang et al. [7] and Hasan et al. [8]

RT PL spectra of all samples in Fig. 4.5 contains a sharp UV peak at ~ 3.25 eV and a broad visible peak at ~ 2.25 eV. The UV peak is due to band edge emission and the broad visible peak is generally assigned for the emission from defect related states in TiO_2 . The UV/VIS PL intensity ratio has been calculated for all samples and noted in Table 4.1 which shows that sample A has highest UV/VIS value because of lower intense visible peak. As said earlier, the broad visible peak is very common feature in TiO_2 PL spectra irrespective of its preparation and morphology [9-12].

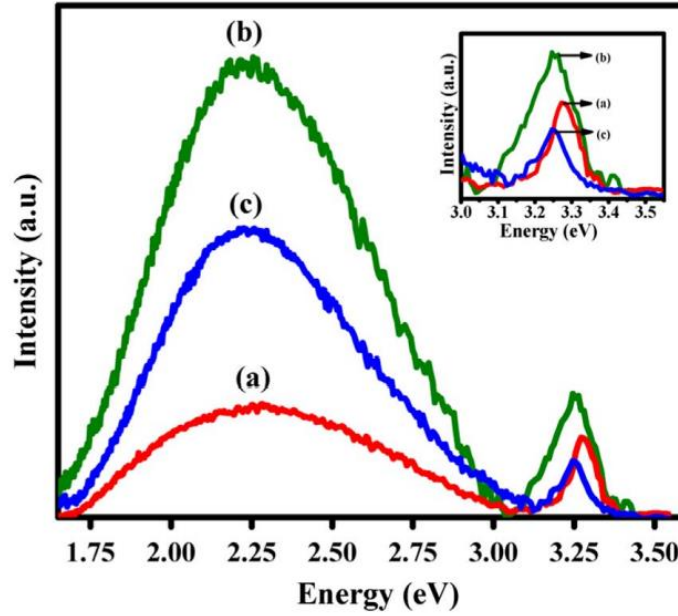


Fig. 4.5: RT PL spectra of (a) Sample A, (b) Sample B, and (c) Sample C. The inset shows an enlarged view of the UV emission.

Different types of trap states or defects are responsible for the broad visible PL in TiO_2 . The possible defects reported for visible PL are V_O , Ti^{3+} , Ti interstitials, impurities, and other defects in the crystal [13-19]. Among these the most accepted source responsible for visible emission is V_O and Ti^{3+} related states [20-23]. According to literature, reduced TiO_2 i.e., TiO_2 containing Ti^{3+} can absorb visible light [24, 25]. Various methods such as high temperature annealing [26], UV treatment [27], high vacuum heating [28], heating in reducing ambient (C [29], H_2 [21] environment), plasma curing [30], laser irradiation [31], bombardment of high energy particle (neutron [32], Ar^+ [33], electron [34], γ - ray [35]) can produce Ti^{3+} surface defects (TSD). There are two mechanisms reported for Ti^{4+} reduction to Ti^{3+} . One, upon UV light electron-hole pairs are generated and these electrons tend to reduce Ti^{4+} cations while the holes are trapped at O_2^- or the oxidized O_2^- [27]. Second process is the loss of oxygen from the TiO_2 surface [26]. It has been suggested that V_O causes two valance electrons in TiO_2 and these excess electrons tend to occupy the empty Ti 3d orbital forming Ti^{3+} . Thus, the both defects are often considered to be produced simultaneously and connectedly. But, according to Liu et al. [21] and Berger et al. [27], TSD is different from V_O as both can be formed separately although both Ti^{3+} defects and V_O can be achieved deliberately by high temperature air and vacuum annealing or UV irradiation. Therefore, though all the samples are supposed to have Ti^{3+} or V_O type defects. Sample B and C are expected to contain more as compared to A. The

higher UV/VIS value of sample A indicates presence of small amount of trap states in it due to the well-established fact that H_2O molecules usually get adsorbed at $\sim 200^\circ\text{C}$. When a sample is cooled down from higher temperature, it may cause OH and O_2 related surface defects in sample [36]. As the sample A is rapidly cooled in N_2 environment, adsorption of OH and/or O_2 is less probable on it.

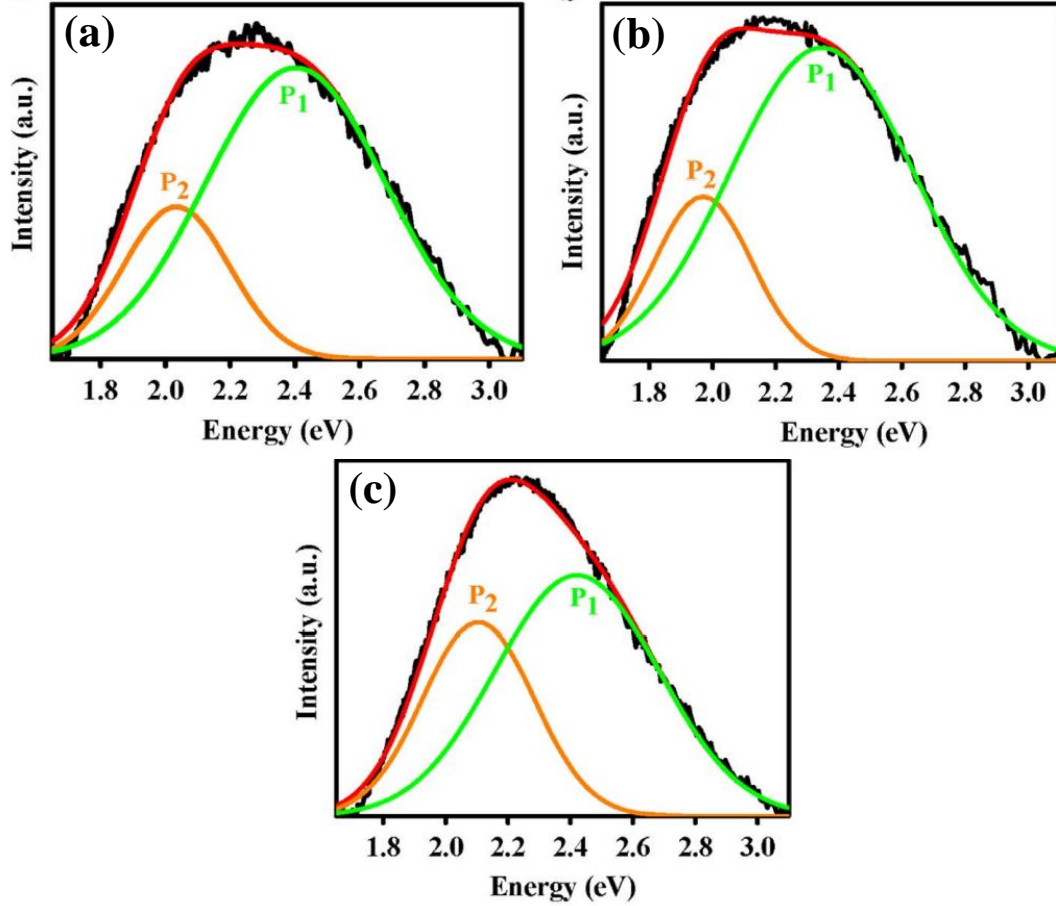


Fig. 4.6: Gaussian multi-peak fitting of the visible photoluminescence spectra of (a) Sample A, (b) Sample B, and (c) Sample C.

Table 4.1. Values of direct, indirect band-gap, UV/VIS, and green/orange emission of the samples.

	Direct band-gap (eV)	Indirect band-gap (eV)	UV/VIS	Green/orange
Sample A	3.39	3.14	0.71	3.21
Sample B	3.46	3.21	0.26	3.57
Sample C	3.35	3.16	0.19	1.80

For further investigation of the emission properties of the samples due to different post-growth treatments and for assigning the probable cause, Gaussian multi-peak fitting has been done for visible PL spectra of all the samples as shown in Fig. 4.6(a)-(c). Each visible peak can be deconvoluted into two sub-peaks, one located at ~ 2.4 eV (green emission, P1) and other at ~ 2 eV (orange emission, P2). It has been also observed that the intensities of the sub-bands vary with the samples that signify different origins of the sub-bands. The ratio of the integrated peak intensity of the two sub-bands (P1/P2) has been calculated by the area under each peak shown in Table 4.1. It also depicts that P1/P2 is comparable for sample A and B but the value is lower for sample C. According to literature, Ti^{3+} and/or V_O defects are usually attributed to green PL in TiO_2 and OH and/or excess O_2 are for orange emission [37]. Actually, the samples possess different amount of both defect concentrations which makes P1/P2 value different for different samples. Since OH and/or excess O_2 related surface states cause orange emission, the sample A should have less these defects due to rapid N_2 cooling [36, 38], making P1/P2 higher. On the other hand, since the sample B is vacuum annealed, it should have more V_O and/or Ti^{3+} defects (as supported by XPS data discussed later) which gives high P1/P2 value. That's why, P1/P2 values are similar for sample A and B. It is well known that UV curing makes TiO_2 surface hydrophilic [39, 40]. Therefore, for sample C, more OH species are adsorbed on the surface that cause more orange emission making lowest P1/P2 value. This result agrees with the work reported by Jin et al. [41], which shows that red band has a strong correlation with the defects with under co-ordinated Ti^{3+} .

To support our results, XPS analysis has been carried out for all samples. The XPS full scan of all samples are shown in Fig. 4.7(a), (c), and (e) which confirms the presence of Ti 2p_{1/2}, Ti 2p_{3/2}, and O 1s_{1/2}. The Ti 2p_{3/2} peak of all samples has been deconvoluted well into two peaks centered at ~ 457 eV and other at ~ 458 eV shown in Fig. 4.7(b), (d), and (f). The lower energy peak is associated

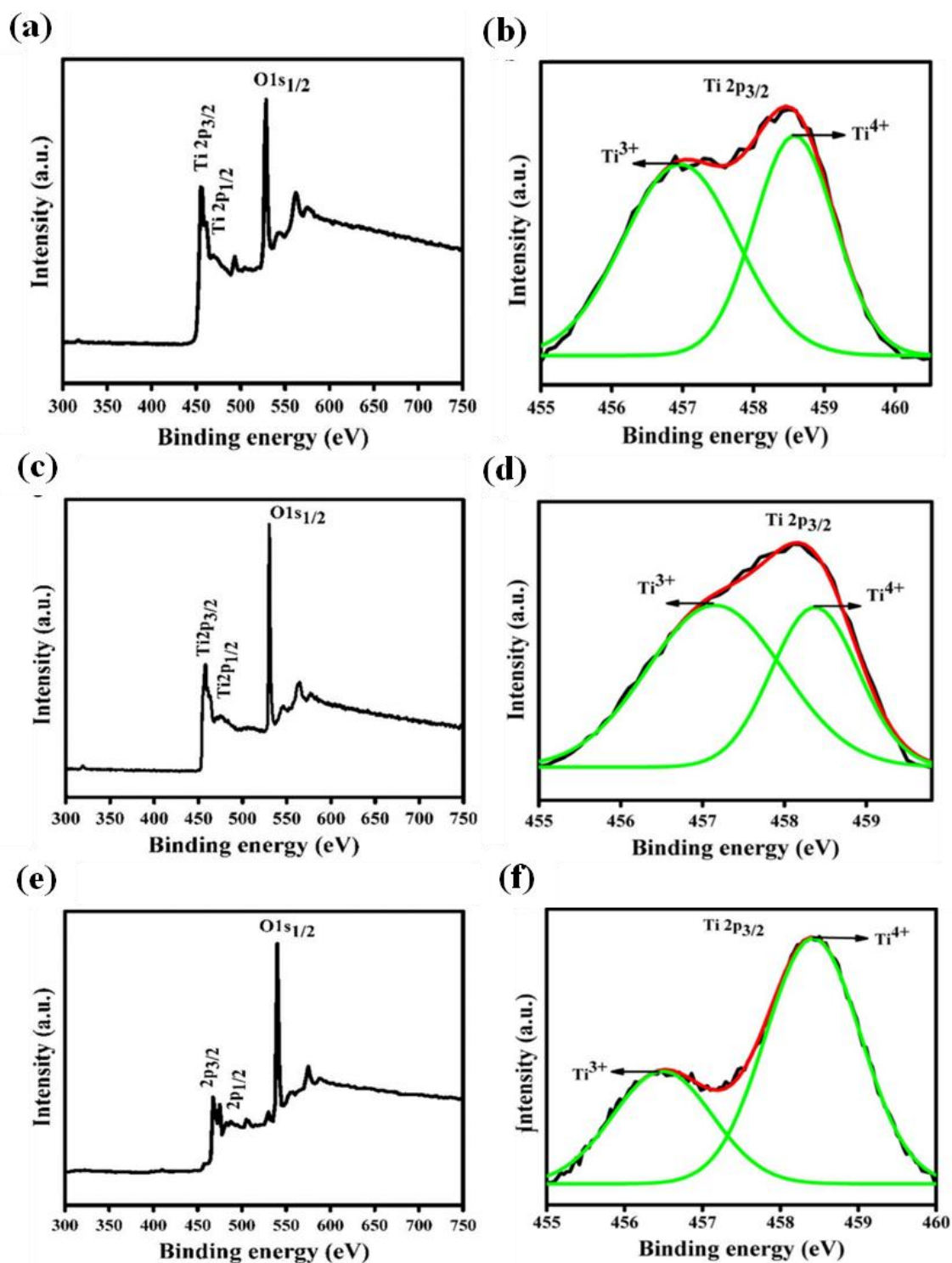


Fig. 4.7: XPS pattern of (a) Sample A, (c) Sample B, and (e) Sample C. Gaussian peak fitting of $\text{Ti } 2p_{3/2}$ peak of (b) Sample A, (d) Sample B, and (f) Sample C.

with Ti³⁺ and the higher energy peak is assigned to Ti⁴⁺ [26]. The estimated ratio of the area under the fitted curve of Ti³⁺ to Ti⁴⁺ has been shown in Table 4.1 which reveals that this value is higher for sample B than that of sample A. It specifies more formation of Ti³⁺ defects in sample B which is at per our PL UV/VIS analyses. The smaller UV/VIS value of sample C than that of sample A and B indicates lesser amount of Ti³⁺ present in it. This agrees with the result that for sample C, green emission is comparable with the orange emission which is caused by the OH and/or excess O₂ adsorption on the TiO₂ surface.

To analyze the relaxation mechanism of charge carriers through the defect states, TCSPC measurement has been performed for all samples. The experimental data has been fitted to bi-exponential decay by the equation [42]:

$$I(t) = B_1 \exp(-t/\tau_1) + B_2 \exp(-t/\tau_2) \quad (4.5)$$

where $I(t)$ is PL intensity, τ_1 and τ_2 are decay constants, and B_1 and B_2 are their relative contributions. The excitation and emission wavelengths have been set at 295 and 380 nm as contrast to PL excitation and emission band. Fig. 4.8(a) shows the representative decay profile of sample C. The two decay constants (τ_1 and τ_2) and their relative contributions (B_1 and B_2) in decay have shown in Table 4.2. Samples B and C exhibit contributions over 90% by slower decay constants as compared to sample A which has very fast decay rate and immeasurable as beyond to instrumental limit. Therefore, this result concludes that vacuum annealing and UV curing both produce defects that slow down the carrier recombination process which lead to larger lifetime value of the carriers. This result also supports our PL analysis of the samples.

Table 4.2. Decay parameters of the samples estimated from TCSPC.

	τ_1 (ps)	B_1	τ_2 (ps)	B_2
Sample A	–	–	–	–
Sample B	216	91.66	1443	8.34
Sample C	272	91.71	2597	8.29

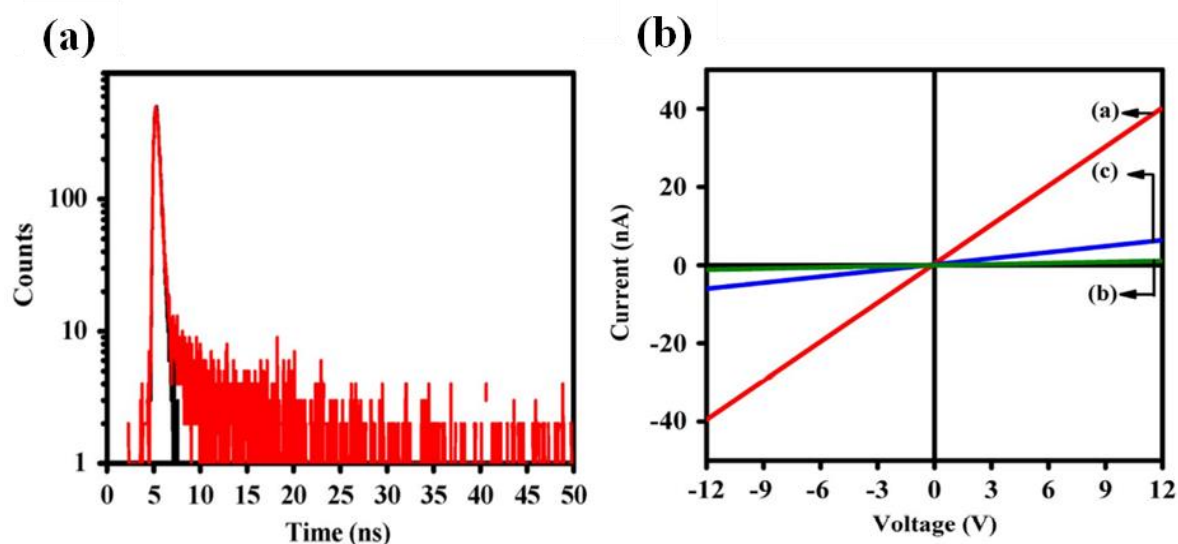


Fig. 4.8: (a) Representative time resolved UV PL decay profile of Sample C (b) Room temperature dark I - V curves of (a) Sample A, (b) Sample B, and (c) Sample C.

In Fig. 4.8(b), the dark I - V characteristics of the samples at bias -10 V to 10 V exhibiting linear characteristics of the curves show the Ohmic nature of the contacts. Sample A possesses maximum current due to lowest amount of carrier traps and sample B shows minimum current value because of large number of traps present due to formation of Ti^{3+} surface defects. This result is at par with our PL, XPS, and TCSPC studies.

4.4 Conclusions

In summary, PL properties of easy and low cost sol-gel TiO_2 films under various post-growth treatments have been demonstrated in this study. It has been found that annealing in air followed by rapid cooling is a very useful method to achieve higher UV emission and lower visible emission which is probably due to the reduction of number of surface traps in air annealing. Also, it has been observed that UV curing and vacuum annealing can create more V_O and/or Ti^{3+} states. Therefore, the recombination pathway exhibits a clear correlation with the formation of Ti^{3+} defects on the surface. This study leads to a very efficient and promising way for the fabrication of highly luminescent oxides.

4.5 References

- [1] S. Wang, S. Tang, H. Gao, X. Chen, H. Liu, C. Yu, Z. Yin, X. Zhao, X. Pan, and H. Yang, *Optical Materials*, **118** (2021) 111273
- [2] D. Komaraiah, E. Radha, J. Sivakumar, M. R. Reddy, and R. Sayanna, *Optical Materials*, **108** (2020) 110401
- [3] K. Tam, C. Cheung, Y. Leung, A. Djurišić, C. Ling, C. Beling, S. Fung, W. M. Kwok, W. Chan, and D. Phillips, *The Journal of Physical Chemistry B*, **110** (2006) 20865-20871
- [4] N. D. Abazović, M. I. Čomor, M. D. Dramićanin, D. J. Jovanović, S. P. Ahrenkiel, and J. M. Nedeljković, *The Journal of Physical Chemistry B*, **110** (2006) 25366-25370
- [5] A. Di Paola, M. Bellardita, and L. Palmisano, *Catalysts*, **3** (2013) 36-73
- [6] R. Swanepoel, *Journal of Physics E: Scientific Instruments*, **16** (1983) 1214
- [7] Z. Wang, U. Helmersson, and P.-O. Käll, *Thin Solid Films*, **405** (2002) 50-54
- [8] M. Hasan, *Opt. Mater.(Amst)*, **32** (2010) 690-695
- [9] L. Chetibi, T. Busko, N. P. Kulish, D. Hamana, S. Chaieb, and S. Achour, *Journal of Nanoparticle Research*, **19** (2017) 1-9
- [10] F. J. Knorr, D. Zhang, and J. L. McHale, *Langmuir*, **23** (2007) 8686-8690
- [11] W. Zhang, M. Zhang, Z. Yin, and Q. Chen, *Applied Physics B*, **70** (2000) 261-265
- [12] W. Zhang, M. Zhang, and Z. Yin, *physica status solidi (a)*, **179** (2000) 319-327
- [13] S. Mathew, T. Benoy, P. Rakesh, M. Hari, T. Libish, P. Radhakrishnan, V. Nampoori, and C. Vallabhan, *Journal of fluorescence*, **22** (2012) 1563-1569
- [14] D. Li, H. Haneda, N. K. Labhsetwar, S. Hishita, and N. Ohashi, *Chemical Physics Letters*, **401** (2005) 579-584
- [15] T. Sekiya, S. Kamei, and S. Kurita, *Journal of luminescence*, **87** (2000) 1140-1142
- [16] Y. Lei, L.-D. Zhang, G.-W. Meng, G.-H. Li, X. Y. Zhang, C. Liang, W. Chen, and S. Wang, *Applied physics letters*, **78** (2001) 1125-1127
- [17] B. Santara, P. Giri, K. Imakita, and M. Fujii, *The Journal of Physical Chemistry C*, **117** (2013) 23402-23411
- [18] B. Dong, T. Liu, C. Li, and F. Zhang, *Chinese Chemical Letters*, **29** (2018) 671-680
- [19] T. Sekiya, T. Yagisawa, N. Kamiya, D. Das Mulmi, S. Kurita, Y. Murakami, and T. Kodaira, *Journal of the Physical Society of Japan*, **73** (2004) 703-710
- [20] Y.-H. Chang, C.-M. Liu, C. Chen, and H.-E. Cheng, *Journal of the Electrochemical Society*, **159** (2012) D401
- [21] H. Liu, H. Ma, X. Li, W. Li, M. Wu, and X. Bao, *Chemosphere*, **50** (2003) 39-46
- [22] X. Xin, T. Xu, J. Yin, L. Wang, and C. Wang, *Applied Catalysis B: Environmental*, **176** (2015) 354-362
- [23] K. Suriye, P. Praserttham, and B. Jongsomjit, *Applied Surface Science*, **253** (2007) 3849-3855
- [24] D. Li, N. Ohashi, S. Hishita, T. Kolodiaznyi, and H. Haneda, *Journal of Solid State Chemistry*, **178** (2005) 3293-3302
- [25] P. Zheng, W. Zhou, Y. Wang, D. Ren, J. Zhao, and S. Guo, *Applied Surface Science*, **512** (2020) 144549
- [26] L. Xiong, J. Li, B. Yang, and Y. Yu, *Properties and Photocatalytic Application, J Nanomater*, (2012)
- [27] T. Berger, M. Sterrer, O. Diwald, E. Knözinger, D. Panayotov, T. L. Thompson, and J. T. Yates, *The Journal of Physical Chemistry B*, **109** (2005) 6061-6068
- [28] U. Diebold, J. Lehman, T. Mahmoud, M. Kuhn, G. Leonardelli, W. Hebenstreit, M. Schmid, and P. Varga, *Surface science*, **411** (1998) 137-153
- [29] Y. Li, X. Li, J. Li, and J. Yin, *Materials Letters*, **59** (2005) 2659-2663

- [30] I. Nakamura, N. Negishi, S. Kutsuna, T. Ihara, S. Sugihara, and K. Takeuchi, *Journal of Molecular Catalysis A: Chemical*, **161** (2000) 205-212
- [31] T. Le Mercier, J.-M. Mariot, P. Parent, M.-F. Fontaine, C. Hague, and M. Quarton, *Applied surface science*, **86** (1995) 382-386
- [32] Z. Yuan, W. Xiao-Xuan, H. Lv, and Z. Wen-Chen, *Journal of Physics and Chemistry of Solids*, **68** (2007) 1652-1655
- [33] J. M. Pan, B. Maschhoff, U. Diebold, and T. Madey, *Journal of Vacuum Science & Technology A: Vacuum, Surfaces, and Films*, **10** (1992) 2470-2476
- [34] J. Jun, M. Dhayal, J.-H. Shin, J.-C. Kim, and N. Getoff, *Radiation physics and chemistry*, **75** (2006) 583-589
- [35] S. Dohshi, M. Anpo, S. Okuda, and T. Kojima, *Topics in Catalysis*, **35** (2005) 327-330
- [36] H. Zhou, H. Alves, D. Hofmann, W. Kriegseis, B. Meyer, G. Kaczmarczyk, and A. Hoffmann, *Applied physics letters*, **80** (2002) 210-212
- [37] A. Stevanovic, M. Büttner, Z. Zhang, and J. T. Yates Jr, *Journal of the American Chemical Society*, **134** (2012) 324-332
- [38] S. Ghosh, and D. Basak, *RSC advances*, **7** (2017) 694-703
- [39] H. Jiang, and L. Gao, *Materials chemistry and Physics*, **77** (2003) 878-881
- [40] A. G. Agrios, and P. Pichat, *Journal of Applied Electrochemistry*, **35** (2005) 655-663
- [41] C. Jin, B. Liu, Z. Lei, and J. Sun, *Nanoscale research letters*, **10** (2015) 1-9
- [42] Concentration dependence of the fluorescence decay profile in transition metal doped chalcogenide glass, *Proceedings of the Optical Components and Materials IV*, (**2007**)

CHAPTER-5

Development of TiO₂ thin films as ultraviolet photodetector via defects tuning

Contents of this chapter has been published in *Applied Surface Science*, 427, 814–822, (2018).

5.1 Introduction

Photodetectors based on photoconducting principle employ a single semiconducting layer indicating a much easier synthesis process over the complicated fabrication procedure of conventional photodetectors that mainly work in photodiode mode [1]. Also, from the previous chapter it is established that photoconductivity of TiO₂ films highly depends on the sub-band-gap density of states mainly originated from V_O and surface adsorbed species [2-6]. Therefore, choice of meticulous processing is necessary to engineer these defects for attaining high and efficient UV photodetection property of TiO₂. Therefore, having these issues in mind, in this chapter, UV photodetection properties of sol-gel derived nanocrystal assembled TiO₂ thin films in simple photoconductive geometry have been discussed where the defect concentration has been varied to a different extent by various post-growth treatments.

5.2 Experimental details

TiO₂ films have been deposited on properly cleaned soda-lime glass substrates by sol-gel spin coating method. The details of the sol preparation and film synthesis procedure have been described in chapter 3. Each coating has been dried at 120 °C for 10 minutes and then heated at 500 °C for 20 minutes. After 20th coating, different post-growth treatments have been performed to tune film properties: (i) annealing at 500 °C in air ambient for 2 hours (SA) (ii) annealing at 500 °C in vacuum for 2 hours (SB) (iii) Irradiance of UV light (365 nm, 1.2 mW) in air ambient at RT for 2 hours (SC).

The structural, microstructural, and optical properties of the thin films have been investigated by using the XRD, XPS, FESEM, AFM, and UV-VIS spectroscopy. For the photoconductivity measurements, two circular Al top electrodes (thickness ~ 40 nm having diameter 1mm and 2mm distance apart) have been thermally evaporated on the film surface.

5.3 Results and discussions

In Fig. 5.1(a), the XRD patterns of all the samples show the presence of multiple peaks at $2\theta = 25.3^\circ$, 37.8° , 48.0° , 53.9° , and 62.7° corresponding to the (101), (004), (200), (105), and (204) diffraction peaks which confirms the tetragonal anatase phase of TiO₂ according to JCPDS data

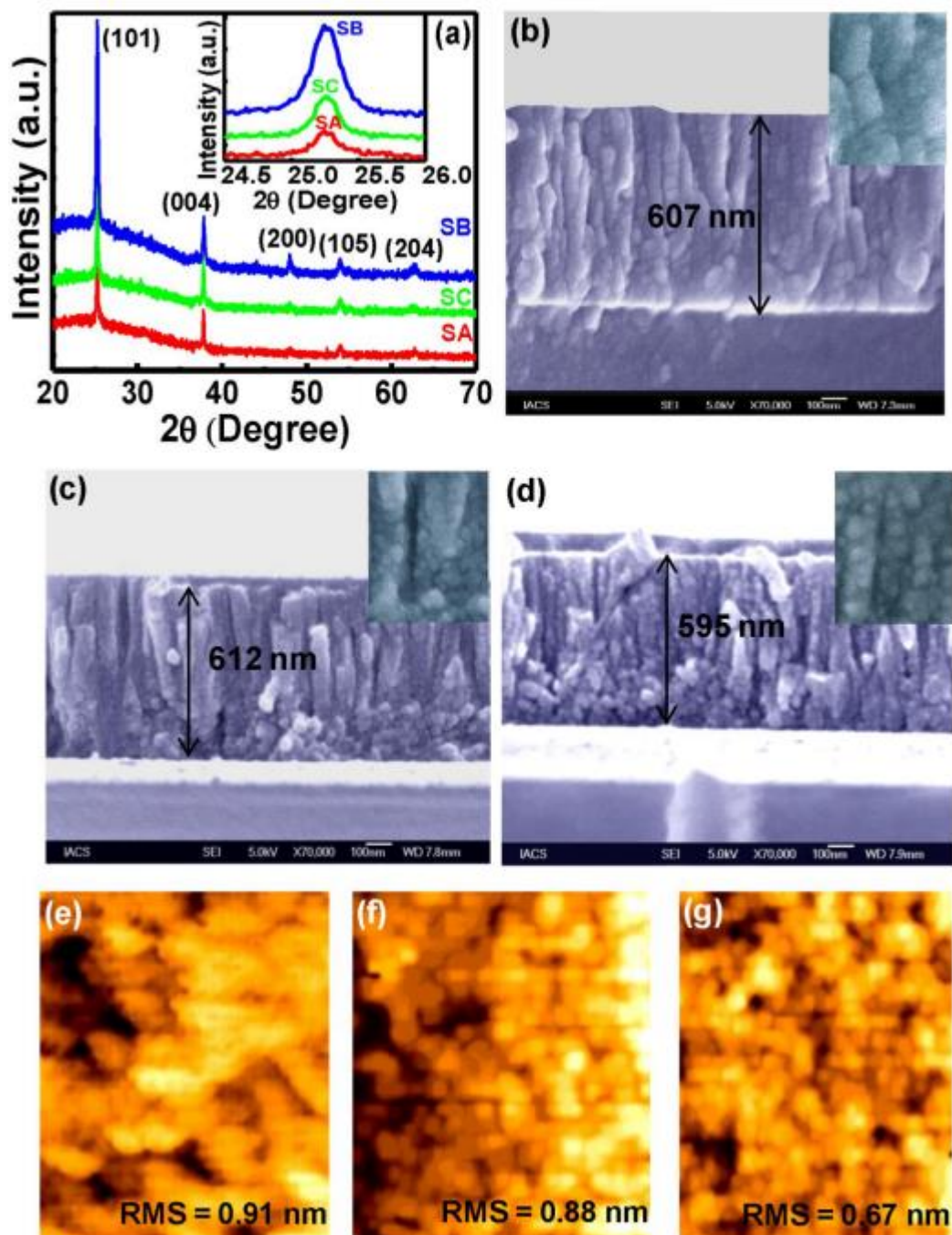


Fig. 5.1: (a) XRD patterns of all the samples. The inset in the figure shows the enlarged view of (101) peak. The cross-sectional SEM images of (b) SA, (c) SB, and (d) SC. The inset in the respective figure shows the magnified view of the columns. AFM images of (e) SA, (f) SB, and (g) SC.

(PDF# 211272). From the enlarged view of (101) peak in the inset, full width at half maxima (FWHM) for all films has been calculated as 0.15, 0.17, and 0.2 for SA, SB, and SC respectively that indicates no notable change in crystallinity of the samples. The cross-sectional FESEM images in the Fig. 5.1(b)-(d) depict the vertical and columnar growth of the samples. Careful scanning of the columns (the insets in the figures) reveals that the columns are assembled of tiny crystallites which increases the resultant surface-to-volume ratio. The thicknesses of the samples are estimated from cross-section as 607 nm, 612 nm, and 595 nm for SA, SB, and SC respectively which matches appreciably with the thickness values calculated by Swanepoel's method [7] as stated in chapter 4. The surface topography of the films has been examined using tapping mode AFM (Fig. 5.1(e)-(g)) which show smooth, homogeneous surface of densely packed small grains of the films. The root mean square (RMS) roughness of the samples, deduced from AFM images has values 0.91 nm, 0.88 nm, and 0.67 nm for SA, SB, and SC respectively indicating uniform nature of the film surface. These images are also too smooth to distinguish any microscopic change in the characteristics.

The optical absorption spectra of all the films, shown in Fig. 5.2(a) exhibit a strong and sharp rise in the region below 400 nm due to highly absorption of photons near the band-gap of TiO_2 as stated earlier chapter. The indirect band-gap values have been estimated from Tauc plot (inset of Fig. 5.2(a)) as 3.12 eV, 3.23 eV, and 3.24 eV for SA, SB, and SC respectively identifying no significant change. The dark I - V characteristics (Fig. 5.2(b)) of the samples has been measured in the bias of -20 V to 20 V which exhibit a linear increase of current with voltage confirming Ohmic nature of the contacts. It has been observed that dark current value of SB is higher than that of SA and SC. This may be due to elimination of O_2 -related carrier traps during vacuum annealing [8-10]. The schematic of the photoconductivity measurement has been presented in the inset of Fig. 5.2(b).

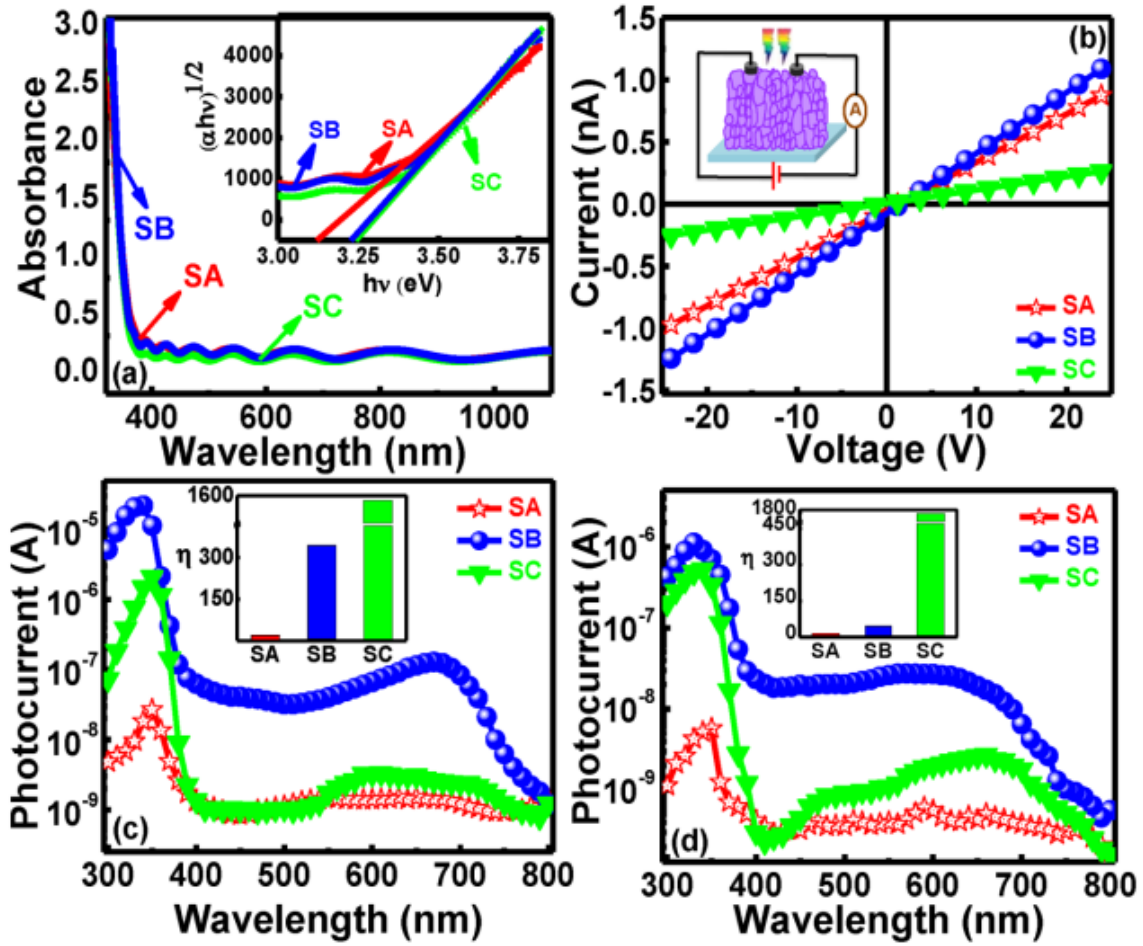


Fig. 5.2: (a) Absorption spectra of the samples. Inset shows the corresponding Tauc plots for the samples. (b) Dark I - V of samples. Inset shows the schematic diagram of experimental set-up for photoconductivity measurement, and Photocurrent spectra of the samples at 10 V for (c) high and (d) low incident power respectively. Inset shows the corresponding value of UV-to-visible rejection ratio.

For detailed analysis, the spectral photoresponse of all the films at the wavelength in the region of 300-800 nm under high and low incident power at 10 V fixed bias condition has been measured and shown in Fig. 5.2(c) and (d) respectively where the insets show the wavelength dependent power variations. All the photocurrent spectra exhibit a strong and sharp rise in the current value below 400 nm indicating the high sensitivity towards UV light due to band edge transition. A broad hump has been observed in the visible region (450-700 nm) due to relaxations of photocarriers from different trap states. However, the nature of hump is different for different films due to varied nature and amount of sub-band defect states present in the films. The UV-to-visible rejection ratio, termed as η (the ratio of photocurrent at 350 nm to

that of 410 nm), defines how blind a UV photodetector towards the visible light (i.e., 410 nm) w.r.t UV (i.e., 350 nm). η has been calculated for all samples and shown in the inset of Fig. 5.2(c) and (d) showing η is quite higher for SC than SA and SB indicating its better photodetection towards visible-blindness. Comparing the data recorded for high and low intense incident light, it has been observed that the detection of low power UV light is higher than that of high incident power by SC. This result specifies that the UV light absorption by the surface is more effective in bringing a pronounced change in the photoresponse since penetration of low power UV light is mainly confined on the surface. An extremely high rejection ratio (1.7×10^3) has been found for low incident UV light ($10 \mu\text{W}$ for 350 nm) for SC indicates its fantastic performance for low intense UV detection. This value is much higher with the value reported by Liu et al. [11]

The corresponding spectral responsivity (R) and specific detectivity (D) of the films have been calculated using the formula as mentioned in chapter 3. The responsivity vs corresponding wavelength at high and low power density has been shown in the Fig. 5.3(a) and (b) respectively and the insets show the wavelength dependent power (used for responsivity calculation) plots of the monochromatic lights. The R values for both SB and SC reach $\sim 2\text{-}5$ A/W at 330 nm for lower power ($7.6 \mu\text{W}$) implying their efficient low power UV detection. This results are much higher than that of TiO_2 -based photodetector as reported by Wang et al. [12]. Xing et al. [13] also fabricated TiO_2 -based metal-semiconductor-metal (MSM) photodetector and they have found R value of 3.63 A/W at 10 V bias under 1.87 mW/cm^2 incident UV radiation. The detectivity vs wavelength plots shown in the Fig 5.3(b) and (d) depict that D values in lower intense incident light are also greater than the higher intense incident light for SB and SC and the estimated D values for the lower power for the samples SB and SC are in the range of $6\text{-}7 \times 10^{13}$ Jones which is very high compared to the value as reported by Liu et al. [14]

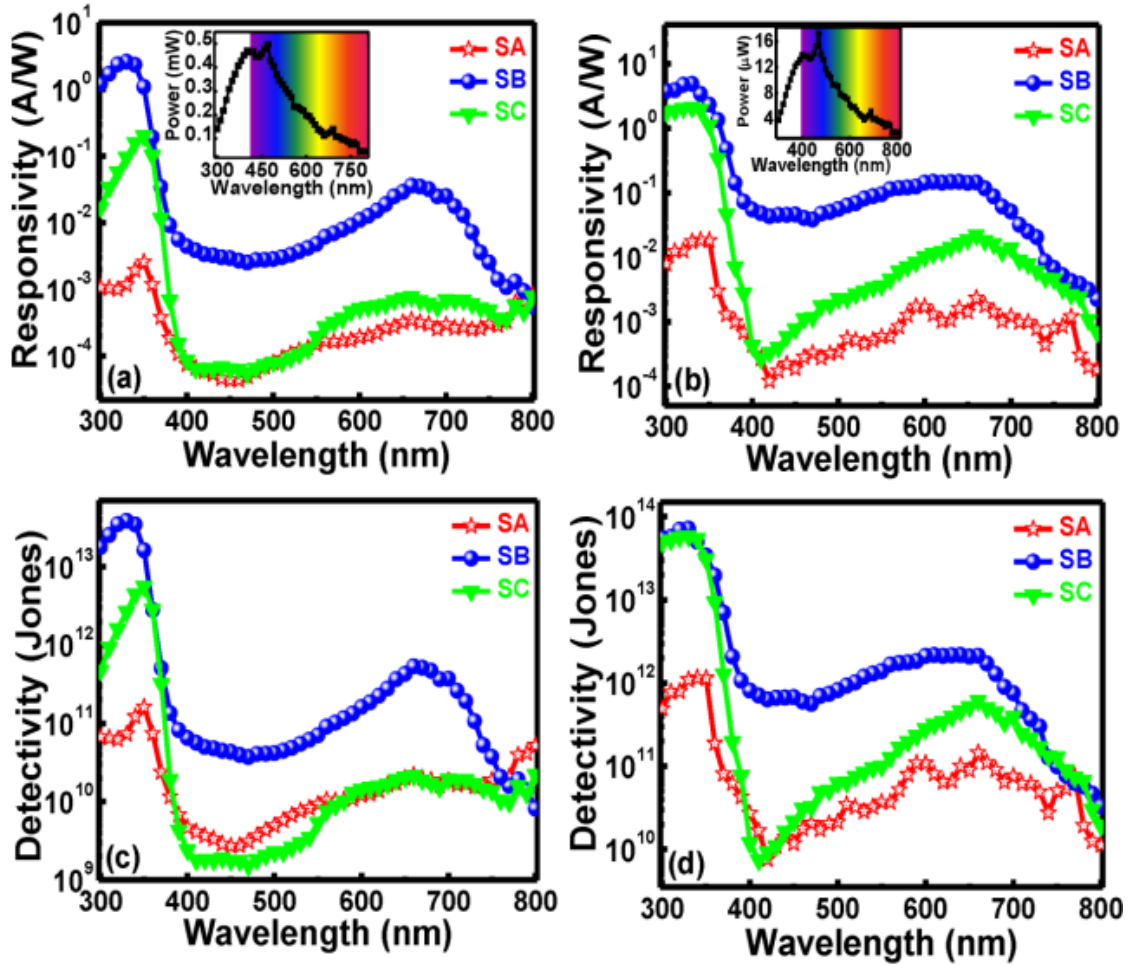


Fig. 5.3: Spectral responsivity of samples for (a) high and (b) low incident power density at 10 V bias. The insets show the variation of power of monochromatic light with wavelength. Specific detectivity of the samples for (a) high and (b) low power density at 10 V bias.

The transient photoresponse under UV illumination (350 nm) with the variation of low to high intensity (10 to 350 μ W) at a fixed bias of 10 V has been carried out for all the films and presented in Fig. 5.4(a)-(c) for the SA, SB, and SC respectively. The samples are exposed to UV light for 15 minutes and simultaneously the photocurrent has been measured. The nature of the curve for SA is completely different from SB and SC. For SA, as soon as the UV light is shinned on the sample, instantaneously current increases and when light is switched off, the current value drops very fast attaining almost its dark value. Under steady UV illumination, there is a photocurrent relaxation

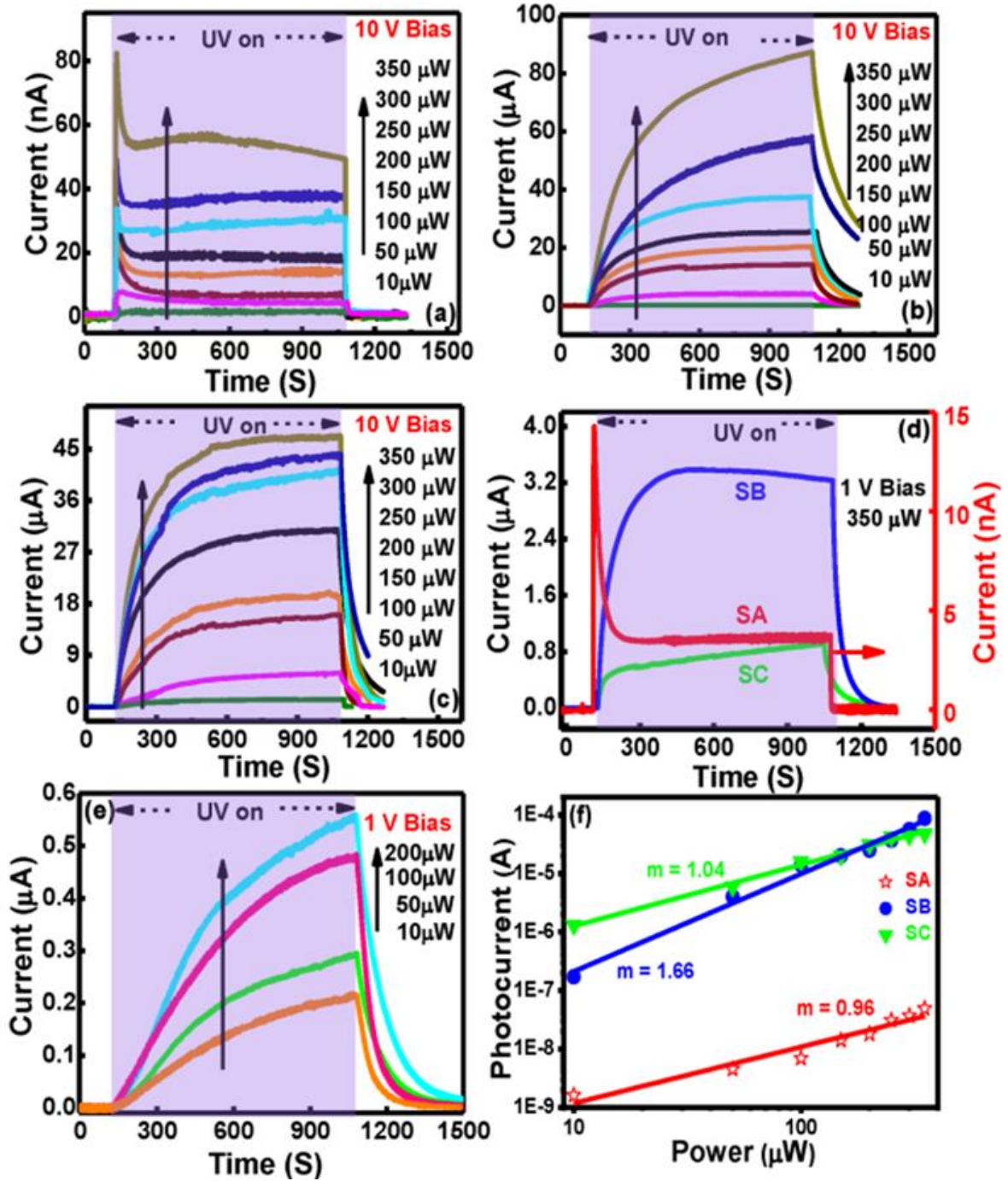


Fig. 5.4: Transient photoresponse curves at 10 V bias for various incident powers of UV light for (a) SA, (b) SB, and (c) SC. (d) Transient photoresponse of all the samples at 1 V bias and 350 μW UV irradiance. (e) Transient photoresponse curves of SC at 1 V bias for various power values. (f) Power dependence of the photocurrent at 10 V and corresponding fitting of photocurrent for all the samples.

in SA similar to the state-of-the-art reported previously for ZnO where no such behavior has been observed for SB and SC [15]. For SB and SC, the rise and decay processes are slow compared to SA. From Fig. 5.4(b) and (c), it has been seen that SB and SC are highly sensitive to as low as 10 μ W incident UV power. The samples also show very good photoresponse upon 350 μ W UV irradiance even at very low (1 V) bias as observed from Fig. 5.4(d). The dark current (I_d), photocurrent (I_{ph}), and I_{ph}/I_d (photosensitivity) for all samples at three conditions: low power and high bias, high power and low bias, and high power and high bias have been summarized in Table 5.1. It has been observed that I_d values of the samples do not vary so much but there is wide variation in steady I_{ph} values depending on the intensity and bias voltage. The photosensitivity is maximum for SC for all three conditions directs better UV detection than other two. Low incident power UV light even causes an I_{ph}/I_d ratio of $\sim 10^4$ for SC (Fig. 5.4(c)). Under 1 V bias condition (Fig. 5.4(d)), the value becomes 9×10^4 thus which can be applied in low on-chip power consumption. Dutta et al. [16] had found photo-to-dark current ratio of 23 for ZnO films at 5 V bias condition although N doping has improved the value marginally. Bera et al. [17] had reported the highest photo-to-dark current ratio of 9×10^4 at 3 V bias for ZnO NRs. Therefore, as compared to the ZnO films and NRs, the photoresponse of TiO₂ film at only 1 V bias condition is much higher. Here, Ti³⁺ defects and surface adsorbed species play prominent role in photoconductivity of TiO₂ [18, 19]. Ti³⁺ defects are formed when an electron is trapped by an under co-ordinated Ti⁴⁺ sites [20, 21] and these sites behave as active sites for adsorbing OH groups which make TiO₂ surface hydrophilic [22]. The photocurrent is managed by a competition between two electron loss processes: electron-hole recombination and electron scavenging. The surface adsorbed oxygen creates a large number of electron scavengers, O²⁻ [23, 24], which shortens the electron life time and hence diminishes photoconductivity. On the other hand, holes created due to photo excitation are trapped by the O²⁻ preventing electron-hole recombination and thus increase the lifetime of the electrons. Therefore, highest photocurrent value is built depending on both processes which wins the race [25]. Most interestingly, SC exhibits very good UV sensitivity at 1 V bias and under UV light of 10, 50, 100, and 200 μ W intensity as shown in Fig. 5.4(e). The calculated photosensitivity values are as high as 1.0×10^4 , 1.8×10^4 , 2.9×10^4 and 3.5×10^4 at 10, 50, 100 and 200 μ W UV irradiation respectively which signify very efficient UV photodetection at low intensity and low biased condition. From the Fig. 5.4(a)-(c), it is clearly shown that the photocurrent obviously depends on the power of the incident UV light, and increases significantly with increasing incident power of light which can be attributed to the change in photogenerated

carriers. The dependence of the photocurrent on the incident light intensity can be fitted by a simple power law [26, 27]: $I_{ph} = BP^m$ where B is a scaling constant at a specific wavelength, P is the varied power of the incident light, and m is an exponent. The linear fitting of the logarithmic plots of I_{ph} vs P in Fig. 5.4(e) with estimated values of m are 0.96, 1.66, and 1.04 for the SA, SB, and SC respectively. The linear power dependence of SC indicates electron-hole generation, without recombination within the semiconductor [28]. However, superlinear photocurrent variation in SA and SB is not clear now and will be investigated later.

Table 5.1. The values of dark current (I_d), photocurrent (I_{ph}), and I_{ph}/I_d for all the films.

	Low power, high voltage			High power, low voltage			High power, High voltage		
	I_d (A)	I_{ph} (A)	I_{ph}/I_d	I_d (A)	I_{ph} (A)	I_{ph}/I_d	I_d (A)	I_{ph} (A)	I_{ph}/I_d
SA	2.4×10^{-10}	1.5×10^{-9}	6.0	5.7×10^{-11}	3.63×10^{-9}	63	2.4×10^{-10}	5.5×10^{-8}	2.3×10^2
SB	4.3×10^{-10}	1.7×10^{-7}	4.0×10^2	4.0×10^{-11}	3.38×10^{-6}	8.5×10^4	4.3×10^{-10}	7.4×10^{-5}	1.7×10^5
SC	1.1×10^{-10}	1.3×10^{-6}	1.2×10^4	7.9×10^{-12}	7.39×10^{-7}	9.0×10^4	1.1×10^{-10}	4.6×10^{-5}	4.2×10^5

To further analyze the chemical states of elements as well as the defect states present in the films, XPS study has been performed for all samples. The XPS full scan has been presented in the insets Fig. 5.5(a), (c), and (e) which confirm the presence of Ti 2p, Ti 2s and O 1s for all the samples. For all samples, Ti 2p_{3/2} peak has been deconvoluted into two peaks using Gaussian multi-peak fitting, one peak centered at ~ 457 eV and other at ~ 458 eV which have been assigned to Ti³⁺ and Ti⁴⁺ respectively as stated in chapter 4. The ratio between the area fitted under the curves of Ti³⁺ to Ti⁴⁺ i.e., Ti³⁺/Ti⁴⁺ has been calculated for each sample (shown in the corresponding figures) which indicates lower concentration of Ti³⁺ in SC as compared to SA and SB. Similarly, O 1s core level peak for all the samples has been well fitted into three peaks centered at ~ 530 eV, 530.6 eV, and 531.7 eV (Fig. 5 (b), (d), and (f)). The lower energy peak centered at ~ 530 eV has been associated to lattice oxygen (Ti-O-Ti). The middle and higher energy peaks have been assigned to the surface adsorbed O₂ and the surface OH species (Ti-OH) respectively [29].

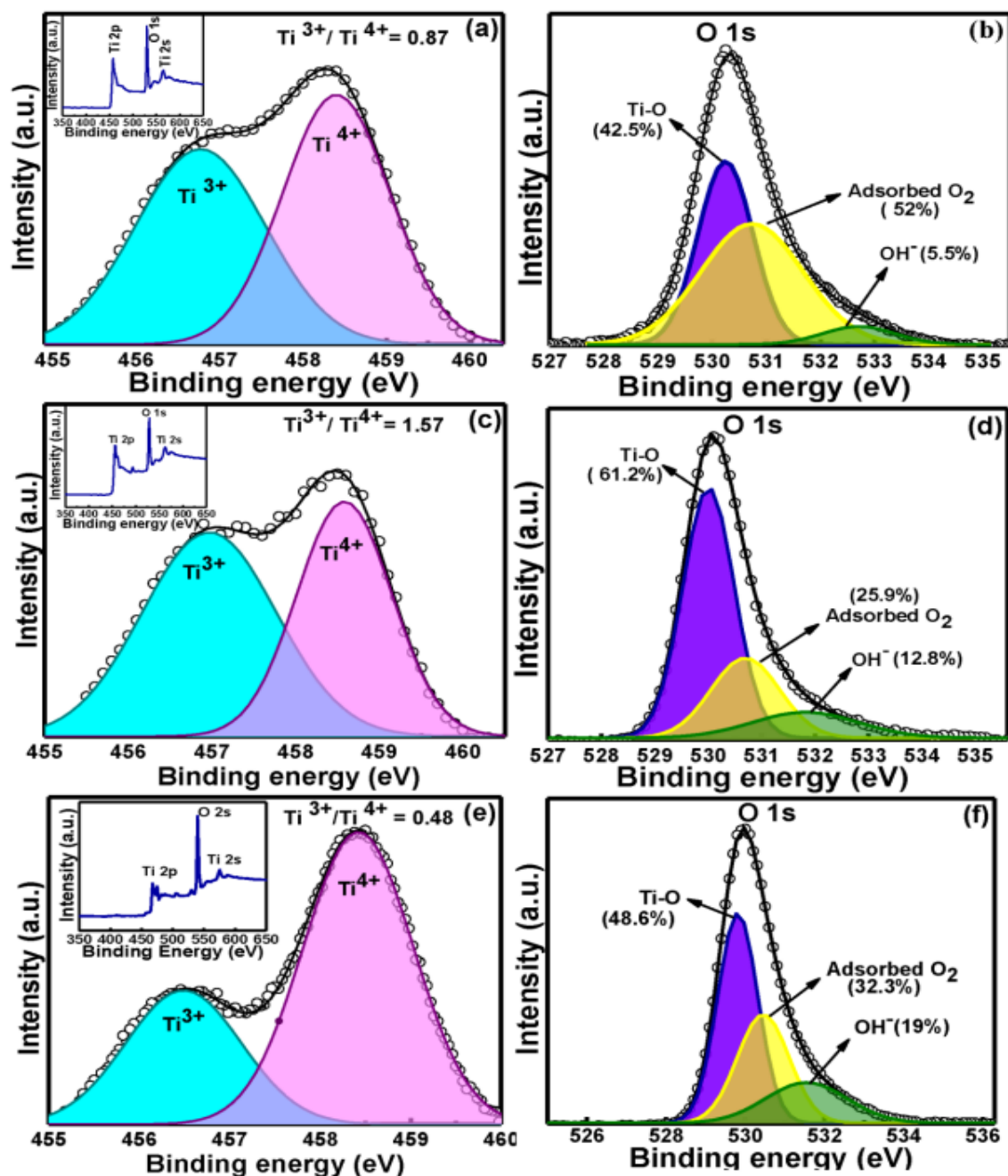


Fig. 5.5: Ti 2p_{3/2} peak fitting for (a) SA, (c) SB, and (e) SC. The Insets show full scan of the XPS spectrum for the corresponding samples. O 1s peak fitting for (b) SA, (d) SB, and (f) SC. The contribution of each of the fitted peak is shown in the figures for all samples.

Therefore, the presence of lower Ti^{3+} and higher OH content [22] is certainly related to electron scavenging as per equation through the reduction reaction as follows: $\text{Ti}^{3+} + \text{H}_2\text{O} \rightarrow \text{Ti}^{4+}\text{-OH} + 1/2\text{H}_2$ [29]. That's why the highest I_{ph}/I_d value at low incident power UV irradiation (in which case the contribution of photocurrent mainly comes from the surface due to low penetration ability) has been obtained (as shown in Table 5.1) for SC and depending on the OH content in sample, photocurrent value of SA and SB varies.

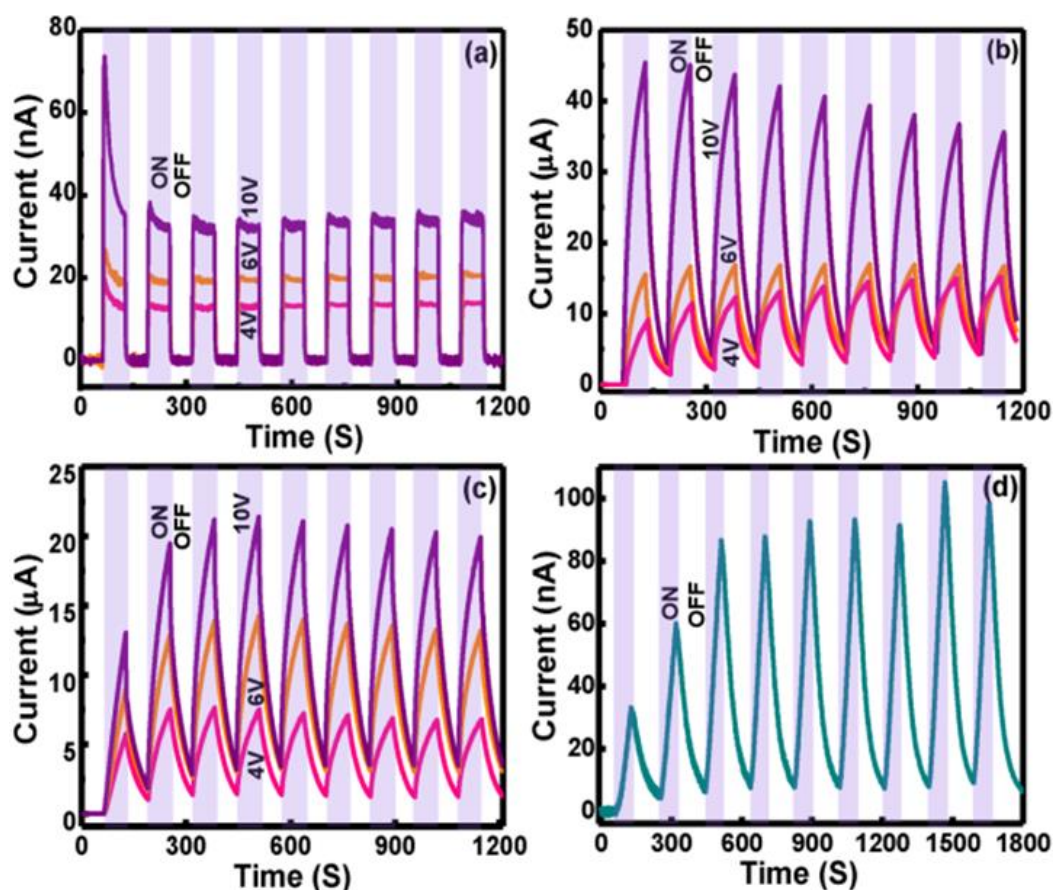


Fig. 5.6: Time dependent growth-decay cycles at three fixed bias conditions for (a) SA, (b) SB, and (c) SC respectively for 350 μW UV illumination. (d) Growth-decay cycle of SC at low bias (1 V) and low incident power (10 μW).

The photocurrent growth and decay cycles of SA, SB, and SC under periodic (1 min) UV illumination (350 nm, 350 μW) at three fixed bias conditions (4V, 6V, 10V) have been also measured and shown in the Fig. 5.6(a)-(c) respectively. Photocurrent relaxation has been observed in SA for the first cycle while the maximum photocurrent value remains the same after several cycles for all bias conditions indicating good stability of photodetection. From the Fig. 5.6(d), it is clear that the photoresponse cyclability of SC at very low bias and low incident

power is interestingly good. The stability of the detector after prolonged UV exposure in Fig. 5.7 shows that the photocurrent slightly increases which may be due to a slow photoresponse of the sample but average response of the detector remains almost same.

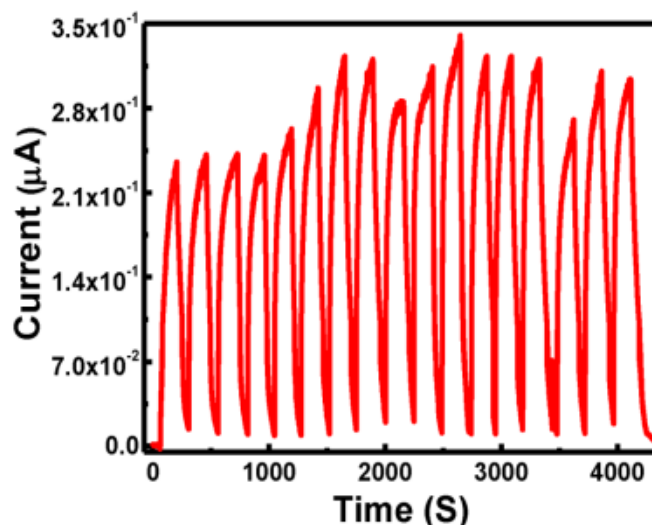


Fig. 5.7: Stability of the detector after prolonged exposure to UV light at 10 V bias and 350 μ W UV irradiation.

5.4 Conclusions

In summary, a comprehensive study on UV photodetection properties of nanocrystal assembled sol-gel TiO₂ films followed by various post-growth treatments have been carried out. The UV cured TiO₂ film shows very high UV-to-visible rejection ratio of 1.7×10^3 for only 10 μ W incident power at 10 V bias condition. Very high photo-to-dark current ratio ($\sim 10^4$) of the film under as low as 1 V bias and only 10 μ W incident power without any device fabrication is extraordinarily notable. This work shows that the post-growth treatments control the surface defect states meaningfully that lead to a strong effect on UV photoresponse properties of the samples. Our study also reveals that simple sol-gel derived and post-growth treated nanocrystal assembled TiO₂ films can be promising candidate for efficient UV photodetection.

5.5 References

- [1] B. N. Pal, I. Robel, A. Mohite, R. Laocharoensuk, D. J. Werder, and V. I. Klimov, *Advanced Functional Materials*, **22** (2012) 1741-1748
- [2] M.-H. Kim, S.-I. Lee, T.-K. Song, H. Park, W. Choi, H.-I. Yoo, and T.-G. Park, *Korean Journal of Chemical Engineering*, **18** (2001) 873-878
- [3] M. Eltermann, V. Kiisk, A. Kikas, S. Lange, and R. Jaaniso, *Sensors and Actuators B: Chemical*, **303** (2020) 127236
- [4] M. Takeuchi, *physica status solidi (a)*, **55** (1979) 653-659
- [5] T. Yan, S. Cai, Z. Hu, Z. Li, and X. Fang, *The Journal of Physical Chemistry Letters*, **12** (2021) 9912-9918
- [6] N. Golego, S. Studenikin, and M. Cocivera, *Physical Review B*, **61** (2000) 8262
- [7] R. Swanepoel, *Journal of Physics E: Scientific Instruments*, **16** (1983) 1214
- [8] K. Pomoni, A. Vomvas, and C. Trapalis, *Thin Solid Films*, **516** (2008) 1271-1278
- [9] A. Vomvas, K. Pomoni, C. Trapalis, and N. Todorova, *Materials Science-Poland*, **25** (2007) 809-816
- [10] S. S. Hegedus, *Journal of applied physics*, **92** (2002) 620-626
- [11] Z. Liu, F. Li, S. Li, C. Hu, W. Wang, F. Wang, F. Lin, and H. Wang, *Scientific reports*, **5** (2015) 1-7
- [12] W. Wang, C. Shan, H. Zhu, F. Ma, D. Shen, X. Fan, and K. Choy, *Journal of Physics D: Applied Physics*, **43** (2010) 045102
- [13] J. Xing, H. Wei, E.-J. Guo, and F. Yang, *Journal of Physics D: Applied Physics*, **44** (2011) 375104
- [14] H.-Y. Liu, S.-H. Hong, W.-C. Sun, S.-Y. Wei, and S.-M. Yu, *IEEE Transactions on Electron Devices*, **63** (2015) 79-85
- [15] A. Bera, and D. Basak, *Applied physics letters*, **93** (2008) 053102
- [16] M. Dutta, T. Ghosh, and D. Basak, *Journal of electronic materials*, **38** (2009) 2335-2342
- [17] A. Bera, and D. Basak, *Applied Physics Letters*, **94** (2009) 163119
- [18] A. Das Mahapatra, A. Das, S. Ghosh, and D. Basak, *ACS omega*, **4** (2019) 1364-1374
- [19] C. Colbeau-Justin, M. Kunst, and D. Huguenin, *Journal of materials science*, **38** (2003) 2429-2437
- [20] L.-B. Xiong, J.-L. Li, B. Yang, and Y. Yu, *Journal of Nanomaterials*, **2012** (2012)
- [21] F. Guillemot, M. Porté, C. Labrugère, and C. Baquey, *Journal of colloid and interface Science*, **255** (2002) 75-78
- [22] H. Y. Lee, Y. H. Park, and K. H. Ko, *Langmuir*, **16** (2000) 7289-7293
- [23] E. Carter, A. F. Carley, and D. M. Murphy, *The journal of physical chemistry C*, **111** (2007) 10630-10638
- [24] C. L. Muhich, Y. Zhou, A. M. Holder, A. W. Weimer, and C. B. Musgrave, *The Journal of Physical Chemistry C*, **116** (2012) 10138-10149

- [25] A. Brajsa, K. Szaniawska, R. J. Barczyński, L. Murawski, B. Kościelska, A. Vomvas, and K. Pomoni, *Optical Materials*, **26** (2004) 151-153
- [26] D.-Y. Zhang, C.-W. Ge, J.-Z. Wang, T.-F. Zhang, Y.-C. Wu, and F.-X. Liang, *Applied Surface Science*, **387** (2016) 1162-1168
- [27] Y. Jiang, W. J. Zhang, J. S. Jie, X. M. Meng, X. Fan, and S. T. Lee, *Advanced Functional Materials*, **17** (2007) 1795-1800
- [28] L. Li, E. Auer, M. Liao, X. Fang, T. Zhai, U. K. Gautam, A. Lugstein, Y. Koide, Y. Bando, and D. Golberg, *Nanoscale*, **3** (2011) 1120-1126
- [29] S. Zhang, *Biological and Biomedical Coatings: Processing and Characterization*, Taylor & Francis, (2011)

CHAPTER-6

Ultraviolet to visible broad-band photodetection by Ag-TiO₂ plasmonic nanocomposites

Contents of this chapter has been published in *Surfaces and Interfaces* 31, 102090, (2022).

6.1 Introduction

As discussed in earlier chapters, among all the attempts taken to make visible light active TiO_2 , noble metals (Au, Ag, Pt, Pd) modified TiO_2 has earned considerable interest due to its unique optical properties and potential applications in optical devices, chemical and biological sensors, and many more [1-8]. These noble metals exhibit anomalous optical properties due to localized surface plasmon resonance (LSPR) as mentioned in previous chapters. The optical properties of these plasmonic noble metal NPs are tunable across the entire visible spectrum by varying their size and shape [5, 9-11]. Moreover, the noble metal NPs show electron storage properties which can improve the electron-hole separation in a metal-semiconductor composite system. Among all the noble metals, Ag is abundant, low expensive, and easy to process [12]. There are several works published on the visible photocatalysis regarding Ag- TiO_2 composites [6, 13-15] but the systematic study on the evolution of spectral photosensitivity of Ag NPs- TiO_2 composite films has not been reported yet which is very essential to exploit this hybrid nanocomposite for broad-band photodetector application. Here, in this chapter, Ag NPs- TiO_2 composite films have been fabricated where UV to visible broad-band photodetection properties have been measured in simple lateral photoconductive geometry.

6.2 Experimental details

TiO_2 thin films have been deposited on ultrasonically cleaned soda-lime glass substrates by sol-gel spin coating technique. The TiO_2 sol preparation and film deposition method has been mentioned in details in chapter 3. After 20th coating, TiO_2 films have been cured with UV light (365 nm, 1.2 mW) for 2 hours at RT and the sample is named as S1. For Ag NPs- TiO_2 nanocomposite film, desired thicknesses (1, 3, and 6 nm) of Ag NPs have been deposited on to TiO_2 films by evaporating metallic Ag in a vacuum coating system and the samples have been named as S2, S3, and S4.

The structural, morphological, and optical properties of the samples have been investigated using respectively XRD, XPS, FESEM, UV-VIS spectroscopy. For photoconductivity measurement, two top contacts of Al (thickness ~ 40 nm) have been thermally evaporated on the films in lateral geometry. The details of the photoconductivity set-up used in this work has been described in chapter 3.

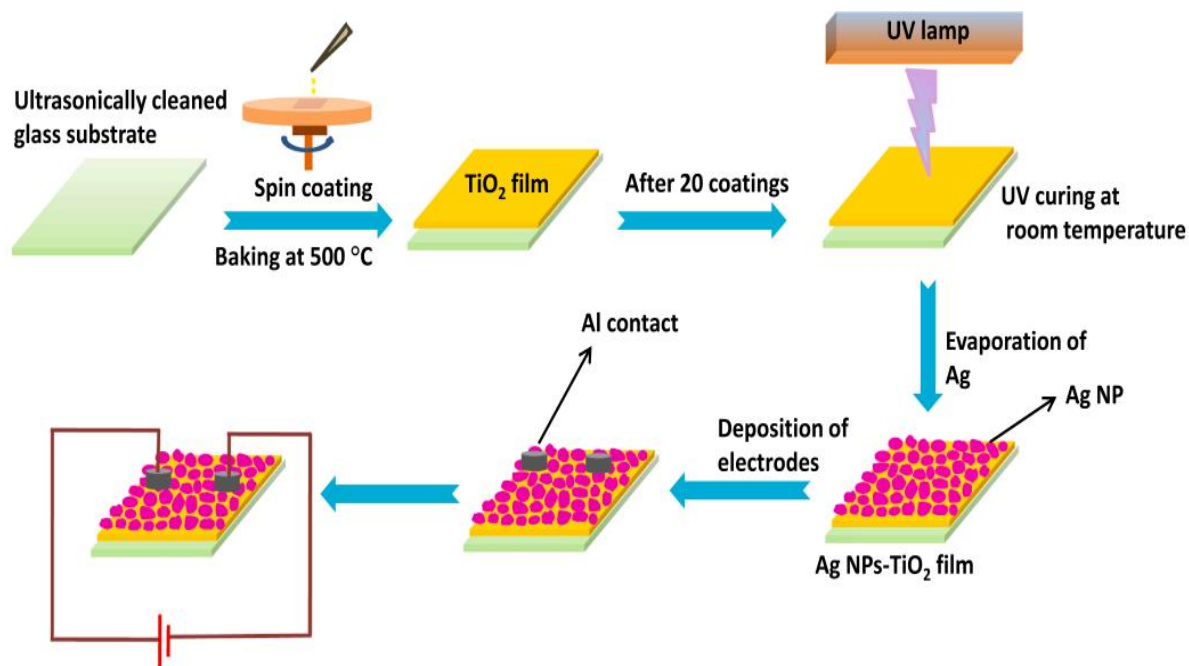


Fig. 6.1: Schematic diagram of sample preparation.

6.3 Results and discussions

XRD patterns for pristine TiO₂ and Ag NPs-TiO₂ films as presented in Fig. 6.2 show multiple peaks at $2\theta = 25.3^\circ$, 37.8° , 48.0° , and 53.9° which correspond to (101), (004), (200), and (105) planes due to for anatase phase tetragonal structure of TiO₂. A very weak peak at $2\theta = 30.9^\circ$ is observed for Ag NPs-TiO₂ films which is assigned to (121) plane of brookite phase of TiO₂. Any change in peak position or any extra peak due to Ag loading has not been found in XRD pattern. This is due to fact that Ag NPs on the top of the well crystallized TiO₂ films have not any influence on the crystallographic structure of TiO₂. The inset shows the XRD pattern of 8 nm thick Ag NPs' film deposited under same deposition conditions which indicates that the deposited Ag NPs on TiO₂ film is expected to be phase pure.

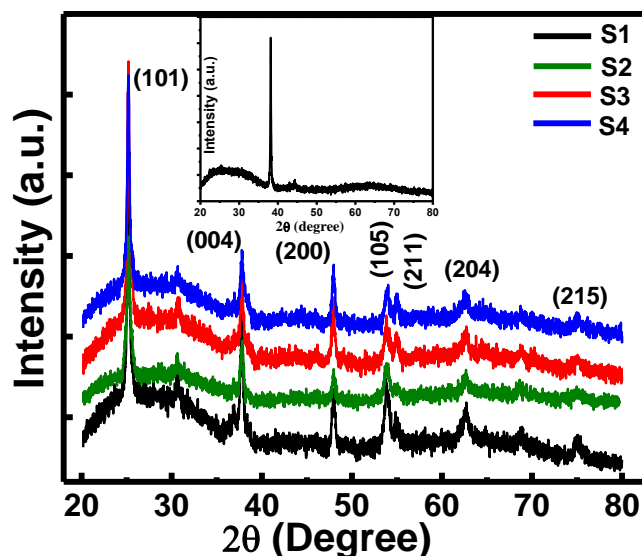


Fig. 6.2: XRD patterns of all the samples. The inset shows XRD pattern of pristine Ag NPs' film.

The FESEM images of all the samples shown in the Fig. 6.3(a), (b), (c), and (d) illustrate that the pristine sample S1 comprises of a very smooth, continuous surface of TiO_2 grains where for the nanocomposite films, Ag NPs have been deposited on the TiO_2 grains in the form of Ag islands. As the thickness of Ag increases, the sizes of the Ag islands increase with non-uniform shapes. For S2 and S3, the average sizes of the Ag NPs are 13 and 33 nm respectively but for S4 sample, the coalescence occurs between the Ag NPs giving more irregular shaped islands with larger dimensions. The elemental analyses have been performed by the EDX which confirms the presence of the peaks of Ti and O for the pristine TiO_2 and additional Ag peaks for the nanocomposite films as shown in Fig. 6.4(a), (b), (c), and (d). From the insets of the figures, it has been observed that the amount of Ag content is increased from 0.12 at. % to 0.55 at. % with the increase in the Ag thickness from 1 to 6 nm.

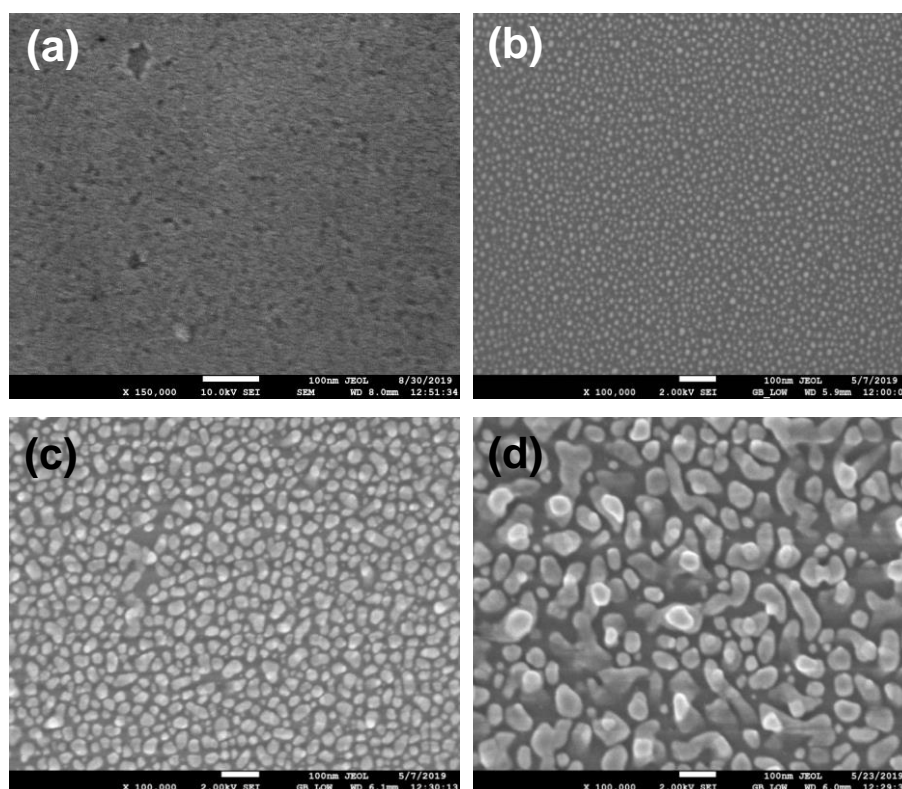


Fig. 6.3: FESEM images of the samples (a) S1, (b) S2, (c) S3, and (d) S4.

The optical transmission spectra for all the samples in Fig. 6.5(a) show that the pristine TiO_2 film is highly transparent in the 1100-500 nm region with an average transparency of $\sim 80\%$ where the transparency of the Ag NPs- TiO_2 nanocomposite films decrease in the visible region with the increase in Ag thickness. As seen from the absorbance spectra in Fig. 6.5(b), the samples exhibit a strong and sharp rise in the absorption value below 400 nm due to typical band-to-band absorption as stated in earlier chapters. The Ag NPs- TiO_2 nanocomposite films show broad and enhanced absorption in the visible wavelength region which is attributed to LSPR [16]. As observed in Fig. 6.5(b), the visible absorbance of the nanocomposite films increases with the increase in Ag thickness and the absorption hump shifts to the longer wavelength, which is similar to the results reported by Lee et al. [17] and Wang et al. [18] With the increase in Ag thickness, the particle size increases and the absorption peak undergoes a red shift since distance between the Ag NPs is decreased, resulting in collective coupled oscillation of the surface plasmons at longer wavelength. For further confirmation, the absorbance of the pristine Ag NPs films having thicknesses 1, 3, and 6 nm are deposited on glass substrates under similar evaporation condition and their absorbance spectra (Fig. 6.5(c))

have been recorded. It shows a gradual shift in absorbance maxima towards the higher wavelength region with increasing Ag thickness that clearly approves the presence of broad hump in the visible spectra in nanocomposite films is due to plasmonic Ag NPs.

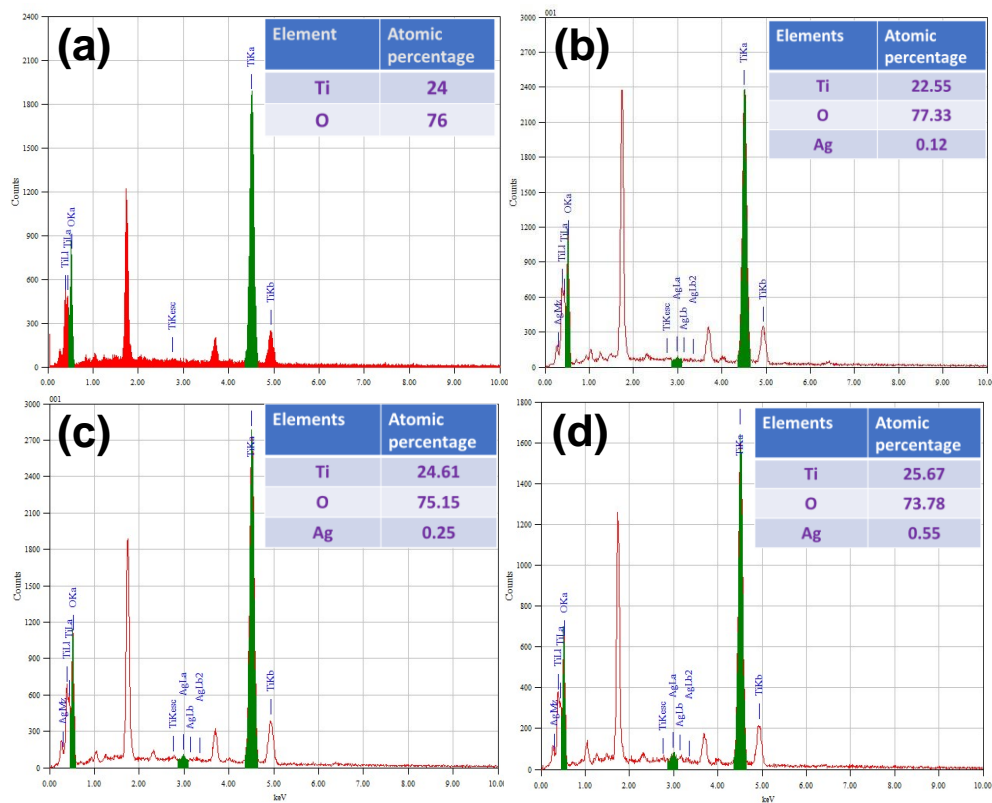


Fig. 6.4: EDX spectra of the samples (a) S1, (b) S2, (c) S3, and (d) S4. The inset shows the atomic percentage of the elemental components of the samples.

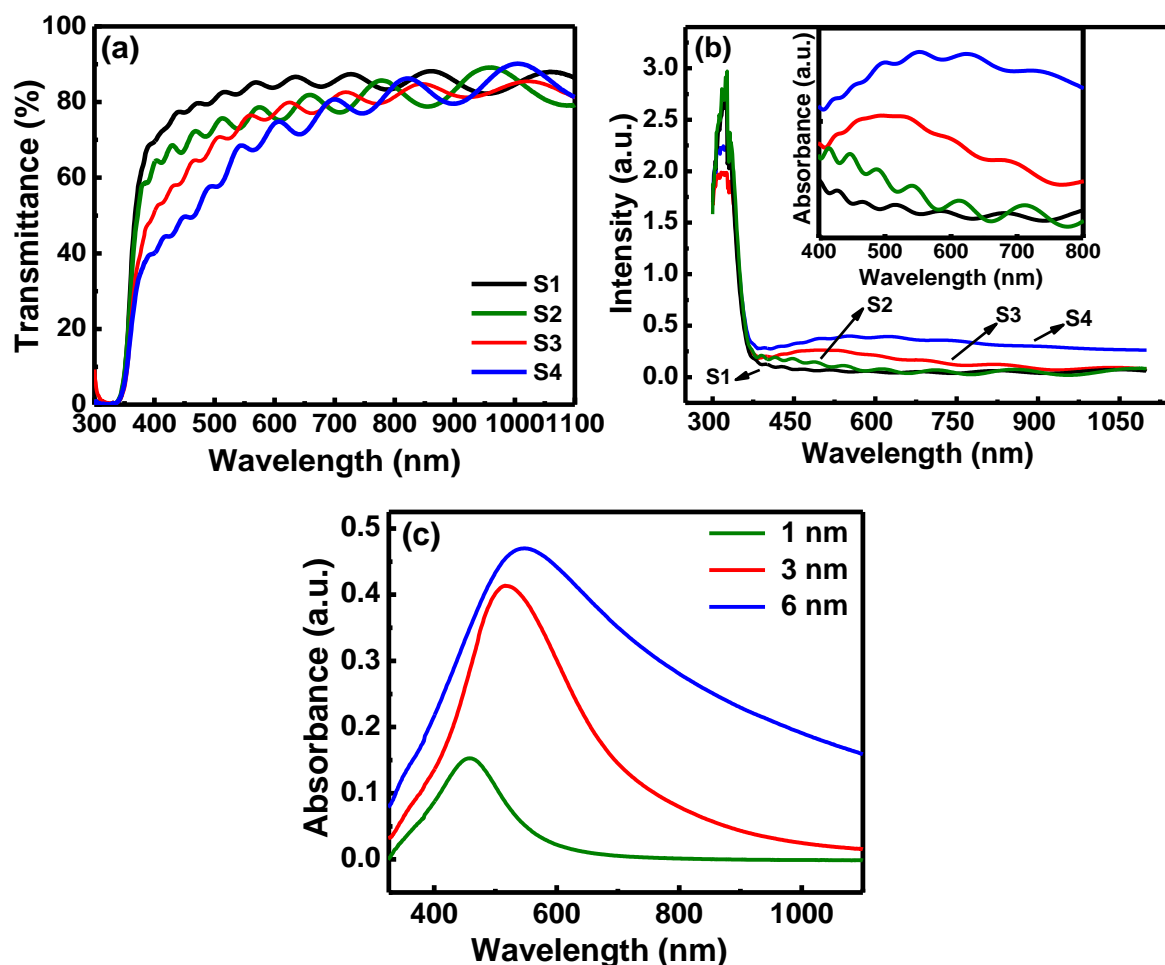


Fig. 6.5: (a) Optical transmission spectra of all the samples. (b) UV-visible absorption spectra of all the samples. Inset shows the enlarged view of spectra within the range of 400 to 800 nm. (c) Absorbance spectra of pristine Ag NPs films of different thickness on glass substrate.

For the further investigations, XPS has been carried out for a representative sample, S2. Fig. 6.6(a) shows the presence of Ti $2p_{3/2}$ peak which is deconvoluted and fitted into two peaks located at 457.5 eV and 458.2 eV. The lower binding energy peak is assigned to the existence of Ti^{3+} and the higher is for Ti^{4+} as discussed previous chapters. The presence of very low amount of Ti^{3+} in the sample indicates better stoichiometry of TiO_2 . Similarly, O 1s peak (Fig. 6.6(b)) is deconvoluted into two peaks where the peak located at a binding energy of 530.1 eV belongs to the lattice oxygen i.e., Ti-O-Ti bonds and another peak at 531.1 eV is assigned to weakly adsorbed oxygen species, subsurface low-coordinated oxygen ions, surface hydroxyl groups [19]. Fig. 6.6(c) confirms the presence of metallic Ag in the sample having binding energy peaks at 368.1 eV and 374.1 eV which correspond to the $3d_{5/2}$ and $3d_{3/2}$ peaks [20]. As

shown in this figure, there are two small humps at about 4 eV energy difference corresponding to the photoelectron peaks which is a characteristic property of plasmonic Ag metal [21, 22].

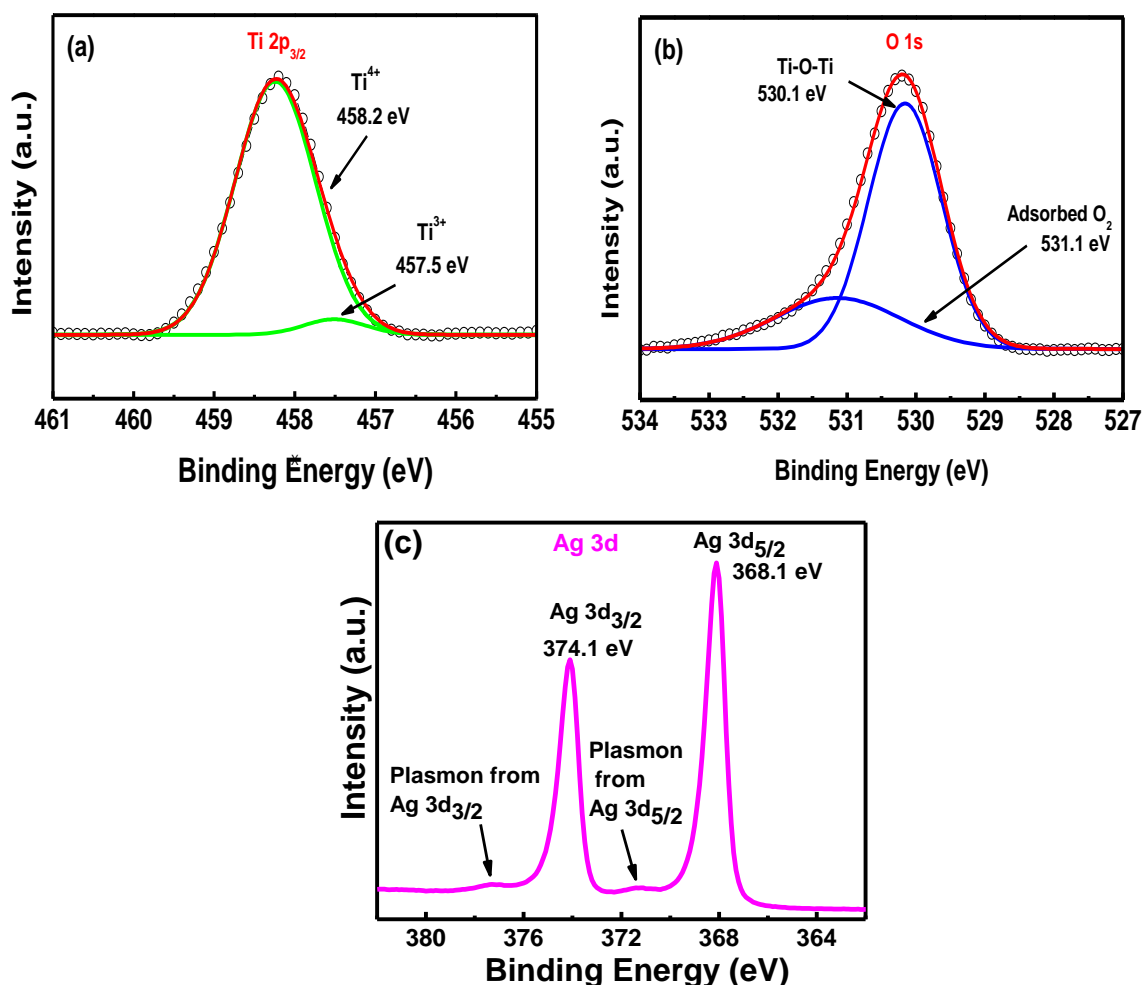


Fig. 6.6: XPS spectra of (a) Ti 2p_{3/2} (b) O 1s (c) Ag 3d peaks of S2.

The dark I - V curves of all the samples in Fig. 6.7(a) show linear behaviour which specifies Ohmic nature of the contacts. At 10 V bias, the dark current (I_d) values are 3.3×10^{-12} A, 4.7×10^{-12} A, 5.5×10^{-12} A, and 8.3×10^{-12} A for S1, S2, S3, and S4 respectively which indicates I_d values slightly increase with the increase in the Ag thickness. Formation of metal-semiconductor junctions leads to an electron transfer from TiO₂ to Ag which causes an increase in the I_d values of Ag NPs-TiO₂ nanocomposite films as compared to the pristine TiO₂ films [23]. The photocurrent spectra in the range of 300-800 nm under 10 V bias condition for S1, S2, S3, and S4 have been shown in the Fig. 6.7(b). All the samples exhibit a strong peak below 400 nm due to band-to-band photocarrier generation in TiO₂. Also, a broad hump in wavelength region of 450-750 nm has been observed though the nature of the hump is different for S1 as compared

to S2, S3, and S4. The low photoresponse of S1 in the visible wavelength region is due to de-trapping of the carriers from the sub-band-gap defects to the CB of TiO₂ [24]. As soon as Ag NPs are loaded on TiO₂ film, a significant enhancement in I_{ph} value has been observed in the visible region for S2 and then decreases for S3 and S4. Decrease in the I_{ph} in S3 and S4 can be explained by considering Ag NPs size as the size of Ag NPs play a crucial role in dominating the light extinction behaviour (e.g., the sum of light absorption and scattering). For a particle size < 30 nm, absorption is more dominant than scattering and as the particle size increases, scattering becomes more prevalent [9]. For S3 and S4, Ag particle size is greater than 30 nm, so scattering in the visible radiation instead of absorption prevails. Therefore, less surface plasmon effect has been found which leads to generation of few numbers of hot carriers [25].

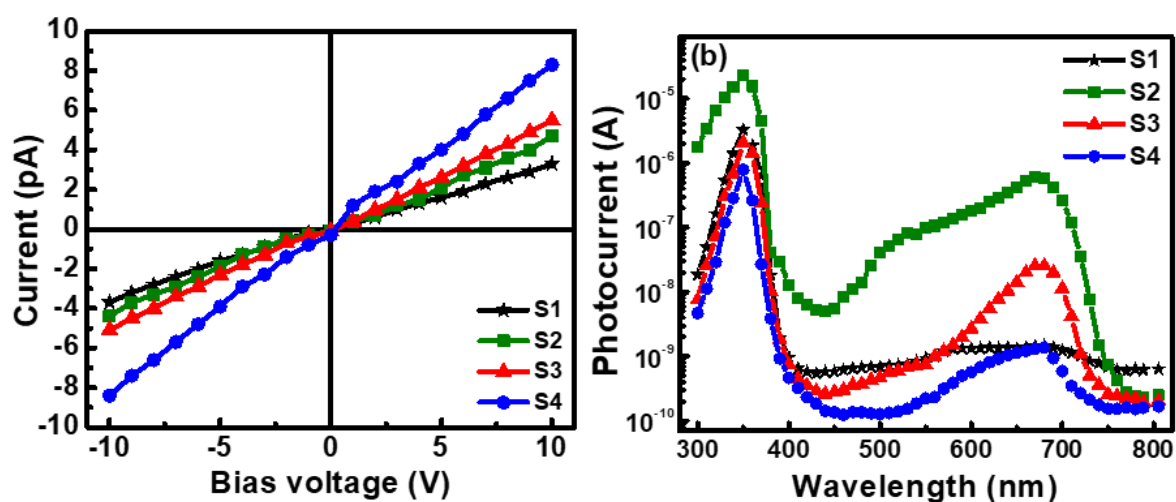


Fig. 6.7: (a) Dark I - V and (b) Photocurrent spectra at 10 V bias for all the samples.

The wavelength-dependent responsivity (R) and specific detectivity (D) have been calculated using the standard formulas as stated in chapter 2 and plotted in Fig. 6.8(a) and (b) for all samples. It has been seen that for S2 and S3, the R values in the visible region are quite higher than that of S1 and decreases for the sample S4. The maximum value of R obtained for the sample S2 is 0.1 A/W at 680 nm and 7×10^{-3} A/W at 550 nm which gives the values of D as 1.3×10^{13} Jones and 9.7×10^{11} Jones at 680 nm and 550 nm respectively which are quite high for a simple lateral geometry photoconductor.

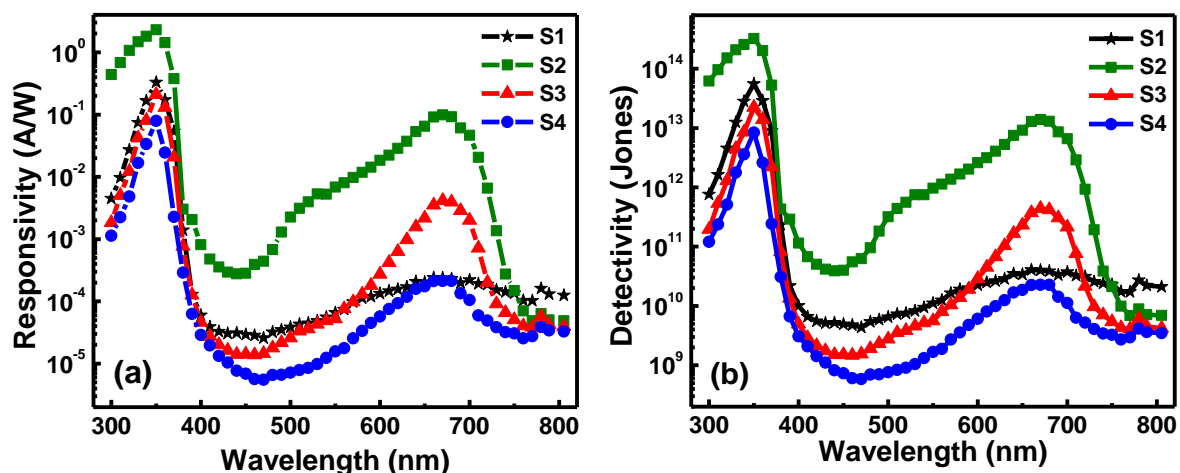


Fig. 6.8: (a) Spectral responsivity and (b) specific detectivity of all the samples.

For the detailed investigations, transient photoresponse properties of the samples under the illumination of four reference wavelengths: 350, 450, 550, and 680 nm for a duration of 12 minutes at 10 V bias have been performed and shown in Fig. 6.9(a), (b), (c), and (d) respectively. The values of I_d , I_{ph} , and I_{ph}/I_d (photosensitivity) of all the samples under all wavelengths have been extracted from the curves and noted in Table 6.1. Very high value of I_{ph} has been observed for pristine TiO_2 film which gives very high I_{ph}/I_d value of $\sim 10^7$ under UV (350 nm) illumination. This is due to generation of carriers because of band-gap absorption as stated in chapter 5. For sample S2, the I_{ph} value slightly increases but the overall I_{ph}/I_d decreases as the I_d of S2 is slightly higher as compared to the S1. For S3 and S4, the I_{ph} also decreases which leads to a lower UV photosensitivity. This may be due to some UV light shielding by the large amount of Ag NPs on the TiO_2 surface. Under 680 nm irradiation, S1 shows a photoresponse with a photosensitivity value of only $\sim 10^2$ while for S2, a very high photosensitivity value of 8.1×10^4 has been observed. However, since the I_{ph} decreases for S3 and S4, they show sensitivity values of 3.1×10^4 and 373 respectively. Under 550 nm illumination, the photosensitivity for S1 is the order of $\sim 10^2$ while for S2, the value is 9.6×10^3 . Again, the photosensitivity value decreases for S3 and S4. All the samples S1, S2, and S3 show almost similar photosensitivity ($\sim 10^2$) under 450 nm irradiation while for S4 it is 63.

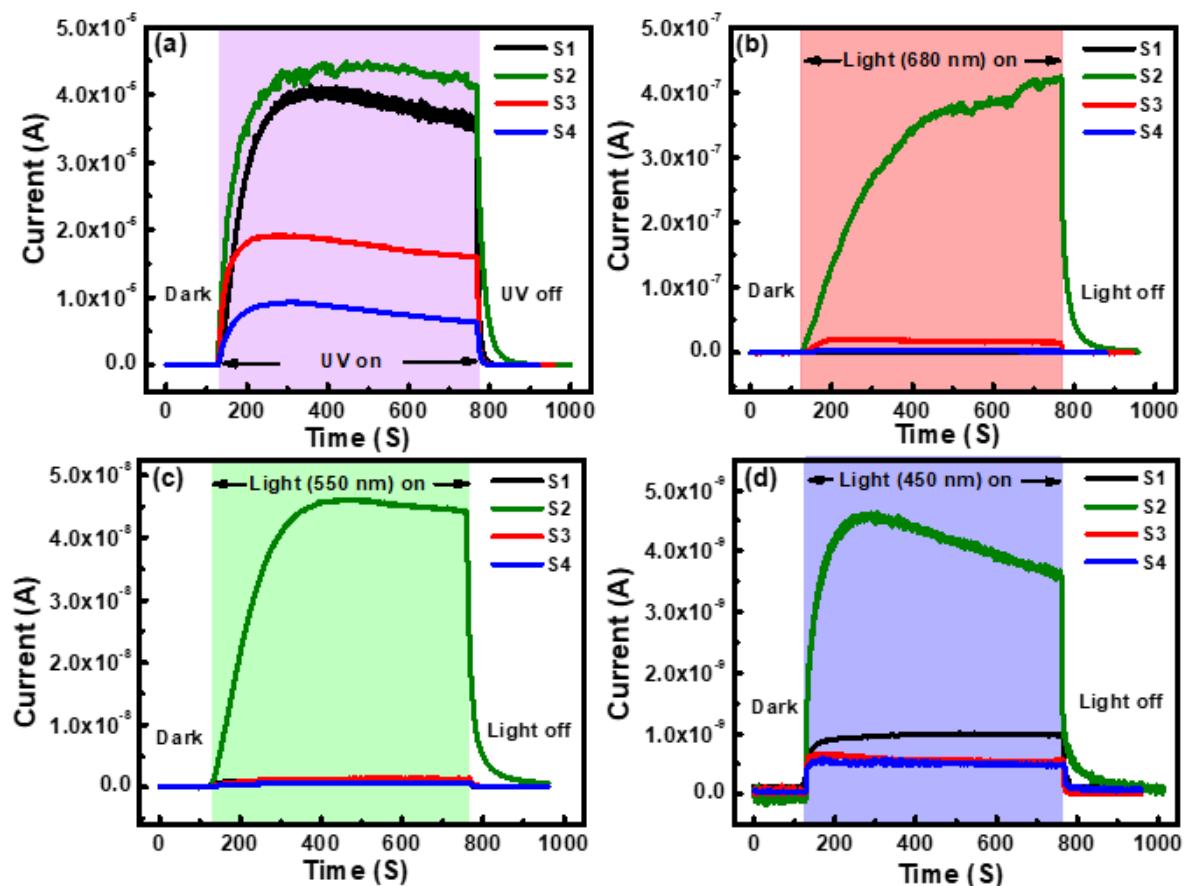


Fig. 6.9: Transient photoresponse of all the samples under (a) 350 nm, (b) 680 nm, (c) 550 nm, and (d) 450 nm light illumination at 10 V bias.

As mentioned in earlier chapter, Ti^{3+} defect states of TiO_2 have direct impact on its photoresponse property [26, 27] which is situated below the CB minima causing visible photoresponse for the pristine TiO_2 due to an efficient electron transfer through the defect sites [24]. The junction formation between Ag and TiO_2 can explain clearly the reason behind the enhanced visible photoresponse in Ag NPs- TiO_2 nanocomposite films. When Ag metal is attached with n-type TiO_2 , electrons start moving from TiO_2 to the metal as the work function of Ag (~ 6 eV) is higher than that of TiO_2 (~ 4.3 eV) which results in Schottky potential barrier (ϕ_{SB}) at metal-semiconductor junction [28]. Upon illumination of visible light on the Ag NPs- TiO_2 surface, it absorbs the visible photon which follows LSPR. The photoexcited plasmons transfer the accumulated energy to electrons in Ag which produce highly energetic hot-electrons [29-31]. These hot-electrons can easily escape from Ag surface and therefore, large number of hot-electrons are gathered in the CB of TiO_2 film from Ag NPs. These electrons can flow through the circuit under some applied bias voltage resulting an enhanced value of visible

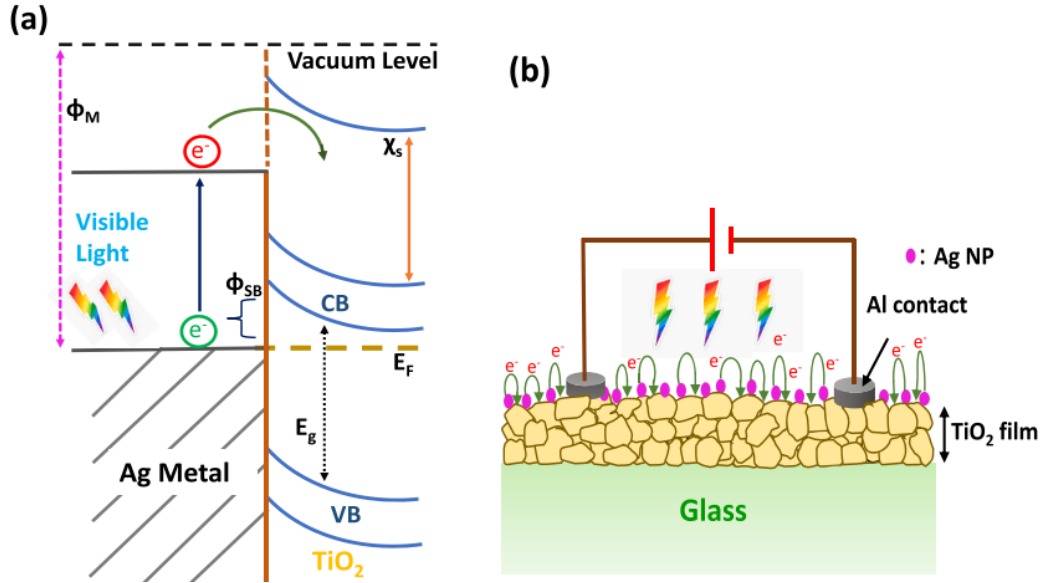


Fig. 6.10: (a) Band alignment of Ag and TiO₂ junction and (b) Schematic diagram for hot-electron transfer from Ag to TiO₂.

I_{ph} of nanocomposite films. This result is at par with the report on Ag-TiO₂ by Paul et al. [32] Fig. 6.10(a) and (b) show the schematic of band alignment between Ag and TiO₂ and the transfer of the hot-electrons from Ag to TiO₂ respectively.

Table 6.1: Dark current, photo current, and photo-to-dark current ratio under 350, 680, 550 and 450 nm illuminations for all samples.

Sample	Wavelength (nm)	I_d (A)	I_{ph} (A)	I_{ph}/I_d
S1	350	3.3×10^{-12}	5.7×10^{-5}	1.7×10^7
	680		2×10^{-9}	606
	550		1.1×10^{-9}	3.3×10^2
	450		9.8×10^{-10}	2.97×10^3
S2	350	4.7×10^{-12}	6.8×10^{-5}	1.4×10^7
	680		3.8×10^{-7}	8.1×10^4
	550		4.5×10^{-8}	9.6×10^3
	450		4.22×10^{-9}	8.98×10^2
S3	350	5.5×10^{-12}	1.8×10^{-5}	3.2×10^6
	680		1.7×10^{-8}	3.1×10^4
	550		1.4×10^{-9}	2.5×10^2
	450		5.7×10^{-10}	103.6
S4	350	8.3×10^{-12}	8.2×10^{-6}	9.8×10^5
	680		3.1×10^{-9}	373
	550		7.2×10^{-10}	8.67
	450		5.2×10^{-10}	62.6

For stability checking, the photocurrent growth and decay cycles (Fig. 6.11(a), (b), and (c)) of all the samples under periodic (2 minutes) illumination of three reference wavelengths (350, 680, and 550 nm) at a fixed bias condition have been carried out which show that the highest I_{ph} value remains almost similar with the value measured from the transient photoresponse over the cycles.

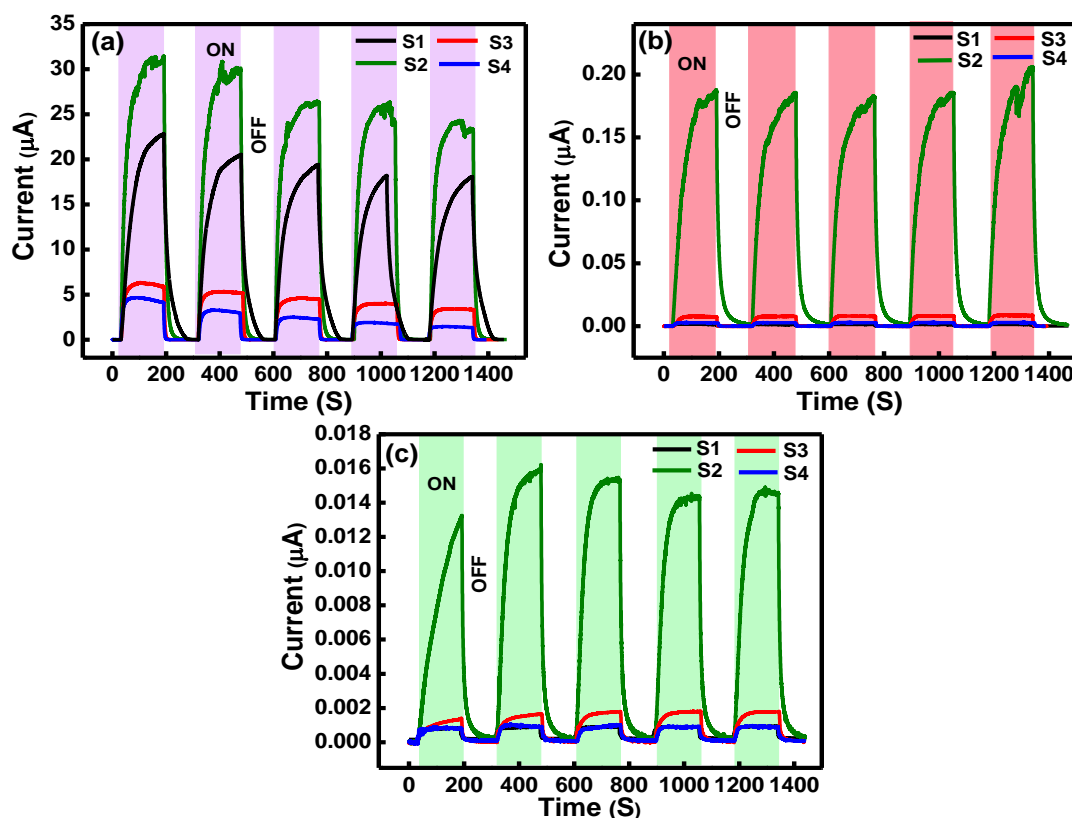


Fig. 6.11: Periodic growth-decay cycles of all the samples under (a) 350 nm, (b) 680 nm, and (c) 550 nm wavelength light irradiation.

6.4 Conclusions

In summary, UV to visible broad-band photodetection property of sol-gel grown Ag NPs-TiO₂ nanocomposite films with various thicknesses of Ag NPs have been demonstrated. Ag NPs on TiO₂ film for a layer thickness of 1 nm shows almost 7, 5, and 4 orders of photosensitivity towards 350 nm, 680 nm, and 550 nm light illuminations in a simple planar geometry which is quite interesting. The plasmonic hot-electrons contribute a vital role in the highly enhanced visible photodetection property of Ag NPs-TiO₂ nanocomposite film that greatly depends on the Ag NPs size. This study shows that Ag NPs-TiO₂ nanocomposite film in simple photconducting mode can be a promising candidate for a UV to visible broad-band photodetection.

6.5 References

- [1] J. G. Mahy, R. G. Tilkin, S. Douven, and S. D. Lambert, *Surfaces and Interfaces*, **17** (2019) 100366
- [2] X. D. Gao, G. T. Fei, S. H. Xu, B. N. Zhong, H. M. Ouyang, X. H. Li, and L. De Zhang, *Nanophotonics*, **8** (2019) 1247-1254
- [3] D. Wibowo, M. Z. Muzakkar, S. K. M. Saad, F. Mustapa, M. Maulidiyah, M. Nurdin, and A. A. Umar, *Journal of Photochemistry and Photobiology A: Chemistry*, **398** (2020) 112589
- [4] L. Yang, X. Jiang, W. Ruan, J. Yang, B. Zhao, W. Xu, and J. R. Lombardi, *The Journal of Physical Chemistry C*, **113** (2009) 16226-16231
- [5] K. Vikrant, S. Weon, K.-H. Kim, and M. Sillanpää, *Applied Materials Today*, **23** (2021) 100993
- [6] G. Wang, X. Wang, J. Liu, and X. Sun, *Chemistry—A European Journal*, **18** (2012) 5361-5366
- [7] M. K. Ntobeng, P. E. Imoisili, and T.-C. Jen, *Materials Science in Semiconductor Processing*, **123** (2021) 105569
- [8] H. Ran, J. Fan, X. Zhang, J. Mao, and G. Shao, *Applied Surface Science*, **430** (2018) 415-423
- [9] M. Rycenga, C. M. Cobley, J. Zeng, W. Li, C. H. Moran, Q. Zhang, D. Qin, and Y. Xia, *Chemical reviews*, **111** (2011) 3669-3712
- [10] S. Misra, L. Li, J. Jian, J. Huang, X. Wang, D. Zemlyanov, J.-W. Jang, F. H. Ribeiro, and H. Wang, *ACS applied materials & interfaces*, **10** (2018) 32895-32902
- [11] J. Toudert, R. Serna, and M. Jimenez de Castro, *The Journal of Physical Chemistry C*, **116** (2012) 20530-20539
- [12] N. Ghafourian, and S. Hosseini, *International Journal of Environmental Science and Technology*, **14** (2017) 2721-2732
- [13] V. K. Gupta, R. Jain, A. Mittal, T. A. Saleh, A. Nayak, S. Agarwal, and S. Sikarwar, *Materials science and engineering: C*, **32** (2012) 12-17
- [14] Y. Zeng, Y. Zhan, R. Xie, K. Hu, J. Cao, D. Lei, B. Liu, M. He, and H. Huang, *Chemosphere*, **244** (2020) 125567
- [15] M. Al-Mamun, S. Kader, M. Islam, and M. Khan, *Journal of Environmental Chemical Engineering*, **7** (2019) 103248
- [16] G. A. Alamu, O. Adedokun, I. T. Bello, and Y. K. Sanusi, *Chemical Physics Impact*, **3** (2021) 100037
- [17] K.-C. Lee, S.-J. Lin, C.-H. Lin, C.-S. Tsai, and Y.-J. Lu, *Surface and Coatings Technology*, **202** (2008) 5339-5342
- [18] W. Wang, S. Wang, J. Lv, M. Zhao, M. Zhang, G. He, C. Fang, L. Li, and Z. Sun, *Journal of the American Ceramic Society*, **101** (2018) 5469-5476
- [19] X. Wang, Y. Yao, W. Gao, and Z. Zhan, *Ceramics International*, **47** (2021) 13572-13581
- [20] M. R. Salvadori, R. A. Ando, C. A. O. Nascimento, and B. Corrêa, *Journal of Environmental Science and Health, Part A*, **52** (2017) 1112-1120
- [21] R. Pollak, L. Ley, F. McFeely, S. Kowalczyk, and D. Shirley, *Journal of Electron Spectroscopy and Related Phenomena*, **3** (1974) 381-398
- [22] Contribution of Ag surface plasmons to the optical properties of Ag/dielectric-material multilayers. *Proceedings of the Optical Interference Coatings*, (2004);
- [23] P. Joshna, A. Hazra, K. N. Chappanda, P. K. Pattnaik, and S. Kundu, *Semiconductor Science and Technology*, **35** (2019) 015001
- [24] A. Das Mahapatra, A. Das, S. Ghosh, and D. Basak, *ACS omega*, **4** (2019) 1364-1374
- [25] K. Chen, X. Feng, H. Tian, Y. Li, K. Xie, R. Hu, Y. Cai, and H. Gu, *Journal of Materials Research*, **29** (2014) 1302-1308

- [26] Y. Li, J. K. Cooper, W. Liu, C. M. Sutter-Fella, M. Amani, J. W. Beeman, A. Javey, J. W. Ager, Y. Liu, and F. M. Toma, *Nature communications*, **7** (2016) 1-7
- [27] Y. Liu, Q. Zhu, X. Li, G. Zhang, Y. Liu, S. Tang, E. Sharman, J. Jiang, and Y. Luo, *The Journal of Physical Chemistry C*, **122** (2018) 17221-17227
- [28] F. Hossein-Babaei, M. M. Lajvardi, and N. Alaei-Sheini, *Applied Physics Letters*, **106** (2015) 083503
- [29] J. Song, J. Long, Y. Liu, Z. Xu, A. Ge, B. D. Piercy, D. A. Cullen, I. N. Ivanov, J. R. McBride, and M. D. Losego, *ACS Photonics*, **8** (2021) 1497-1504
- [30] S. V. Singh, M. P. Kumar, S. Anantharaj, B. Mukherjee, S. Kundu, and B. N. Pal, *ACS Applied Energy Materials*, **3** (2020) 1821-1830
- [31] H. Lee, Y. K. Lee, E. Hwang, and J. Y. Park, *The Journal of Physical Chemistry C*, **118** (2014) 5650-5656
- [32] K. K. Paul, and P. Giri, *The Journal of Physical Chemistry C*, **121** (2017) 20016-20030

CHAPTER-7

**Investigation on photoluminescence and
photodetection properties of Li doped TiO₂ films**

7.1 Introduction

Among the various strategies adopted to tune the defects in TiO₂, doping in TiO₂ is very useful [1,2]. Both metals (Cu, Co, Ni, V, Fe, Ru, Li, Ag) and non-metals (N, S, C, B, P, I, F) can be introduced as dopant in TiO₂ to study the defects which play an important role on tailoring the photophysical properties as stated in earlier chapters [1-4]. Li is one of the most promising dopants which can improve the optical and electrical properties when introduced in TiO₂ [5-7]. Being a group-I element, the Li ion (Li⁺) has the smallest ionic radius (0.60 Å), which is very near to that of the Ti ion (0.68 Å) [8] and therefore, Li can easily occupy the Ti⁴⁺ site or interstitial position in TiO₂ matrix [9].

In conventional synthesis techniques such as hydrothermal, aqueous chemical growth, sol-gel, it has been observed that the doping impurities tend to accumulate on the surface of the TiO₂ due to excess surface energy [10]. This leads to decrease in the crystallinity of the doped TiO₂ in some cases [11, 12]. In this situation, post-growth doping via ion implantation method can be a very fruitful solution for successful doping in TiO₂ [13-15]. In the process of ion implantation, the collisions between the energetic dopant ion beam and the host lattice produce several point defects inside the host or target material which may strongly influence its structural and optoelectronic properties. Therefore, keeping these issues in mind, Li ion has been implanted in sol-gel TiO₂ film and evolution of various defects due to ion implantation and their correlation with the photophysical properties of TiO₂ film has been presented in this chapter.

7.2 Experimental details

TiO₂ films have been deposited on properly cleaned glass substrates by sol-gel spin coating technique. The details of sol preparation and film coating process have already been described in chapter 3. After each coating of TiO₂ sol on glass substrates was dried at 120 °C for 10 minutes and then heated at 350 °C for 20 minutes to obtain crystalline films. After 20th coating, the films were finally annealed at 500 °C for 1 hour. The ion implantation experiment was then performed on the samples with 100 keV Li ions having three doses ranging from 1×10¹⁴ to 1×10¹⁵ ions/cm² in a radiation chamber. The implantation process was executed in vacuum at pressure of ~ 5×10⁻⁷ Torr at RT. During implantation, the ion beam was scanned over 1 cm² area on the sample and the beam current was fixed at 80 nA. After Li implantation, the implanted TiO₂ films were annealed in Argon ambient at 450 °C for 1 hour. The

unimplanted TiO₂ was also annealed in same condition and have been considered as the pristine sample in this work. The nomenclature of all the samples is given in Table 7.1.

Table 7.1. Nomenclature of the samples.

Fluence (ions/cm ²)	Sample Name
0	Pristine
1×10^{14}	TLi114
5×10^{14}	TLi514
1×10^{15}	TLi115

7.3 Results and discussions

Fig. 7.1 depicts the XRD patterns of all the samples which correspond to the diffractions from the (101), (004), (200), and (105) planes of tetragonal anatase TiO₂ (JCPDS file: PDF#211272). Any extra diffraction peak due to Li-related impurities or any secondary phase is not observed in the XRD patterns of the implanted samples which indicates that the anatase structure is stable after Li doping. An enlarged view of the peak (101) of all the samples in Fig. 7.1(b) shows that peak shifts towards higher 2θ value under Li doping which is also reported

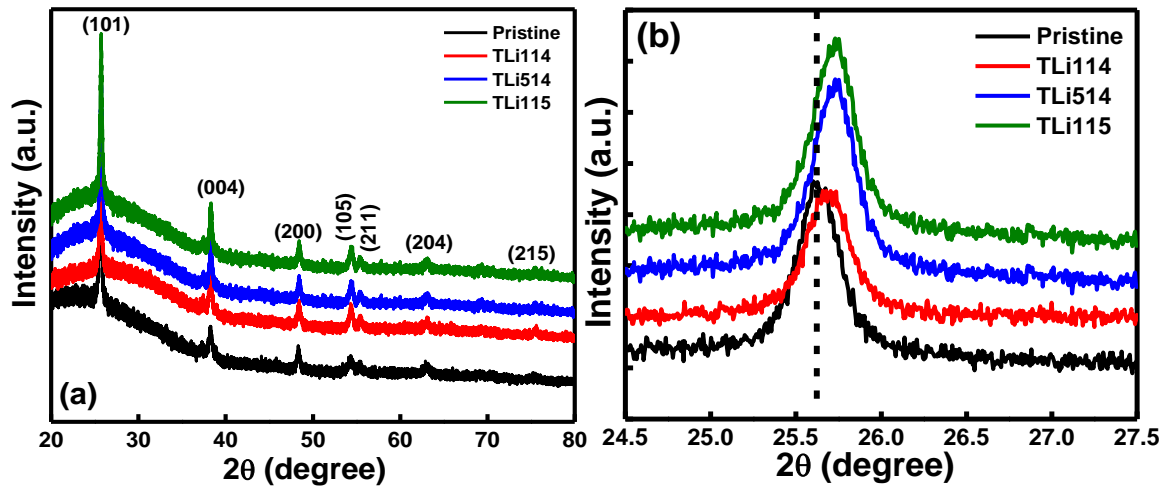


Fig. 7.1: (a) XRD patterns of all the samples and (b) Enlarged view of (101) peak of all the samples.

by Ghicov et al. [15]. The crystallite size (D) of all samples has been calculated for the most intense peak ($2\theta \sim 25.6$) using the Debye-Scherrer's formula which is already stated in chapter 3. The estimated values of D are 27.91, 25.88, 26.04, and 26.77 nm for Pristine, TLi114, TLi514, and TLi115 respectively which shows no significant change in crystallite size.

The XPS scans have been carried out after sputtering the samples for ~ 100 s to remove the undesired particles from the sample's surface. Fig. 7.2(a) shows the XPS full scans of pristine and a representative implanted sample TLi115. A broad peak in the region 50-63 eV centered at ~ 56 eV confirms the presence Li 1s [16] as seen from Fig. 7.2(b). Fig. 7.2(c) and (d) correspond to broad Ti 2p peak for pristine and TLi115 respectively. Ti 2p is doublet with the lower energy peak (~ 455 -460 eV) which is assigned to Ti $2p_{3/2}$ and the higher energy peak (~ 460 -472 eV) is for Ti $2p_{1/2}$. Using Gaussian multi-peak fitting, both the energy regions are fitted to suitable number of peaks. Both for pristine and TLi115 sample, Ti $2p_{3/2}$ peak is deconvoluted into three peaks centered at ~ 454 eV, 456 eV, and 458 eV which are associated to Ti^{2+} , Ti^{3+} , and Ti^{4+} respectively [17]. Similarly, Ti $2p_{1/2}$ peak is also fitted into three peaks showing Ti^{2+} , Ti^{3+} , and Ti^{4+} at ~ 460 , 461, and 463 eV for pristine sample and for TLi115, this peak is fitted into two peaks showing contribution of Ti^{3+} and Ti^{4+} . From the area under fitted curve, it has been calculated that the presence of Ti^{3+} is slightly higher in TLi115 than pristine which may be due to incorporation of Li in TiO_2 lattice [18]. It has observed from the Fig. 7.2(e)-(f) that O 1s peak for both the pristine and TLi115 are asymmetric in nature and can be deconvoluted into three Gaussian peaks centered at ~ 530 eV (O_a), ~ 531 eV (O_b) and ~ 532 eV (O_c). As said earlier, the lower energy peak is related to O^{2-} ions of TiO_2 lattice and surface adsorbed hydroxyl groups and oxygen molecules generally correspond to the higher energy peak. The middle one is generally assigned to V_O related defects present in the sample. From the peak area calculations, the contribution of V_O related states in TLi115 (17%) is more than that of the pristine (12%), suggesting an increase in the formation of V_O defects due to Li ion implantation [19].

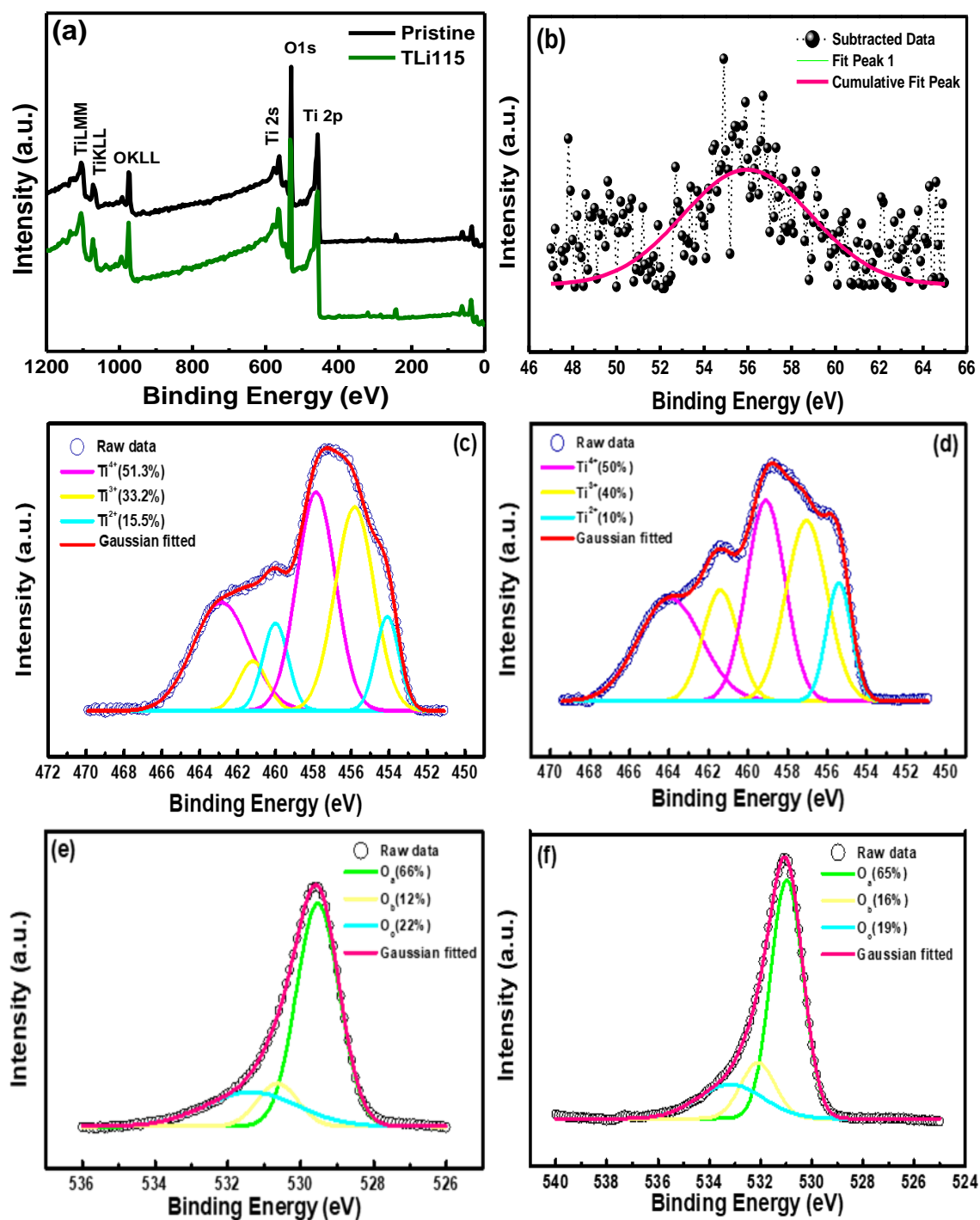


Fig. 7.2: (a) XPS full scan of pristine and TLi115, (b) Li 1s peak of TLi115, (c), (d) Ti 2p, and (e), (f) O 1s peak fitting of pristine and TLi115 respectively.

UV-VIS absorption spectra in Fig. 7.3 shows that all the samples exhibit maximum absorbance below 350 nm due to band edge absorption of TiO_2 and no significant change has been observed for Li implanted samples. From the Tauc plot, it has been estimated that pristine and implanted samples exhibit almost similar band gap values in the range of ~ 3.4 - 3.45 eV.

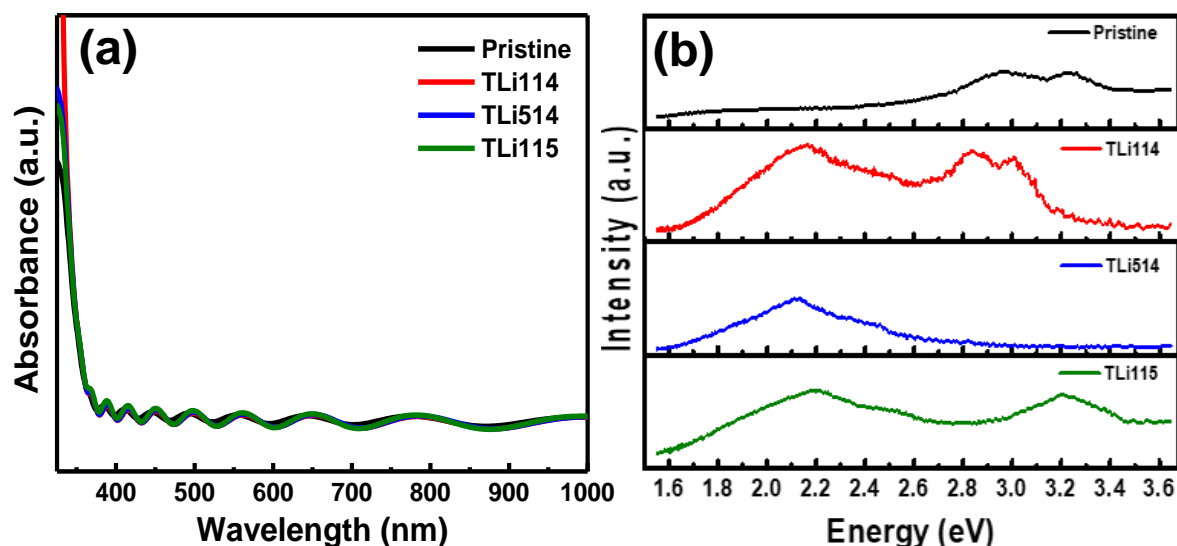


Fig. 7.3: (a) Optical absorbance spectra and (b) PL spectra of the samples.

In order to further investigate the effect of Li doping on the creation of defects, the RT PL spectra has been taken and presented in Fig. 7.3(b). In the pristine TiO_2 , the two emission bands centred at ~ 3.24 eV and ~ 2.97 eV are distinctively observed. The first one is assigned for band edge emission which falls in the UV region commonly observed in TiO_2 [20]. Similar band-to-band emission is also reported by Choudhury et al. [21] for undoped TiO_2 . Tripathi et al. have observed a peak around 402 nm (~ 3.1 eV) in anatase TiO_2 phase and they have assigned this peak due to emission from shallow trap near band edge [22]. PL peak at 3.2 eV due to band-gap absorption in TiO_2 is also reported by Chen et al. [23] The peak at 2.97 eV (violet emission) is due to recombination of carriers in the shallow acceptor levels near VB of TiO_2 . Pallotti et al. [24] have also found near band edge emission centered at ~ 2.9 – 3.0 eV in as-grown TiO_2 . A detailed analysis of emission property of anatase TiO_2 has been carried out by Abazovic et al. [25] A broad band PL with the direct band edge transitions along with several indirect transitions at 3.19, 3.05, and 2.91 eV have been reported. A new peak has been appeared for the initial fluence Li implanted TiO_2 (TLi114) at 2.82 eV in addition to the peak

at ~3 eV. This indicates implantation causes more and more acceptor levels. Additionally, a broad defect emission in the visible region centered at ~2.15 eV (yellow-green emission) is also observed for this sample. Lopez et al. [26] have illustrated that the green PL band mainly originates from the recombination of electrons in the CB or shallow traps with holes trapped in deep defect states like V_O and this defect increases with the Li incorporation into TiO_2 which results more intense green emission in Li doped TiO_2 sample. As soon as the sample is implanted with the Li fluence of 5×10^{14} ions/cm², the UV and the violet emissions disappear probably due to creation of nonradiative recombination pathways. As the Li implantation fluence increases, the density of the point defects increases, which are not completely restored upon annealing at higher fluences. The large concentration of the point defects acts as nonradiative recombination centres reducing the intensity of the UV and violet emissions. For TLi514, the visible yellow-green band has also been observed but this band shifts to ~2.2 eV as the implantation fluence increases to 1×10^{15} ions/cm². Green PL has a direct correlation with V_O and/or Ti^{3+} type of states on (101) oriented anatase crystal surface as discussed in chapter 4. Here, the results indicate more formation of V_O and/or Ti^{3+} states due to Li implantation. As calculated by Valentien et al. [27], these V_O - Ti^{3+} states locate at 0.7 eV below the CB minima. In addition to various visible bands, the as-grown TiO_2 may exhibit green band in its PL spectra as reported in the previous studies. But in our case, the pristine TiO_2 film does not show green PL. This may be due to final annealing of the pristine sample in Argon environment.

(a)

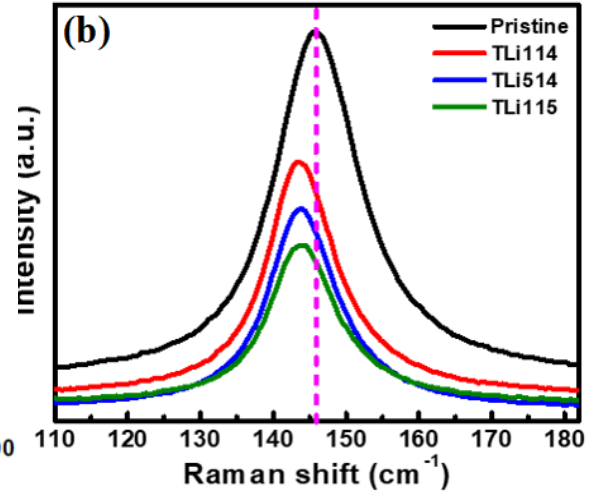
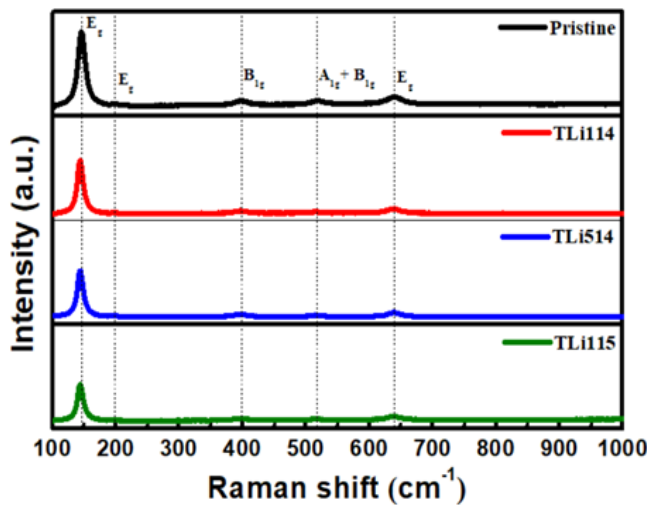


Fig. 7.4: (a) Raman spectra and (b) Enlarged view of $1E_g$ mode of all the samples.

The appearance of the visible emission at higher fluences indicates the formation of more $\text{Ti}^{3+}/\text{V}_\text{O}$ type defects, which is at par with the XPS results.

The anatase phase of TiO_2 shows overall six characteristics active Raman modes, which are represented as 1A_{1g} , 2B_{1g} , and 3E_g symmetries. The RT Raman scattering spectra ($100\text{--}1000\text{ cm}^{-1}$) of the pristine and implanted samples are presented in Fig. 7.4(a), where the Raman vibrational modes have been appeared at ~ 145 , 199 , 399 , 516 , and 640 cm^{-1} . The modes are very distinctive and can be assigned to the anatase phase of TiO_2 [28], which support the XRD results. The peaks at 145 cm^{-1} , 199 cm^{-1} , and 640 cm^{-1} correspond to the E_g - symmetric stretching vibration of O-Ti-O in anatase TiO_2 . The other peaks at 399 cm^{-1} is associated with the B_{1g} - symmetric bending vibration of O-Ti-O where the peak at 516 cm^{-1} to the A_{1g} - antisymmetric bending vibration of O-Ti-O. The most dominant mode at 145 cm^{-1} has been seen (Fig. 7.4(b)) to be shifted towards lower wavenumber with Li doping, which may be due to the inclusion of Li into Ti sublattice [29, 30]. This shift is also observed by Lopez et al. [26] for Li doped TiO_2 nanoparticles. The intensity of the same mode has also been decreased as the fluence increases. This indicates an increase in the defects in the samples due to Li implantation. This study agrees with the PL results. However, the intensity and the peak position of the other modes has been remained unaltered even after implantation.

To investigate the effect of Li incorporation on the conductivity of TiO_2 film, dark current (I_d) has been measured applying a fixed bias of 10 V of all the samples and noted in Table 7.2. The pristine sample exhibits highest I_d and the values decrease with the increase of Li ion fluence indicating an increase in the resistivity due to Li ion implantation. Formation of various implantation-induced defects in the Li implanted films may be the probable cause. Fig. 7.5(a) shows the spectral photocurrent response in the region of $300 - 800\text{ nm}$ for all films measured at 10 V bias which depicts a sharp increase in photocurrent value at $\sim 340\text{ nm}$ for both pristine and implanted samples which is due to band-to-band absorption and photocarrier generation by TiO_2 . A hump in the visible region of the photocurrent spectra has been observed due to the presence of in-gap defect states where the nature of the hump is different from implanted samples to pristine as seen from the inset of Fig. 7.5(a).

The photocurrent transient curves under UV (340 nm) and visible (500 nm) irradiation for all the samples for a duration of 10 minutes at 10 V bias condition have been shown in Fig. 7.5(b, c). It has been observed that all the samples are highly responsive to UV radiation. As soon as UV light shine on the samples, photocurrent values increase sharply and then photocurrent

relaxation process occurs as stated in chapter 5 previously. Photo-to-dark current ratio (photosensitivity) has been calculated for all the samples and shown in Table 7.2. The pristine sample exhibits highest photosensitivity value of 5×10^3 and with an increasing Li ion fluence, this value decreases. The 80% photocurrent growth time and decay time for UV transient cycle have been calculated for all samples and summarized in Table 7.2. The values are comparable showing no notable change. When the samples are irradiated with visible light (500 nm) photocurrent increases slightly showing photosensitivity of 1 order as shown in Fig. 7.5(c). This value remains almost same for both pristine and implanted samples.

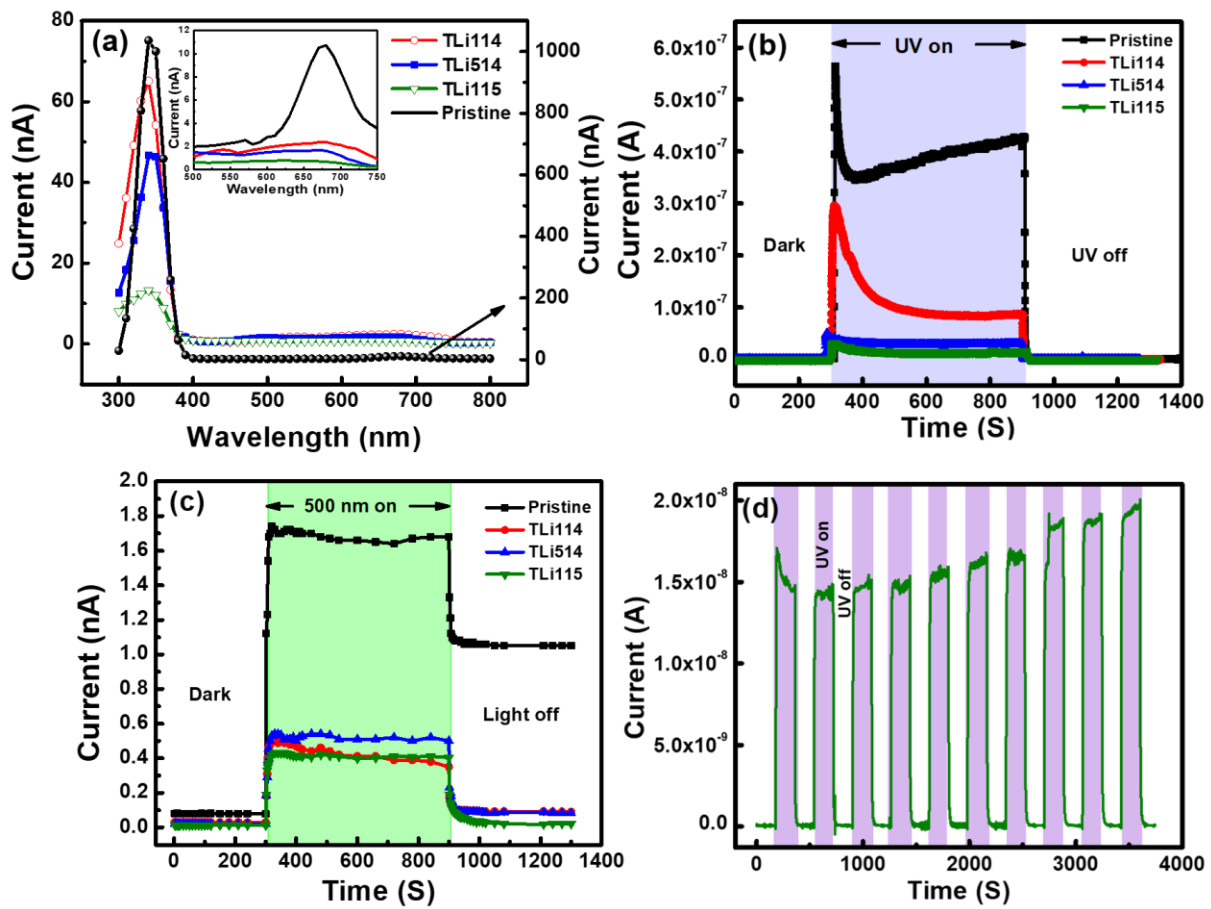


Fig. 7.5: (a) Photocurrent spectra of all samples. Transient photoresponse of all samples under (b) UV (340 nm) and (c) visible (500 nm) illumination. (d) Periodic growth-decay cycles of sample TLI115.

The photocurrent periodic growth and decay cycles for highest dose sample, TLI115 under periodic (2 minutes) UV illumination at 10 V bias condition has been measured and presented

in Fig. 7.5(d). The highest photocurrent value remains almost similar with the value of the transient cycle indicating stable photosensitivity of the samples.

Table 7.2: The values dark current (I_d), photocurrent (I_{ph}), I_{ph}/I_d (for UV and visible (500 nm) illuminations), rise time, and decay time for UV illumination for all samples.

Sample	I_d (A)	I_{UV} (A)	I_{500} (A)	I_{UV}/I_d	I_{500}/I_d	Rise time (S)	Decay time (S)
Pristine	8×10^{-11}	4×10^{-7}	1.66×10^{-9}	5×10^3	20	0.57	1.2
TLi114	3×10^{-11}	8.7×10^{-8}	4.5×10^{-10}	2.9×10^3	15	0.75	3.2
TLi514	2.1×10^{-11}	2.9×10^{-8}	5.1×10^{-10}	1.4×10^3	24	0.37	1.8
TLi115	1.2×10^{-11}	1.4×10^{-8}	4.1×10^{-10}	1.2×10^3	19.5	0.6	3

7.4 Conclusions

In summary, photodetection and PL property of Li doped sol-gel grown TiO_2 via ion implantation method has been illustrated in this chapter. It has been observed that PL property of Li doped TiO_2 films significantly changes with the Li ion fluence due to evolution of various types defects due to doping where photodetection property does not vary so much. Li ion doping in TiO_2 causes the $\text{Ti}^{3+}/\text{V}_\text{O}$ type defects increases which is also supported by XPS and Raman spectroscopy studies along with PL analyses.

7.5 References

- [1] M. Khairy, and W. Zakaria, Egyptian Journal of Petroleum, **23** (2014) 419-426
- [2] A. Zaleska, Recent patents on engineering, **2** (2008) 157-164
- [3] D. Zhang, J. Chen, Q. Xiang, Y. Li, M. Liu, and Y. Liao, Inorganic chemistry, **58** (2019) 12511-12515
- [4] P.-P. Filippatos, N. Kelaidis, M. Vasilopoulou, D. Davazoglou, N. N. Lathiotakis, and A. Chronos, Scientific Reports, **9** (2019) 1-10
- [5] A. Belous, O. Gavrilenko, E. Pashkova, and V. Mirnyi, Russian journal of electrochemistry, **38** (2002) 425-430
- [6] M. Tardío, R. Ramírez, R. González, and Y. Chen, Physical Review B, **66** (2002) 134202
- [7] K. C. Chiu, and J. H. Jean, Journal of the American Ceramic Society, **94** (2011) 3711-3715

- [8] J. Mahler, and I. Persson, *Inorganic chemistry*, **51** (2012) 425-438
- [9] R. A. Roca, F. Guerrero, J. A. Eiras, and J. Guerra, *Ceramics International*, **41** (2015) 6281-6285
- [10] S. Sarkar, and D. Basak, *Applied Physics Letters*, **103** (2013) 041112
- [11] H. Beitollahi, S. Tajik, F. G. Nejad, and M. Safaei, *Journal of Materials Chemistry B*, **8** (2020) 5826-5844
- [12] O. Lupan, L. Chow, L. K. Ono, B. R. Cuenya, G. Chai, H. Khallaf, S. Park, and A. Schulte, *The Journal of Physical Chemistry C*, **114** (2010) 12401-12408
- [13] A. Das, and D. Basak, *ACS Applied Electronic Materials*, **3** (2021) 3693-3714
- [14] L. Large, and R. Bicknell, *Journal of Materials Science*, **2** (1967) 589-609
- [15] A. Ghicov, J. M. Macak, H. Tsuchiya, J. Kunze, V. Haeublein, L. Frey, and P. Schmuki, *Nano Letters*, **6** (2006) 1080-1082
- [16] A. Andersson, D. Abraham, R. Haasch, S. MacLaren, J. Liu, and K. Amine, *Journal of The Electrochemical Society*, **149** (2002) A1358
- [17] S. Hashimoto, and A. Tanaka, *Surface and Interface Analysis: An International Journal devoted to the development and application of techniques for the analysis of surfaces, interfaces and thin films*, **34** (2002) 262-265
- [18] P. Singh, (2011)
- [19] R. Zhao, G. Wang, Y. Mao, X. Bao, Z. Wang, P. Wang, Y. Liu, Z. Zheng, Y. Dai, and H. Cheng, *Chemical Engineering Journal*, **430** (2022) 133085
- [20] H. Abdullah, D.-H. Kuo, and Y.-H. Chen, *Journal of materials science*, **51** (2016) 8209-8223
- [21] B. Choudhury, M. Dey, and A. Choudhury, *Applied Nanoscience*, **4** (2014) 499-506
- [22] A. K. Tripathi, M. K. Singh, M. C. Mathpal, S. K. Mishra, and A. Agarwal, *Journal of Alloys and Compounds*, **549** (2013) 114-120
- [23] X. Chen, and C. Burda, *Journal of the American Chemical Society*, **130** (2008) 5018-5019
- [24] D. Pallotti, E. Orabona, S. Amoruso, C. Aruta, R. Bruzzese, F. Chiarella, S. Tuzi, P. Maddalena, and S. Lettieri, *Journal of Applied Physics*, **114** (2013) 043503
- [25] N. D. Abazović, M. I. Čomor, M. D. Dramićanin, D. J. Jovanović, S. P. Ahrenkiel, and J. M. Nedeljković, *The Journal of Physical Chemistry B*, **110** (2006) 25366-25370
- [26] A. Vázquez-López, A. Cremades, and D. Maestre, *Optical Materials Express*, **12** (2022) 3090-3100
- [27] C. Di Valentin, G. Pacchioni, and A. Selloni, *The Journal of Physical Chemistry C*, **113** (2009) 20543-20552
- [28] T. Ohsaka, F. Izumi, and Y. Fujiki, *Journal of Raman spectroscopy*, **7** (1978) 321-324
- [29] T. Ravishankar, G. Nagaraju, and J. Dupont, *Materials Research Bulletin*, **78** (2016) 103-111
- [30] T. K. Ghorai, *Open Journal of Physical Chemistry*, **1** (2011) 28

CHAPTER-8

Summary and future scope

❖ Summary

A comprehensive study on sol-gel TiO₂-based thin films modified via various post-growth treatments, anchoring with metal nanoparticles and doping have been illustrated in this thesis with the aim to study its photophysical properties namely PL and photodetection through monitoring the defects. The noteworthy outcomes of the studies are summarized below:

various post-growth treatments such as thermal annealing in air and vacuum, UV curing at room temperature have been found to control the defects in pristine TiO₂ thin films. Besides a sharp UV band edge emission, the existence of adsorbed O₂ molecules, OH species, and Ti³⁺ related defect states on the surface result in an enhanced visible emission in all the post-growth treated TiO₂ films. The air annealed sample followed by rapid cooling offers a stronger UV emission and reduced visible emissions due to reduction in the number of surface traps. Therefore, sol-gel TiO₂, if subjected to air annealing at 500 °C and cooled rapidly is quite promising as highly luminescent oxide material.

UV cured TiO₂ film shows high UV-to-visible rejection ratio of 1.7×10^3 under 10 μW incident light at 10 V bias. Very high photo-to-dark current ratio ($\sim 10^4$) of the film under as low as 1 V bias and only 10 μW incident UV light has been found without typical device fabrication. UV curing makes TiO₂ surface hydrophilic resulting higher adsorbed OH related trap states responsible for enhanced UV photosensitivity.

To extend the photoactivity of TiO₂ in the visible region, TiO₂ film has been modified with plasmonic Ag nanoparticles wherein Ag-TiO₂ nanocomposite film with 1 nm Ag layer thickness exhibits the highest photo-to-dark current ratio of 10^7 , 10^5 , and 10^4 under 350 nm, 680 nm, and 550 nm incident lights respectively in a simple planar MSM photoconducting geometry implying high efficiency for designing broad-band photodetector.

Li doped TiO₂ films synthesized via post-growth ion implantation shows significant changes in the PL emission property with the Li ion fluence where the UV photosensitivity deteriorate while Li doping. For lower Li ion fluence, formation of more numbers of acceptor levels and for higher fluence, enhanced visible emission indicate creation of more defects like V_O and Ti³⁺ related states. UV This study gives an idea that PL properties of TiO₂ may be tuned efficiently by Li doping.

❖ **Future Scope**

From the summary of this thesis work, few scopes are outlined as follows:

- Modifying the functional properties via controlling the defects of other oxide thin films by various post-growth treatments
- Developing UV to visible broad-band photodetector of various TiO₂-based nanocomposites /heterostructures
- Doping with other dopants in TiO₂ to investigate the above said photophysical properties